THE SELF-STANDING, MALLEABLE DOUGHS OF ADVANCED CERAMICS FACILITATE LOW-NUMBER PRODUCTION AND PROTOTYPING ON A BENCHTOP

by
AYŞE AY

Submitted to the Graduate School of Natural Sciences and Engineering
in partial fulfillment of the requirements for the degree of Doctor of Philosophy

Sabancı University
June 2024

THE SELF-STANDING, MALLEABLE DOUGHS OF ADVANCED CERAMICS FACILITATE LOW-NUMBER PRODUCTION AND PROTOTYPING ON A BENCHTOP

Approved by:

Assoc. Prof. Özge AKBULUT
(Thesis Supervisor)
Prof. Alpagut KARA

Assoc. Prof. Damla EROĞLU PALA

Prof. Fevzi Çakmak CEBECİ

Prof. Yusuf Ziya MENCELOĞLU

Approval Date:

ABSTRACT

THE SELF-STANDING, MALLEABLE DOUGHS OF ADVANCED CERAMICS FACILITATE LOW-NUMBER PRODUCTION AND PROTOTYPING ON A BENCHTOP

AYŞE AY

MATERIALS SCIENCE AND NANOENGINEERING PH.D. THESIS, JUNE 2024

Thesis Supervisor: Assoc. Prof. OZGE AKBULUT

Keywords: colloidal processing, 3D-printing, prototyping, ceramics processing, low-volume fabrication

Ceramics stand out for their long-term durability, high thermal stability, strength, and chemical resistance, making them ideal for extreme applications. However, these desirable properties often pose challenges in the near-net shaping of ceramics. Currently, there is a lack of cost- and energy-effective processing routes for advanced ceramics that align with rapid prototyping and low-volume manufacturing setups. There is a pressing need for alternative methods tailored specifically for ceramics. Recently, we have shown the preparation of self-standing, malleable doughs of advanced ceramics. These doughs are generated through the introduction of a single additive in an aqueous suspension and in under two minutes, they can be shaped by hand or pushed into a mold. The single additive is a grafted random copolymer that induces polymer bridging among ceramic particles leading to homogeneous coagulation. After a short period of drying, the green bodies can be near-net shaped at a benchtop CNC.

The self-standing, malleable doughs represent a significant opportunity in ceramic processing, they can be machined with forces that are below 10 N and potentially, the waste and faulty samples can be recycled fully. This enables no material leak, time- and energy-efficient processing; along with the use of existing setups, the method can revolutionize low-number manufacturing and prototyping for advanced ceramics.

In this thesis, I expanded the materials portfolio of these doughs from oxides to a multi-component nitride. In addition, I parameterized the machining of alumina to serve standardization of this processing technique and paved the way for adaptation of this technique by the establishments with no or minimum materials domain knowledge.

ÖZET

TEZGAH ÜSTÜ, DÜŞÜK MİKTARDA ÜRETİM VE PROTOTİPLEMEYİ KOLAYLAŞTIRAN İLERİ SERAMİK ŞEKİLLENDİRİLEBİLİR HAMURLARIN TASARIMI

AYŞE AY

MALZEME BİLİMİ VE NANOMÜHENDİSLİK DOKTORA TEZİ, HAZİRAN 2024

Tez Danışmanı: Doç. Dr. ÖZGE AKBULUT

Anahtar Kelimeler: kolloidal sistemler, 3 boyutlu yazım, prototipleme, seramik işleme, düşük-hacimli üretim

Seramikler, yüksek termal stabiliteleri, dayanıklılıkları ve kimyasal dirençleriyle öne çıkarak zorlu uygulama alanlarında kullanım için ideallerdir. Bununla birlikte, bu arzu edilen özellikler çoğu zaman seramiklerin nete yakın şekillendirilmesini engeller. Şu anda, ileri seramikler için hızlı prototipleme ve düşük hacimli üretim sistemleriyle uyumlu, maliyet ve enerji açısından verimli işleme yollarının eksikliği bulunmaktadır. Seramiklere özel olarak uyarlanmış alternatif yöntemlere acil bir ihtiyaç vardır. Son zamanlarda ileri seramiklerden elle şekillendirilebilir hamurların hazırlanışını gösterdik. Bu hamurlar, sulu bir süspansiyona tek bir katkı maddesinin eklenmesiyle üretilmekte, iki dakikadan kısa bir sürede elle şekillendirilebilmekte veya kalıplanabilmektedir. Tek katkı maddesi, homojen koagülasyonu sağlayarak seramik parçacıkları arasında polimer köprülenmesini indükleyen graftlı rastgele bir kopolimerdir. Hamurlardan elde edilen yeşil gövdeler, kısa bir kurutma süresinin ardından tezgah üstü CNC'de nete yakın şekillendirilebilir.

Elle şekillendirilebilen bu hamurlar seramiklerin işlenmesinde önemli bir fırsat sunmaktadır; 10 N'nin altındaki kuvvetlerle işlenebilmekte ve potansiyel olarak atık ve hatalı numuneler bu sayede tamamen geri dönüştürülebilmektedir. Bu, malzeme kaybının önlenmesini, zaman ve enerji açısından verimli işlemeyi de mümkün kılmaktadır. Mevcut kurulumların kullanılmasıyla birlikte bu yöntem, ileri seramikler için düşük hacimli üretim ve prototip oluşturmada devrim yaratabilir.

Bu tezde, bu hamurların malzeme portföyünü oksitlerden çok bileşenli nitrür içeren ileri seramik sistemlerine genişlettim. Ayrıca alüminanın CNC ile işlenmesini, bu tekniğin standardizasyonunu sağlayacak şekilde parametrelendirdim ve bu tekniğin, malzeme bilgisi olmayan veya minimum düzeyde olan işletmeler tarafından uyarlanmasının önünü açtım.

ACKNOWLEDGEMENTS

I would like to express my gratitude to my supervisor, Assoc. Prof. Ozge Akbulut, for her support throughout my PhD journey. She is and will remain a role model for the rest of my life, not only for her scientific achievements but also as a powerhouse of energy that fuels everything forward, serving as an inspiration for boundless determination. Her patience, expertise, and lightning-fast responses have been invaluable. I owe a debt of gratitude to Dr. Ahu Gumrah Dumanli for introducing me to Assoc. Prof. Ozge Akbulut, providing me with hands-on characterization experience during my master's studies that has greatly benefited my PhD journey. I also appreciate Dr. Ahu Gumrah Dumanli for her co-supervision on several projects on which we collaborated.

My heartfelt thanks extend to my thesis progress committee members, Prof. Alpagut Kara and Prof. Fevzi Cakmak Cebeci, for their feedback and support. Prof. Yusuf Ziya Menceloglu, Prof. Mali Gulgun, and Assoc. Prof. Damla Eroglu Pala, thank you for being there with a single call and allocating your precious time. I am deeply grateful to Dr. Gokhan Kula and Furkan Buluc of MDA Ceramics Inc. for generously sharing their expertise in ceramics, and to Assoc. Prof. Burcu Saner Okan and Nargiz Aliyeva for sharing their insights on life-cycle assessment. Prof. Mirko Kovac's kind allocation of his research grant and Dr. Yunus Govdeli's supervision, when I needed guidance in aerodynamics, have been instrumental in my journey to diversify my project. Dear Asst. Prof. Ahu Akin, thank you for being a lifetime mentor, dear Prof. Kutlu Ulgen, Prof. Nihan Nugay, Assoc. Prof. Kerem Uguz, and Dr. Anna Regoutz, I always feel your support.

My fellow MAT-GRAD friends, Ekin Berksun, Shahrzad Sajjadivand, Ogeday Rodop, Cagla Girisken, Yasemin Akyol, Aybike Mine Ersin, Ahmet Can Kirlioglu, Gizem Beliktay, Aleyna Beste Ozhan, and Isik Arel, my QUAL buddies, specifically, Yelda Yorulmaz, Melih Can Tasdelen, and Onur Zirhli, your friendship means a lot to me. Maryam Sepehri, Saygun Guler, Ozberk Ozturk, Osman Sahin, and Oguz Albayrak of SU-MEMS, thank you for always being at the dinner table (6 pm sharp). Emre Aydemir thanks for being my solid-state pal. Ceylin Isiklar, I truly thank you for being my right hand in the lab countless times when I needed you the most.

My TRIO, Pinar Akarsu and Ayca Cisil Telorman, your companionship serves as a

comforting cushion, easing the weight of Bundesliga. Mumtaz Cahit Vural and Elmas, thank you for being such caring, adaptive, and supportive, being the ear and purr that I need, the last bits won't be the same without you.

Finally, dear Mom, Neriman, and Dad, Sabahaddin, we find ourselves at a crossroads, faced with a challenging yet ultimately rewarding decision to make together. I am deeply grateful to know that your support has been, and will always be, by my side.

To my family

TABLE OF CONTENTS

LIST OF TABLES

LIST OF FIGURES

LIST OF ABBREVIATIONS

AMPS	:	2-acrylamido-2-methylpropane sulfonic acid
AA	:	Acrylic acid
ASTM	:	American Society for Testing and Materials
ANOVA	:	Analysis of variance
P_{app}	:	Applied pressure
Ra	:	Arithmetic mean roughness
W	:	Average weight of meshes
A_p	:	Basal area of the corresponding calibration weight
k	:	Boltzmann's constant
c	:	Charge of proton
cDIW	:	Coaxial direct ink writing
CNC	:	Computer numerical control
Ct	:	Control
C	:	Core ink
DI	:	Deionized
D_2O	:	Deuterium oxide
DLS	:	Dynamic light scattering
F	:	Force
FTIR	:	Fourier-transform infrared spectroscopy
GPS	:	Gas pressure sintering
GPC	:	Gel permeation chromatography
g	:	Gravity
HCl	:	Hydrochloric acid
HPC	:	Hydroxypropyl cellulose
ICP-OES	:	Inductively coupled plasma-optical emission spectrometry
ID	:	Inner diameter
LC	:	Length of the inner nozzle
LVR	:	Linear viscoelastic region
LC	:	Loading capacity
G"	:	Loss modulus
MgO	:	Magnesia

MA	:	Maleic anhydride
m	:	Mass
Mx	:	Mesh
MC	:	Methyl cellulose
DMAPMA	:	N-(3-(Dimethylamino)propyl)methacrylamide
NMR	:	Nuclear magnetic resonance spectrometry
OD	:	Outer diameter
PEG	:	Poly(ethylene glycol)
PVA	:	Poly(vinylalcohol)
PCL	:	Poly(ε-caprolactone)
PDI	:	Polydispersity index
Pr	:	Pore factor
KPS	:	Potassium peroxydisulfate
r	:	Radius of the core nozzle
SEM	:	Scanning electron microscopy
S	:	Shell ink
ALG	:	Sodium alginate
NaOH	:	Sodium hydroxide
G'	:	Storage modulus
T	:	Temperature
E_f	:	Total amount of fertilizer encapsulated in fibers
Tx	:	Traditional
U	:	Uniformity factor
HV	:	Vickers hardness
Q	:	Volumetric flow rate
XRD	:	X-ray diffraction spectroscopy
YSZ	:	Yttria-stabilized zirconia

LIST OF SYMBOLS

λ_D	:	Debye length
τ_ω	:	Shear stress at the inner nozzle wall
ε_x	:	Shrinkage in x direction
η	:	Viscosity
τ_f	:	Yield point

Chapter 1

1. INTRODUCTION

In this thesis, near-net shaping of advanced ceramics, as well as the design and prototyping of agrochemical release systems were reported. The thesis is divided into two parts, comprising five chapters in total. Part one covers the colloidal processing of two technical ceramics, namely a modal ceramic, α-alumina, and a multi-component nitride system, SiAlONs. The second part focuses on the colloidal processing of a commercial-grade fertilizer. The first chapter provides an introduction and summarizes the main findings of each chapter in the thesis.

In Chapter 2, a facile, benchtop method for producing self-standing, malleable doughs of alumina –the most used technical ceramic– for CNC machining was introduced. A single additive, poly(ethylene glycol)-grafted random copolymer of acrylic acid and N-(3-(Dimethylamino)propyl)methacrylamide, at 0.75 wt. % relative to α-alumina, was used to formulate malleable alumina doughs (75.3 wt. %) in under 2 minutes. The optimal machining parameters for achieving the best surface quality were identified for tools with two different diameters. Additionally, the recycling potential of α-alumina was demonstrated, incorporating up to 30 wt. % from intentionally broken parts at the green state. This cost-effective and accessible methodology not only enhances the precision and quality of ceramic production but also promotes sustainability by incorporating a significant recycling component, paving the way for greener ceramic manufacturing practices.

In Chapter 3, SiAlONs, a multi-component ceramic system, were studied. Their use frequently requires custom shapes, and they are usually machined at the green state for

their near-net-shaping. An additive, a copolymer of poly(ethylene glycol)-grafted acrylic acid and 2-acrylamido-2-methylpropane sulfonic acid, was used to coagulate SiAlON suspensions, forming a malleable dough with 72.7% SiAlON content. The mechanical and microstructural properties of the machined dough were compared with a wear part made from the same powder but fabricated through uniaxial pressing. The fabrication and prototyping of complex shapes using conventional machining techniques were demonstrated.

In the second part, a flexible agrochemical release system that boosts plant growth was devised through room temperature and solvent-free processing. A core-shell mesh fiber system through coaxial direct ink writing for the release of fertilizer was fabricated. The viscosity and the printability of the core ink were tuned by dissolving the fertilizer in an aqueous hydroxypropyl cellulose and poly(ethylene glycol) solution. As the shell ink, a polysaccharide-based formulation based on methylcellulose and sodium alginate was utilized to encapsulate the core ink and prolong the release. The core-shell meshes with sub-mm diameter fibers inherently granted a high core loading capacity of ~86.8 wt. %. The efficacy of the 3D-printed controlled release of the fertilizer was tested using a plant growth assay. The meshes increased wheat shoot growth by ~1.7-fold and ~1.5-fold compared to the control (no chemical) and traditional (where the fertilizer was applied directly into soil) application, respectively, in four weeks. In addition, a 30% reduction in the fertilizer load produced ~1.2-fold growth compared to the traditional application. This route will enable a zero-waste fabrication of controlled-release systems, offering a promising solution in terms of both environmental sustainability and efficient multiple-nutrient delivery.

Chapter 2

2. OPTIMIZING MACHINING PARAMETERS OF A MODAL CERAMIC SYSTEM ON A BENCHTOP: MALLEABLE ALUMINA DOUGHS FOR LOW-NUMBER PRODUCTION

This chapter is written based on the article “Benchtop machining of self-standing alumina doughs for low-number fabrication and prototyping” that was submitted to ACS Applied Materials & Interfaces in January 2024 and received feedback for revision in March 2024.

2.1.Introduction

Advanced ceramics are known for their high thermal stability, mechanical strength, and chemical and wear resistance (Ayode Otitoju et al., 2020; Heimann, 2010; Riedel et al., 2008), making them suitable for demanding applications such as ultra-high-temperature applications, implants, and ballistic armor (J. Ma et al., 2003; Sigmund et al., 2000). However, their intrinsic hardness and brittleness pose challenges in shaping them into complex structures (Dhara & Su, 2005; Mohanty, Rameshbabu, et al., 2013). Computer numerical control (CNC) machining, commonly used for metals (Childs, 2,000; Juneja, 2003; Pabla & Adithan, 1994), has been adapted for ceramics to achieve intricate designs (Kastyl et al., 2020), however, it requires significant investment in machinery and skilled labor. Machining of sintered ceramics involves high forces and energy consumption, leading to tool wear and frequent replacement of expensive tooling (Chang & Lin, 2012; Gonçalves Júnior et al., 2019; Liu et al., 2017; Zhai et al., 2021). Moreover, recycling faulty products and scrap is also energy-intensive (Wei et al., 2023).

Alternatively, ceramics can be processed in their green state, where the loosely consolidated structure requires lower forces and results in less tool wear (Dadhich et al.,

2015; Demarbaix et al., 2020; Seesala & Dhara, 2021). Powder compaction methods such as hot (HIP) and cold isostatic pressing (CIP) are cost-effective for high-volume production due to their batch-processing nature, however, they require expensive molds and equipment (Figure 2.1) (Seesala et al., 2021; Vaben & Stöver, 1997). HIP involves applying high pressure and temperature (Figure 2.1) to a ceramic material, which enhances its density and mechanical properties by eliminating internal voids and defects. This method leads to ceramics with superior strength, toughness, and resistance to wear and corrosion, making it ideal for high-performance applications. HIP requires expensive equipment and significant energy consumption due to the high temperatures and pressures involved, making it costly for small-scale or low-volume production (Atkinson & Davies, 2,000; Bocanegra-Bernal, 2004; Davis, 1991). Additionally, the process duration can be lengthy, further increasing production costs (Atkinson & Davies, 2,000; Bocanegra-Bernal, 2004). CIP, on the other hand, applies pressure at room temperature, ensuring uniform compaction of ceramic powders (Figure 2.1). This process produces green bodies with consistent density and can be used to create complex shapes that are challenging to achieve with other methods. CIP, while less energy-intensive, often requires a subsequent sintering step to achieve the desired material properties, which can introduce additional time and expense. Despite these benefits, both HIP and CIP have drawbacks in producing very fine or intricate features due to the inherent nature of the pressing techniques.

To create a machinable green body using a slurry-based approach, ceramic particles are embedded in a polymeric matrix, which imparts sufficient ductility and resilience during machining (Prabhakaran et al., 1999; Su et al., 2008). This process often involves using multiple chemicals including binders and dispersants, which need to be removed later, with each laboratory and company having its unique formulation (Figure 2.1) (J. Kim et al., 2022). Gel-casting involves using a monomer solution that polymerizes to form a rigid gel, providing good shape retention and uniform microstructure. It offers a balance between cost and precision, suitable for small to medium production volumes. Protein coagulation casting uses proteins to bind ceramic particles, which then coagulate and form a solid structure upon heating (Yin et al., 2009). These methods are particularly useful for creating complex shapes and are relatively cost-effective for small-scale production. However, they often fall short in achieving the same level of density and mechanical properties as isostatic pressing. Thus, there is a need for a universally accepted, readily available, and cost-effective method for consolidating green ceramics.

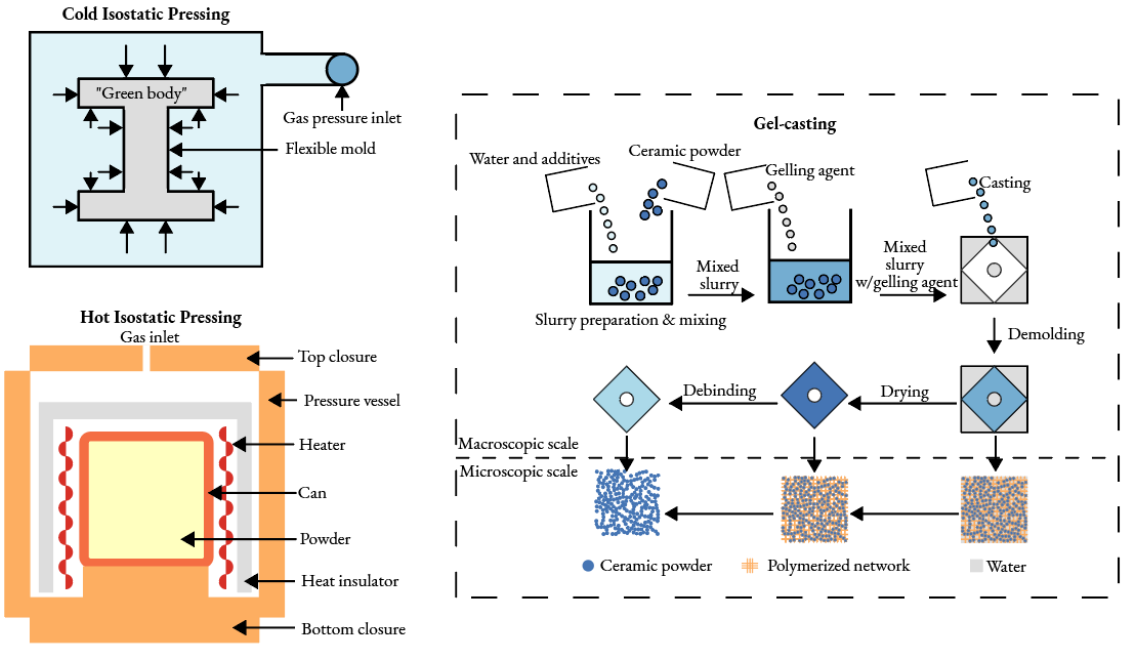

Figure 2.1 Schematics of green body preparation methods and hot isostatic pressing

Recently, Akbulut research group has shown the preparation of malleable, self-standing doughs of yttria-stabilized zirconia (YSZ) (Zemberekci et al., 2021) and magnesia (MgO) (Ozhan et al., 2023) through the use of a single additive at low amounts (<2 wt. %). These additives, which are random copolymers with ionic backbones, effectively coagulate highly concentrated aqueous ceramic suspensions (>60 wt. % particles) through polymer bridging, resulting in a dough-like consistency. The self-standing dough addresses multiple issues that current organic matrix-based or powder compaction methods cannot solve. The dough can be manually shaped or pressed into molds (Figure 2.2) without requiring a controlled environment or specialized equipment for preparation. Due to comprising a minimal quantity of a single organic formulation, they are highly reproducible and thus applicable to standardization. In this thesis, the self-standing dough formulation is expanded to another oxide, α-alumina (Figure 2.2).

Alumina, the most frequently used advanced ceramic (Ben-Nissan et al., 2008), was used as a modal ceramic to demonstrate the standardization of CNC machining for low-number production and prototyping on a benchtop (Figure 2.2). A poly(ethylene glycol) (PEG)-grafted copolymer of N-(3-(Dimethylamino)propyl)methacrylamide (DMAPMA) and acrylic acid (AA), at 0.75 wt. % (with respect to the weight of alumina) to homogeneously coagulate ~75.3 wt. % aqueous alumina suspensions (Figure 2.3) was utilized. Thereafter, the machining parameters were optimized by varying the cutting tool diameter (1 mm and 2 mm), spindle (5,000–30,000 rpm), and cutting speeds (1,000–1,800

mm/min) and the interaction between the green body and the tool was assessed, as well as the tool wear.

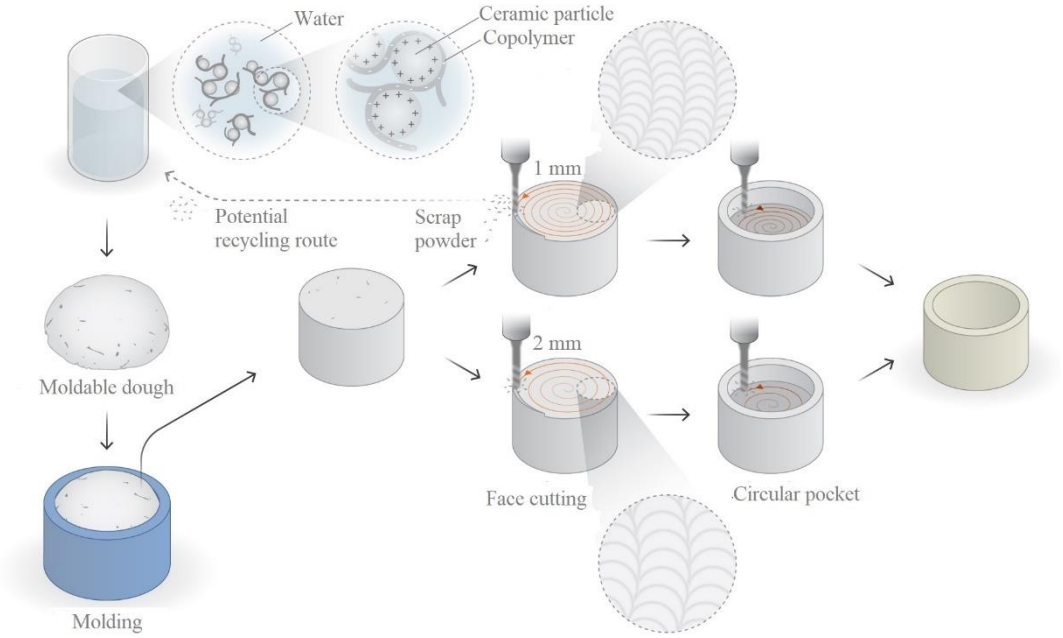

Figure 2.2 The fabrication of crucibles from self-standing alumina dough using green machining

The surface quality after machining was tracked by profilometry, optical microscopy, and scanning electron microscopy (SEM). Upon sintering, all hand-shaped objects demonstrated isotropic linear shrinkage of ~19% from the dried state to the sintered state and reached a density of 3.93±0.29 g/cm^3 (~99.5% t.d.). The hardness of the sintered samples was measured as 15.16±1.15 GPa in alignment with other reports (Khan et al., 2016; Lee et al., 2019). Additionally, a potential recycling route for the green bodies was introduced by incorporating up to 30 wt. % scrap, which was sourced from intentionally broken green parts.

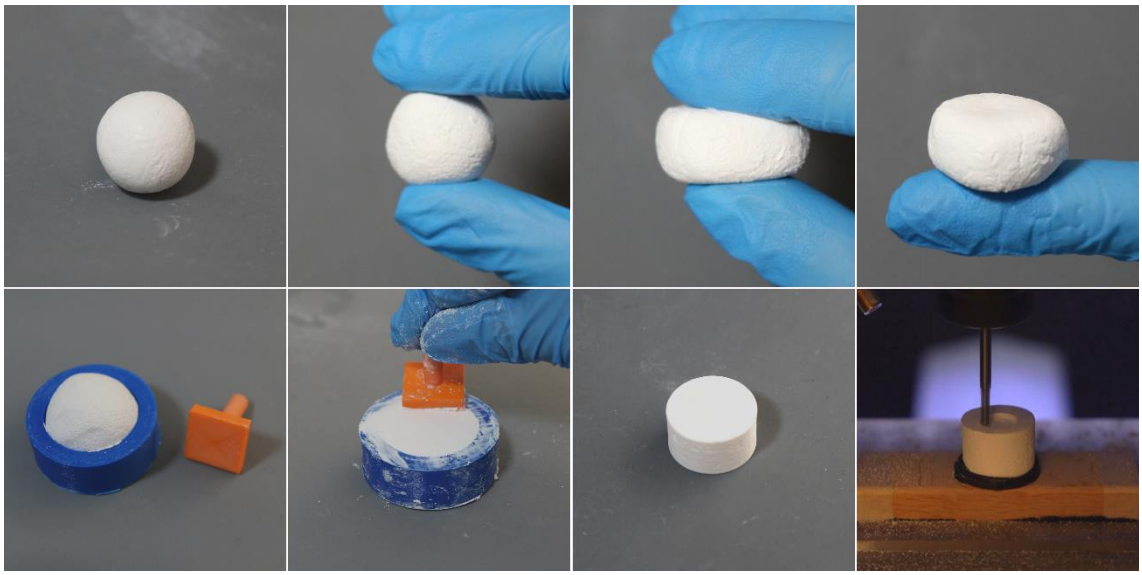

Figure 2.3 A malleable, self-standing dough comprising 75.3 wt. % alumina and 0.75 wt. % copolymer relative to the weight of alumina, its molding, and green machining to produce a crucible

Self-standing, malleable doughs (Figure 2.3) have the potential to standardize green-state ceramic machining. This research represents the initial effort to systematically parameterize the green machining of alumina. This accessible approach can be readily applied to various ceramics, expanding the materials portfolio for energy-, cost-, and resource-efficient processing, particularly for low-volume production and prototyping.

2.2.Materials and methods

2.2.1. Materials

Alpha alumina was acquired from US Research Nano Materials, Inc. AA (99%), DMAPMA (99%), and potassium peroxydisulfate (KPS, ≥99.0%) were sourced from Sigma-Aldrich. PEG (MW=1,000 g/mol), hydrochloric acid (HCl, 37%), sodium hydroxide (NaOH, 97%), and maleic anhydride (MA, 99%) were purchased from Merck. All chemicals were used without further purification, and solutions were prepared with deionized (DI) water having a resistivity of 18.2 MΩ·cm, with the pH adjusted to 7.

2.2.2. Synthesis of the additive and the preparation of the ceramic suspensions

The procedure to synthesize MA-esterified PEG (MAPEG) was conducted following the method proposed by Lu et al. (Lu et al., 2010). The resulting MAPEG was used for polymerization without purification. For the aqueous free-radical polymerization of DMAPMA, AA, and MAPEG, a mixture containing 0.05 mol of DMAPMA, 0.05 mol of AA, and 0.02 mol of MAPEG (Mn=∼1156 g/mol) was dissolved in 100 mL of DI water. This solution was transferred to a 250 mL three-neck flask equipped with a reflux condenser. The flask was purged with nitrogen gas and stirred magnetically as the temperature was increased to 50 °C. At this point, a 75 mL aqueous solution of KPS (initiator) was slowly added dropwise over 10 minutes, corresponding to 1 mol% of the total moles of comonomers (0.12 moles). The temperature was then elevated to 70 °C, and the reaction was allowed to proceed for 12 hours.

The composition of the copolymer (Figure 2.4, Table 2.1, and Table 2.2) was determined via nuclear magnetic resonance spectrometry (NMR, Varian Unity Inova 500 MHz, Agilent Technologies, USA). The polymerization medium was precipitated in acetone, vacuum dried at 70 °C for 12 hours, and subsequently dissolved in deuterium oxide (D_2O, 99.90%).

Gel permeation chromatography (GPC) was used to determine the molecular weight distribution (Mw and Mn) and the polydispersity index of the copolymer (Table 2.2). This analysis was performed using an Agilent 1260 Infinity system with Waters Ultrahydrogel 250 and 500 columns, coupled with a refractive index detector, operating at a flow rate of 0.7 mL/min. Before measurement, the copolymer was dissolved in a phosphate buffer (pH=7.2) at a concentration of 5 mg/mL.

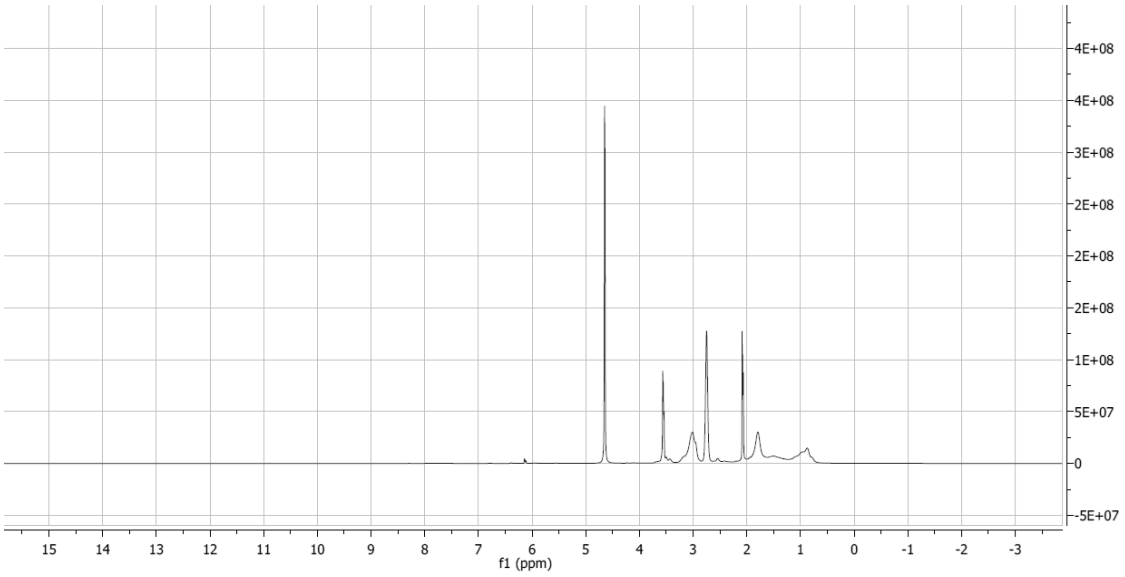

Figure 2.4 ^{1}H NMR spectrum of the DMAPMA/AA/PEG copolymer in deuterium oxide (D_2O) (The peak at ~4.65 ppm originates from D_2O solvent in the measurement.)

Table 2.1 ^{1}H NMR absolute integral values associated with each functional group of the copolymer

Region	Range	Functional group	Absolute Integral
1	1.93−1.65	-CH_2-CH	17.29
2	2.13−2.01	-	15.35
3	2.84−2.64	$N(CH_3)_2$	30.55
4	3.21−2.90	N-CH_2	23.92
5	3.61−3.46	CH_2-CH_2-O	12.89

Table 2.2 Properties and characteristics of the copolymer

Molar concentration (DMAPMA:AA:PEG)	0.05:0.05:0.02
Molar feed ratio (DMAPMA:AA:PEG)[a]	25:25:0.6
DMAPMA/AA[a]	8.8:10
PEG/DMAPMA+AA[a]	1.29:100

Molecular weight (M_n) (kg/mol^{-1})[b]	5.64
PDI (M_w/M_n)[b]	1.55

[a] Determined by ^{1}H-NMR, [b] Determined by gel permeation chromatography (GPC)

2.2.3. Electrokinetic studies

A zeta potential analyzer (Malvern Instruments, Ltd., Zetasizer Nano series, UK) with a 633 nm laser and a scattered light detector set at a 173° angle was used to assess the electrokinetic behavior of alumina nanoparticles. 1 mg, 2 mg, 5 mg, and 10 mg nanoparticles were separately dispersed in 100 mL of deionized water and ultrasonicated in a bath sonicator for 5 minutes, and alumina suspensions with a concentration of 0.001 wt. %, 0.002 wt. %, 0.005 wt. %, and 0.01 wt. % were obtained. An aqueous copolymer solution was added gradually to these suspensions to achieve a copolymer concentration between 0.25–1.5 wt. %. The suspensions were then ultrasonicated for another 5 minutes and mechanically stirred for 10 minutes before measurements. Three measurements, each consisting of at least 15 runs, were performed at 25 °C. The zeta potential and hydrodynamic radius for each copolymer concentration were determined by averaging these three measurements and reported along with their standard deviations.

Alumina suspensions were prepared at concentrations of 0.025 wt. %, 1 wt. %, and 30 wt. % without the introduction of copolymers. To analyze floc sizes, 0.75 wt. % copolymer relative to the weight of alumina particles was introduced to these suspensions. These suspensions were sonicated for 1 hour within a temperature range of 19–24 °C. Using the Hydro SM device, micro drops were added until an obscuration level of 20% was achieved. Six measurements, each lasting 30 seconds, were taken to determine the volume density percentage and the particle/floc size distribution, utilizing a Mastersizer 3000E (Malvern Instruments, UK).

2.2.4. Preparation of the green bodies

To determine the maximum solid loading resulting in a dough-like consistency, an aqueous copolymer solution was gradually added to pre-weighted α-alumina. After

incorporating the copolymer, the mixture was hand-mixed for 2 minutes until it reached a dough-like consistency. Digital images of the self-standing alumina dough were captured using a Canon EOS 650D camera (Figure 2.3). Before molding, the particle loading was evaluated using a solid content analyzer, and a particle loading of ~77.6 wt. % was achieved with 0.75 wt. % additive. For example, a 100 g dough consisted of 75.3 g of particles, 24.1 g of DI water, and 0.6 g of additive. The volumetric composition of the dough was 44.9% (v/v) alumina, 0.7% (v/v) additive, and 54.4% (v/v) DI water. Throughout all compositions, the copolymer amount is expressed relative to the weight of the alumina particles.

2.2.5. Rheological characterization

An Anton-Paar MCR92 rheometer equipped with a parallel plate geometry of 25 mm with a fixed gap size of 1 mm was used to characterize the rheological behavior of ceramic suspensions at room temperature (25 °C). Samples with 67.8, 72.5, 75.3, and 77.1 wt. % solid loading containing 0.75 wt. % additive were prepared. The shear rate was varied from 0.1 to 100 s^{-1}. To obtain the storage and loss moduli in dynamic mode, the angular frequency was kept constant at 10 rad/s, while the strain increased from 0.001 to 100%.

2.2.6. Sintering profile, density measurements, and shrinkage

The sintering of green bodies was conducted in a MoS-B 180/4 chamber furnace (Protherm, Turkiye). The furnace temperature was gradually increased to 1650 °C at a rate of 1 °C/min, with a dwelling time of 3 hours.

The density of the sintered bodies was measured using Archimedes' method, employing an AND GR-200 analytical scale and a custom setup to measure the mass of the submerged sample in DI water at 22 °C (ρ_{water}=0.99777 g/cm³).

The percentage of shrinkage in cubic alumina samples during drying and sintering was calculated using linear dimensional measurements. A K-factor was introduced to quantify the percentage of anisotropic sintering shrinkage using Eq. (2.1)-(2.3) (Heunisch et al., 2010):

$$K_{xy} = 100 \times (1 - \varepsilon_x/\varepsilon_y) \quad (2.1)$$

$$K_{xz} = 100 \times (1 - \varepsilon_x/\varepsilon_z) \quad (2.2)$$

$$K_{yz} = 100 \times (1 - \varepsilon_y/\varepsilon_z) \quad (2.3)$$

Where ε_x, ε_y, and ε_z represent shrinkage in the x, y, and z directions, respectively. The shrinkages were calculated along the x, y, and z directions for five cubical samples, and the average is reported.

2.2.7. Mechanical characterization

The Vickers hardness (HV) was assessed via an indenter (Emco-Test Prüfmaschinen GmbH, Austria) with a 1 kg load for 15 seconds, following the ASTM-C1327-08 standard, after polishing the samples in an automated polishing machine (TegraPol-25, Struers). The average of five measurements for each sample was employed to determine the Vickers hardness by analyzing the radial cracks generated during the indentation test using Eq. (2.4) (ASTM, 2022):

$$HV = 0.0018544 \, (P/d^2) \quad (2.4)$$

where P is the load (N), and d is the average length of the two diagonals of the indentation (mm).

2.2.8. Machining

Green bodies were dried at room temperature (20.4±1 °C) for 24 hours at a relative humidity of 52%. Machining was performed using a bench-top 3-axis REVO M1A CNC milling machine (REVO, Turkiye) equipped with 1 mm and 2 mm diameter tungsten carbide flat-end mill cutting tools (LPKF Laser & Electronics AG, Germany). Tungsten carbide was chosen for its durability and cost-effectiveness (Johansson et al., 2019; Micallef et al., 2020; Rizzo et al., 2020), while the flat-end mill geometry was selected to achieve a smooth surface finish, ensuring precision and dimensional accuracy (Vickers & Quan, 1989).

A major challenge in green machining is securely mounting the green bodies to the CNC table (Mohanty, Rameshbabu, et al., 2013). Mechanical clamping methods presented

difficulties due to the brittleness and limited mechanical strength of the green compacts, as excessive clamping pressure could potentially compromise their integrity. Vacuum clamping was also not a viable option due to the porous nature of the green compacts. Additionally, the machining process introduced vibrations which can lead to detachment and breakage of the samples. To address these challenges, a practical solution that involved drilling holes with dimensions matching those of the samples on a hardwood panel was employed (Figure 2.11b). The samples were then securely fixed into these openings using adhesive tape (Aerovac Composites One, USA). This approach ensured that the ceramic substance was surrounded by the tape and minimized the movement during the machining process.

2.2.9. Surface characterization

The quality of the machined surface was assessed by optical microscopy (Sanqtid, China) and surface profilometry (Dektak 6M, USA) before and after sintering. Arithmetic mean roughness (Ra) was measured by surface profilometry, applying a force of 2 mg, along and perpendicular direction of machining using a Stylus-type profilometer with a 12.5 μm tip radius. The horizontal distance traveled was set to 3 mm and 6 mm, for 1 mm and 2 mm tools, respectively. The distance traveled for the 2 mm tool was increased intentionally to cover more area. SEM (Leo Supra 35VP field emission SEM) was used to evaluate surface morphology at an acceleration voltage of 3 keV without any coating after sintering.

2.3.Results and discussion

2.3.1. Formulating machinable alumina green bodies

To determine the minimum amount of copolymer required for preparing a dough, the stability of alumina dispersions was evaluated using zeta potentiometry. The pristine alumina (without any copolymer introduction) suspension exhibited a zeta potential (ζ) of -34 mV at around pH 7 (Figure 2.5). At lower additive concentrations, the copolymer molecules did not sufficiently cover the particle surfaces, resulting in the formation of a robust network through inter-particle adsorption of long-chain molecules (Mohanty, Das,

et al., 2013). When 0.75 wt. % copolymer was added, the suspended powder surfaces reached the highest surface charge of -43 mV, indicating monolayer coverage of the polymers (Figure 2.5).

Additionally, the average hydrodynamic diameter (h_d) initially decreased with increasing copolymer concentration but then increased beyond 0.75 wt. %. The smallest h_d was 211 nm, corresponding to the copolymer amount necessary for complete surface coverage of the particles (Figure 2.5). Beyond this optimal point, excess un-adsorbed polymer molecules in the aqueous solution compressed the electrical double layers, reducing the surface charge and zeta potential (Mohanty, Das, et al., 2013). The increase in h_d with polymer dosages exceeding 0.75 wt. % can be attributed to mechanisms such as polymer−polymer/free-polymer interactions and bridging flocculation (Doroszkowski, 1999; Furusawa et al., 1992; S. Kim et al., 2015; Piculell & Lindman, 1992b; Vincent et al., 1980).

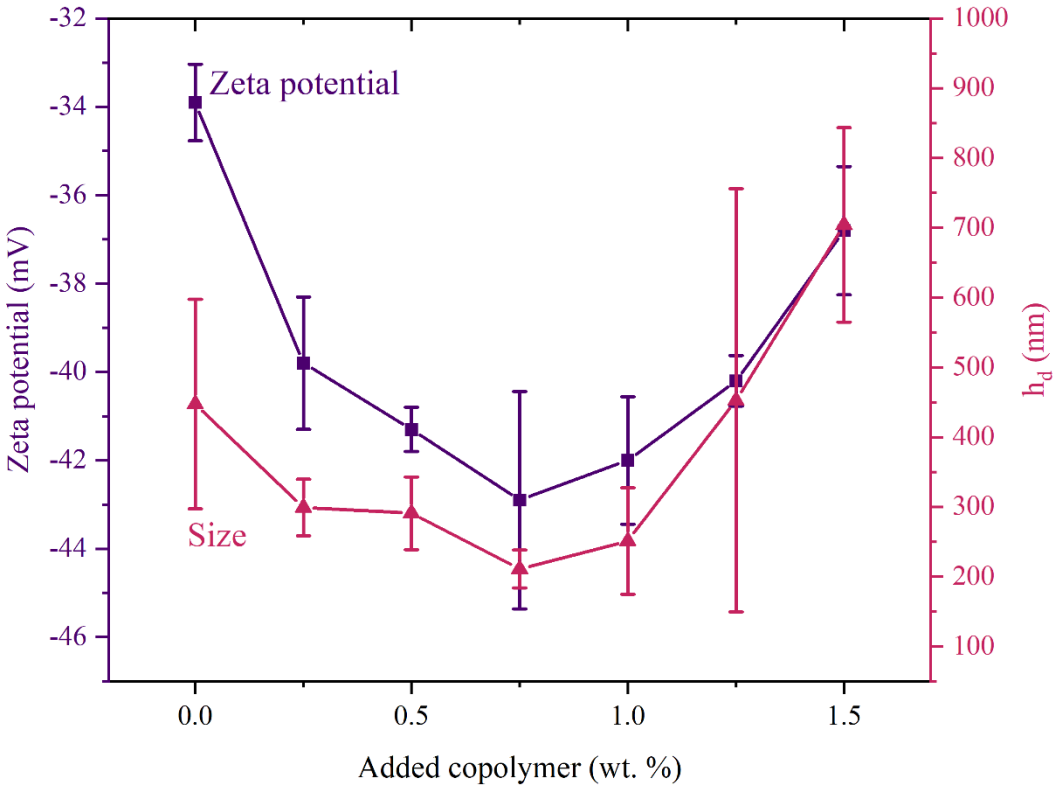

Figure 2.5 Zeta potential and hydrodynamic diameter of alumina particles with varying copolymer content (Line plot used for better data visualization.)

Figure 2.6a illustrates the size (h_d) distribution and intensity (%) of a 0.001 wt. % alumina suspension with varying copolymer concentrations. The primary peaks fall between 0 and 500 nm for all samples. The sample without copolymer (0 wt. %) shows a sharp peak,

indicating a narrow size distribution of well-dispersed ceramic particles. As the polymer concentration increases, the peaks shift slightly and broaden, indicating changes in particle size distribution and potential aggregation. As the polymer concentration increases from 0.25 wt. % to 1.0 wt. %, the intensity peaks decrease and broaden, suggesting the start of particle aggregation. Beyond 1.0 wt. %, the peaks broaden further, and additional peaks appear, reflecting more complex interactions between the copolymer and alumina particles. Higher polymer concentrations (1.75 wt. % and 2.0 wt. %) show secondary peaks at larger diameters (around 5000 nm), indicating the formation of larger aggregates or clusters. Therefore, while small amounts of polymer (up to around 1.0 wt. %) effectively bind alumina particles and maintain a controlled size distribution, excessive copolymer addition leads to significant aggregation, forming larger particle clusters and broadening the size distribution.

In Figure 2.6c, alumina particles without copolymer showed peaks concentrated around 250 nm at lower solid loadings (0.001 wt. % and 0.002 wt. %). As the solid loading increased to 0.005 wt. % and 0.01 wt. %, the peaks broadened and shifted to larger sizes (up to 1,000 nm), indicating significant aggregation at higher solid loadings. This suggests that particles are well-dispersed at lower solid loadings, whereas higher loadings result in considerable aggregation. Figure 2.6d demonstrates that adding copolymer to the ceramic particles at 0.75 wt. % broadens and shifts the intensity peaks compared to those without polymer. At 0.001 wt. %, the peak remains narrow but shifts slightly to larger sizes. At higher solid loadings (0.005 wt. % and 0.01 wt. %), the peaks are much broader and shift to larger sizes, indicating enhanced aggregation due to the copolymer. This broadening and shift in size distribution with increased solid loading show that aggregation occurs in both cases, but the effect is more pronounced with the copolymer, suggesting it promotes aggregation at higher solid loadings.

Additionally, the formation of dough at different solid loadings with increasing additive content was visually tracked (Figure 2.6b). At 72.5 wt. % solid loading, the suspension remained sticky regardless of the additive amount. However, at 77.1 wt. % solid loading, prominent cracks were observed. Non-sticky, malleable dough formulations with no clumping were achieved with 0.75 wt. % and 1 wt. % additive, with 0.75 wt. % being selected for further studies due to its optimal performance.

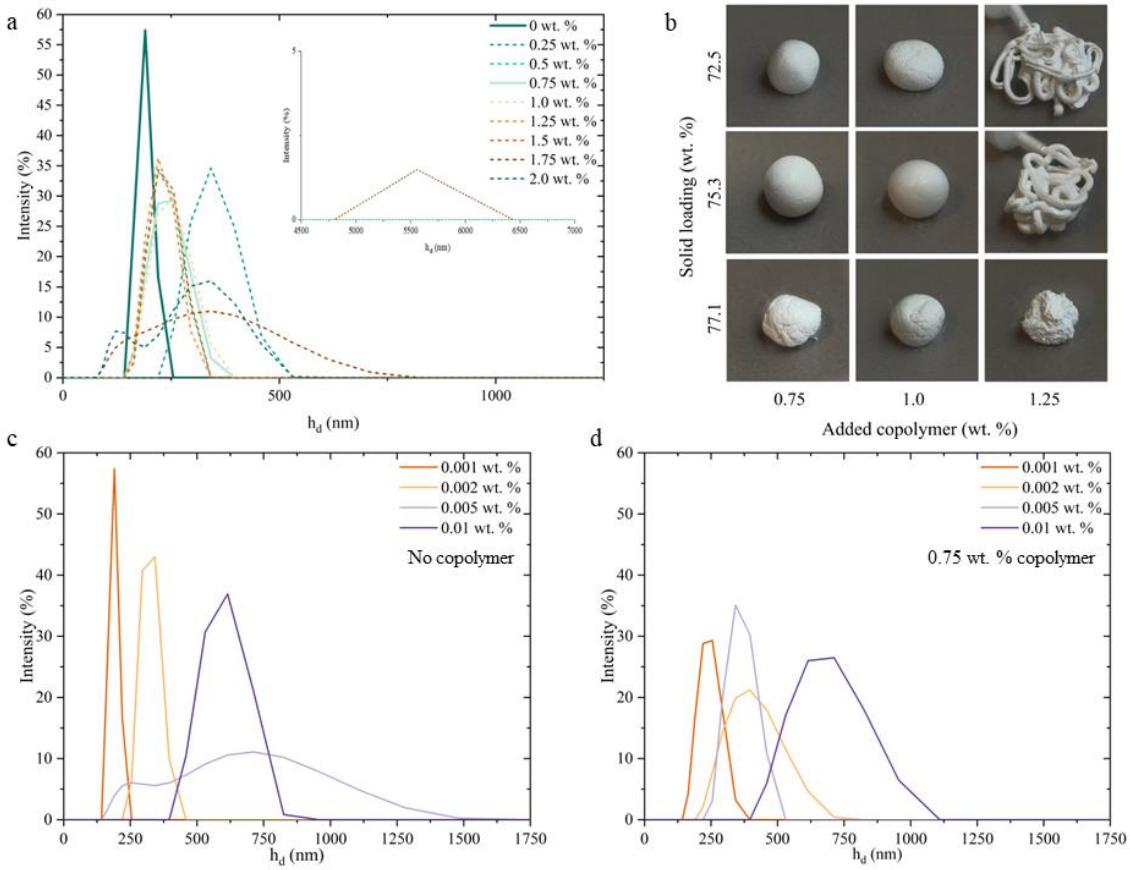

Figure 2.6 a) Intensity-weighted size distribution of 0.001 wt. % alumina dispersion with added copolymer, b) photographic matrix showing dough at different compositions, c) intensity-weighted size distribution of pristine alumina suspensions at 0.001–0.01 wt. %, d) intensity-weighted size distribution of 0.001–0.01 wt. % alumina dispersion with 0.75 wt. % copolymer added

In an ideal dilute solution, the diffusion coefficient (D_t) measured using DLS remains constant regardless of solute concentration. As the concentration increases, the solution deviates from ideal behavior, prompting a first-order expansion. The diffusion interaction parameter, k_D (mL/g), represents the first-order correction to the diffusion coefficient:

$$D_t=D_0(1+k_Dc) \quad (2.5)$$

Here, k_D is determined by measuring the diffusion coefficient across a concentration range typically between 1 and 10 mg/mL, where the first-order approximation is applicable. Attractive interactions ($k_D<0$) lead to a decrease in D_t and an increase in apparent hydrodynamic diameter (h_d) in Figure 2.7.

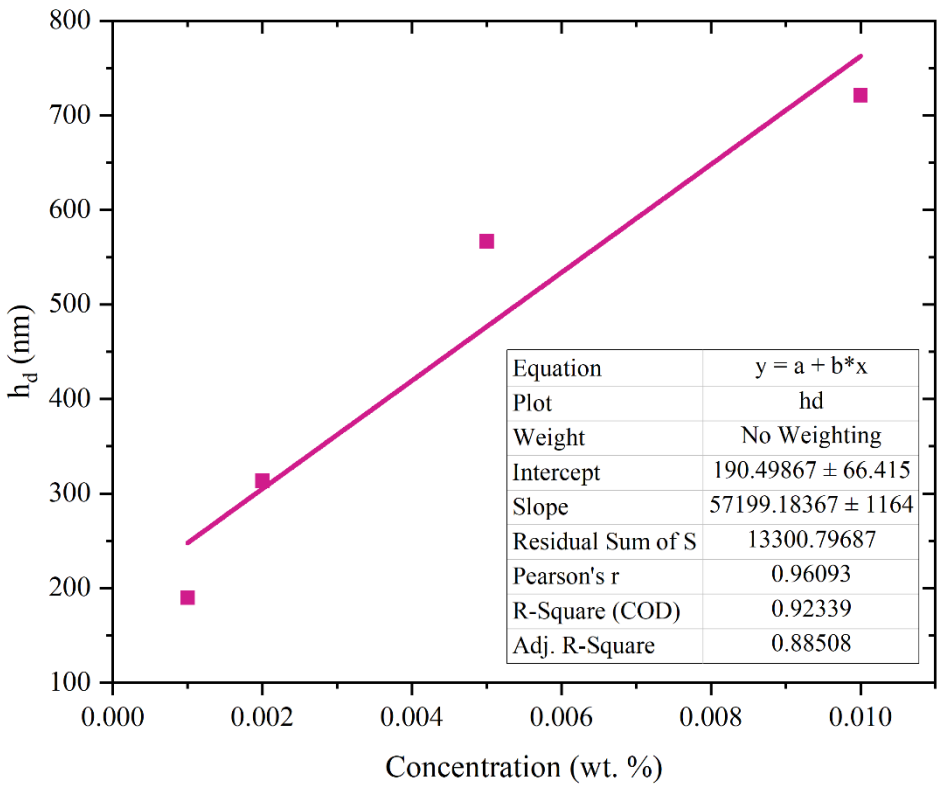

Figure 2.7 Apparent hydrodynamic diameter as a function of concentration

The dispersing effect of the copolymer was studied by tracking the change in the floc size in the medium (Figure 2.8). The increase in floc size at different particle concentrations implies that the copolymer effectively promotes particle bridging. Pristine suspensions (no copolymer) exhibited a multimodal particle size distribution with an average floc size of ~1.6 μm at particle concentrations of 1 and 30 wt. %. Conversely, introducing the copolymer resulted in a shift in the average floc size to around 20 μm even at a 1 wt. % particle loading, indicating the initiation of floc formation in the suspension. The efficacy of the copolymer in flocculating alumina particles was more prominent at higher solid contents, where flocs with an average size of ~30 μm were noticeable at 30 wt. % solid concentration, accompanied by additional peaks at larger sizes. This change in the floc size shows that copolymer can effectively facilitate particle bridging, leading to the formation of dough-like suspensions.

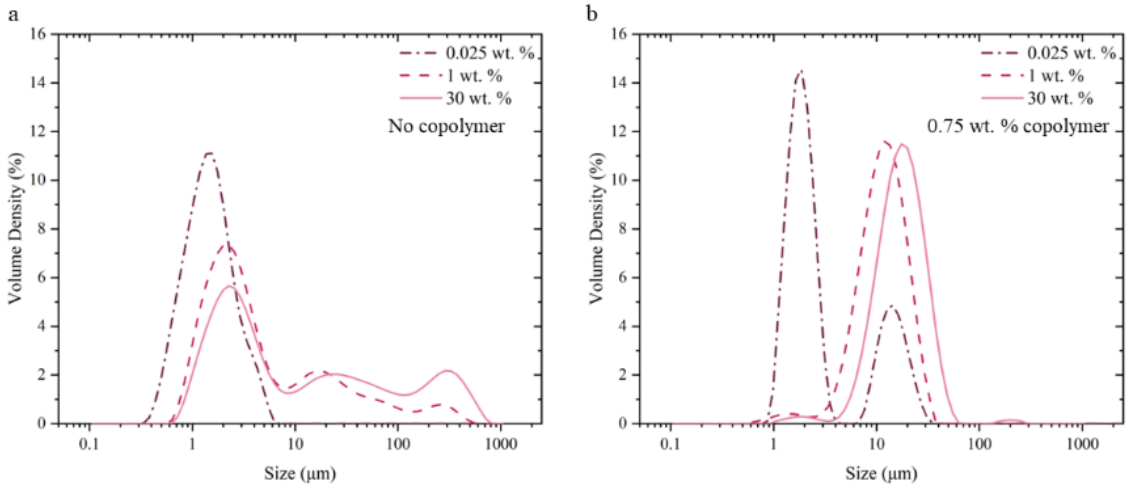

Figure 2.8 Floc size in a) pristine alumina suspensions and b) alumina suspensions in the presence of 0.75 wt. % copolymer at different particle concentrations

2.3.2. The flow behavior of alumina suspensions/doughs

For the preparation of the doughs, achieving homogeneous coagulation without any bleeding is essential. The flow behavior of ceramic suspensions with solid contents of 67.8%, 72.5%, 75.3%, and 77.1% by weight, each containing 0.75% additive by weight, was analyzed (Figure 2.9a). At shear rates ranging from 0.01 to 100 s^{-1}, all suspensions demonstrated shear-thinning behavior (Figure 2.9a). This pseudoplastic behavior of highly-loaded suspensions is due to the formation of an inter-particle network at relatively lower shear rates (Acosta et al., 2013; Dabak & Yucel, 1987; Tsai & Zammouri, 1988). As the shear rate gradually increased, this inter-particle network broke down into small, flowable clusters, leading to a reduction in the viscosity of the suspension. However, beyond 10 s^{-1}, the 77.1% wt. % suspension crumbled under the applied shear force and spread out of the measuring plate. This structural breakdown, especially at higher solid loadings, is attributed to drying during the measurement. For the 67.8% wt. % suspension, the viscosity was consistently ten times lower than that of the 75.3 wt. % suspension across the measurement range, therefore the 67.8 wt. % formulation is referred to as an ink, which flows upon the application of pressure. In contrast, the 75.3 wt. % alumina-loaded formulation exhibited a dough-like behavior across shear rates of 0.01 to 100 s^{-1}. Figure 3b displays the viscoelastic properties of 75.3 wt. % suspension with a clear yield point at 2.8×10^4 Pa.s. At low strains (<0.01 %), the structure is relatively intact, with the alumina particles forming a network stabilized by the copolymer, leading to

predominantly elastic behavior where G' is higher than G", for all suspensions (Bouhamed et al., 2009). The first crossover point corresponds to the initial yield point, where the applied strain disrupts the alumina particle network, causing the transition from the elastic region to the viscous region (G">G'). Further strain causes additional structural rearrangements, including breaking and reformation of particle-particle and particle-polymer interactions, leading to multiple crossover points (Zhu & Smay, 2011). These additional points indicate further transitions where different structural elements or interactions dominate the behavior, such as the breakdown of larger particle aggregates or the reorientation of copolymer chains (Kamani et al., 2021; Sheng et al., 2010). The initial yield point, in Table 2.3, marks the disruption of the alumina particle network under applied strain, transitioning the behavior from elastic to viscous (G" > G'). With further strain, additional structural rearrangements occur, involving the breaking and reformation of particle-particle and particle-polymer interactions, leading to multiple crossover points (Figure 2.9b). After assessing the flow behavior, 75.3 wt. % solid loading with 0.75 wt. % additive was singled out for the dough formulation.

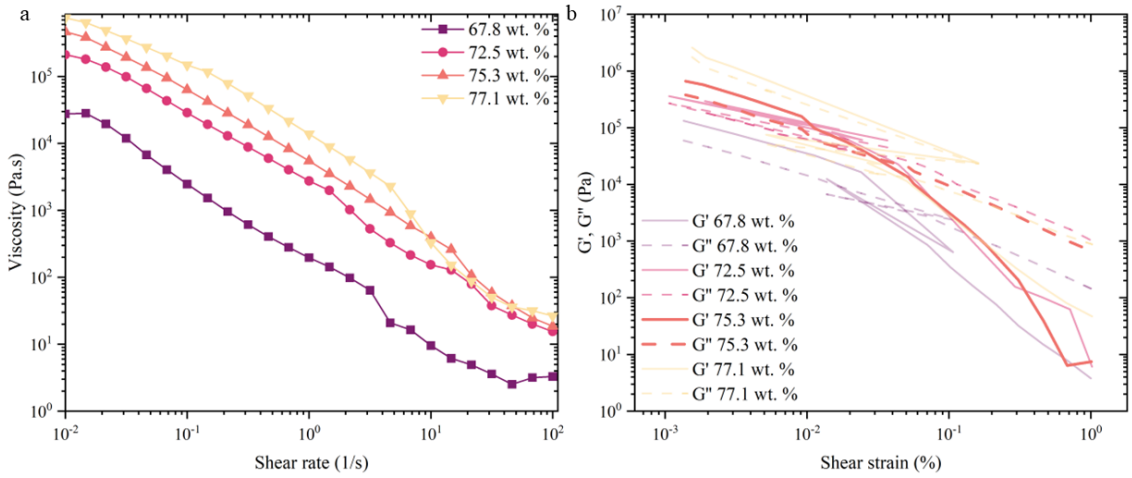

Figure 2.9 a) Viscosity as a function of shear rate and b) oscillatory rheological response of alumina suspensions with 0.75 wt. % additive at varied solid loadings (67.8–77.1 wt. %).

Table 2.3 Particle loading of alumina suspensions and their respective yield stresses and strains

Particle loading (wt. %)	Yield stress (Pa)	Strain (%)
67.8	4.8×10^{3}	0.04
72.5	6.4×10^{4}	0.02
75.3	2.8×10^{4}	0.03
77.1	2.5×10^{4}	0.1

Figure 2.10 shows molded doughs (e.g., cylinder, cube, and pentagon) that contain ~75.3

wt. % alumina and 0.75 wt. % additive. Before machining, the average density of green bodies was calculated as 2.02±0.03 g/cm^3 by dividing the weight of the samples by their volume. All hand-shaped objects demonstrated linear shrinkage of ~2.4% from molding to the dried state.

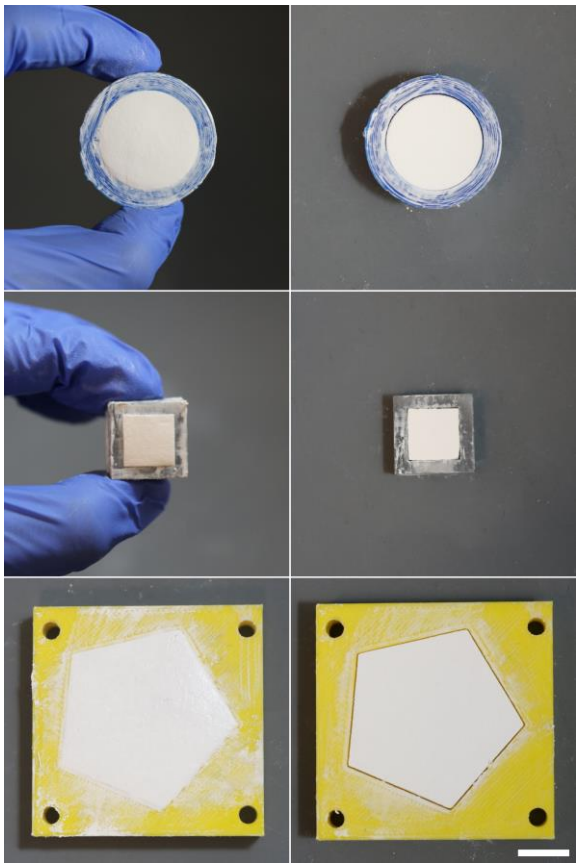

Figure 2.10 Digital images display molded doughs and their drying shrinkage, with a scale bar representing 1 cm.

2.3.3. Influence of the machining parameters on surface topography

The surface quality of the green-machined samples at varying spindle speeds in the range of 5,000 and 30,000 rpm and cutting speeds in the range of 1,000 and 1,800 mm/min were examined at green, as-sintered, and polished states. The depth of the cut was set to 0.2 mm to minimize the deformation. To evaluate machinability, the moisture content of the suspensions during 30 hours of drying in ambient conditions (20.4±1 °C, relative humidity of 52%) was tracked using a solid content analyzer (Shimadzu, uniBloc MOC63u) (Figure 2.11a). The moisture content of green bodies before machining was estimated as 1.4%.

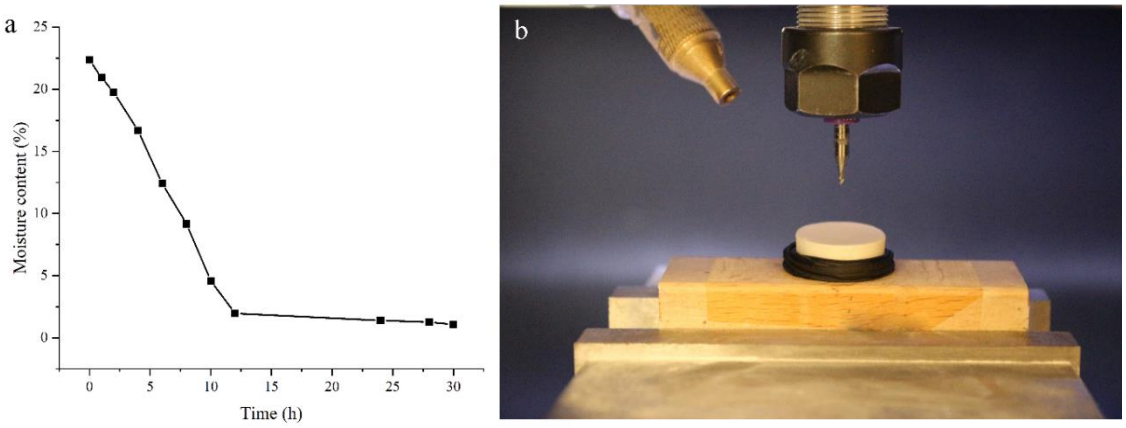

Figure 2.11 a) Moisture content of the dough with 75.3 wt. % alumina and 0.75 wt. % additive over time during ambient drying, and b) setup for mounting the sample onto the holder for CNC machining.

Figure 2.12, where the optimum machining parameter combination for the 1 mm tool is marked with a star, provides a perspective through a series of raw optical images of the green bodies, encompassing spindle speeds ranging from 5,000 to 30,000 rpm and cutting speeds spanning 1,000 to 1,800 mm/min, cut with a 1 mm tool. The optimal parameters are identified as 20,000 rpm and 1,200 mm/min, resulting in a sintered state roughness of 2 μm (Figure 2.14c). The appearance of finer notches on the machined surface was due to the tool movement, supported by the presence of hills at regular intervals on the surface profilometry in Figure 2.14a for both green and sintered samples. At lower spindle speeds (5,000–10,000 rpm), the interaction of the cutting tool with alumina was relatively inefficient compared to the higher spindle speeds. As the spindle speed increases up to 20,000 rpm, the tool begins to engage with the material more effectively, leading to a decrease in roughness (Figure 2.14c). The surface profile at 20,000 rpm demonstrated a more regular and consistent pattern, featuring reduced spikes and minimized differences between the height of hills and valleys on the surface. First, higher spindle speeds accelerated the movement of the tool through the material, forming thinner chips, and in turn, providing a smoother surface. Beyond 20,000 rpm, the increase in spindle speed disrupted the machining process, and increased spindle speeds resulted in tool wear and vibrations. Consequently, the machining quality deteriorated, leading to an increase in surface roughness (Figure 2.14c). The edges of the cutting tool worsened more swiftly, generating irregularities on the machined surface. The vibrations due to increased spindle and cutting speed led to poor surface roughness (Ra=8.3 μm) at 30,000 rpm. The samples machined with a 1 mm tool at a spindle speed of 20,000 rpm and a cutting speed of 1,200

mm/min exhibited more consistent patterns and minimal disparity between the heights of hills and valleys.

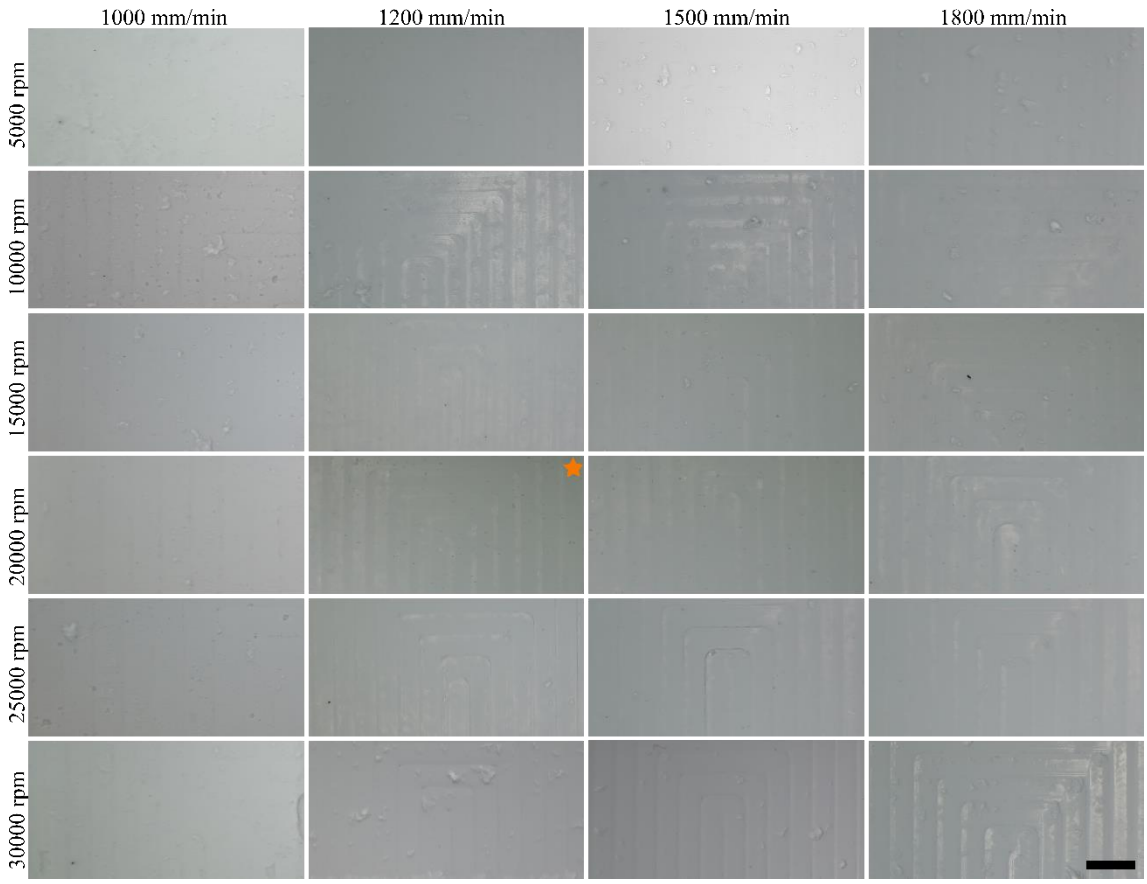

Figure 2.12 Optical images of machined green bodies (1 mm tool) before sintering, with the optimal machining parameters for the 1 mm tool (20,000 rpm, 1,200 mm/min) indicated by a star. Scale bar represents 2 mm.

Figure 2.13, where the optimum machining parameter is marked with a star, displays a full outlook of raw optical images of surfaces machined using a 2 mm tool, including spindle speeds ranging from 10,000 to 30,000 rpm and cutting speeds spanning from 1,000 to 1,800 mm/min. The surface profiles achieved by using optimum machining parameters for 1 mm and 2 mm tools are provided in Figure 2.14a and b. The surface roughness obtained using the 2 mm tool was confined to a narrow array of 1–5 µm (Figure 2.14d), while the 1 mm tool resulted in a surface roughness with more variation, ranging from 2 to 8.5 µm (Figure 2.14c). Optimum machining parameters were selected as a spindle speed of 20,000 rpm and cutting speed of 1,200 mm/min for a 1 mm tool (Figure 2.14a, c) with 2.24 µm and 0.30 µm average surface roughness at as-sintered and polished

state, respectively. The optimum machining parameters for the 2 mm tool are a spindle speed of 15,000 rpm and a cutting speed of 1,800 mm/min (Figure 2.14b, d) with 1.31 μm and 0.27 μm average surface roughness at as-sintered and polished state, respectively. The surface roughness was found to decrease with increasing tool diameter in alignment with the previous reports (Demir et al., 2021; Hafidh Obaeed, 2019). This behavior has been attributed to applying cutting force over a larger area with increasing tool diameter. However, after post-sintering polishing, the disparity in the surface quality between different tool diameters was negligible. Consequently, the 2 mm tool for its ability was selected to facilitate faster machining operations with a material removal rate of 14.81 mg/s in comparison to 7.81 mg/s of the 1 mm tool using a spindle speed of 15,000 rpm and a cutting speed of 1,800 mm/min.

The surface roughness (perpendicular direction to the machining), affected by sintering-induced grain growth, exhibited an increase to 1.86±0.89 μm when utilizing a 2 mm tool at varied spindle and cutting speeds (10,000–30,000 rpm, 1,000–1,800 mm/min). In contrast, the unsintered green bodies displayed a comparatively lower surface roughness of 0.89±0.22 μm. The effect of sintering on the surface profile was provided in Figure 2.15 for a machined surface at a spindle speed of 20,000 rpm and a cutting speed of 1,200 mm/min with a 1 mm and 2 mm diameter cutting tool. The lowest surface roughness was achieved at a spindle and cutting speed of 20,000 rpm and 1,200 mm/min for a 1 mm tool and 15,000 rpm, and 1,800 mm/min for a 2 mm tool.

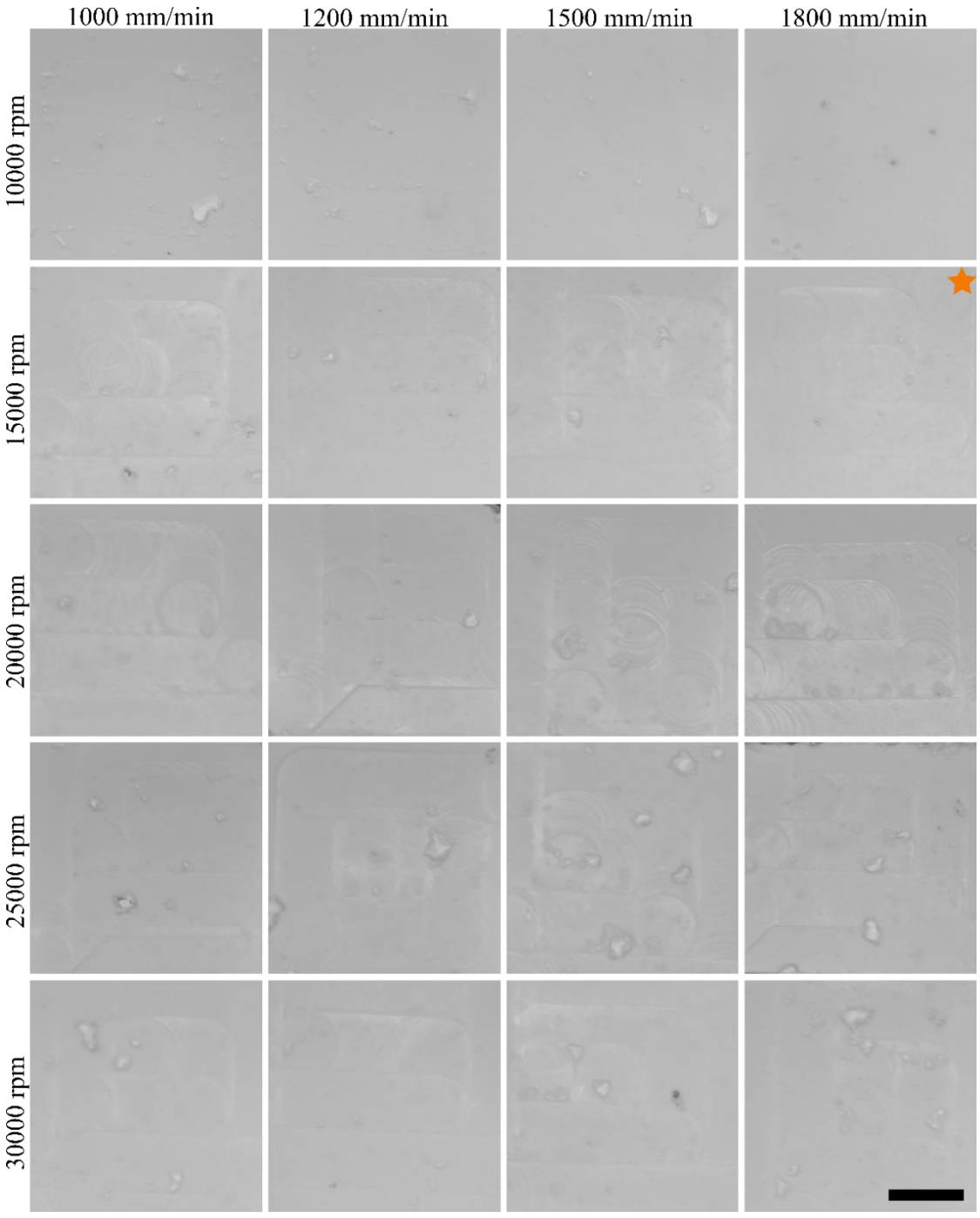

Figure 2.13 Optical images of machined green bodies (2 mm tool) before sintering, with the optimal machining parameters for the 2 mm tool (15,000 rpm, 1,800 mm/min)

indicated by a star. Scale bar represents 2 mm.

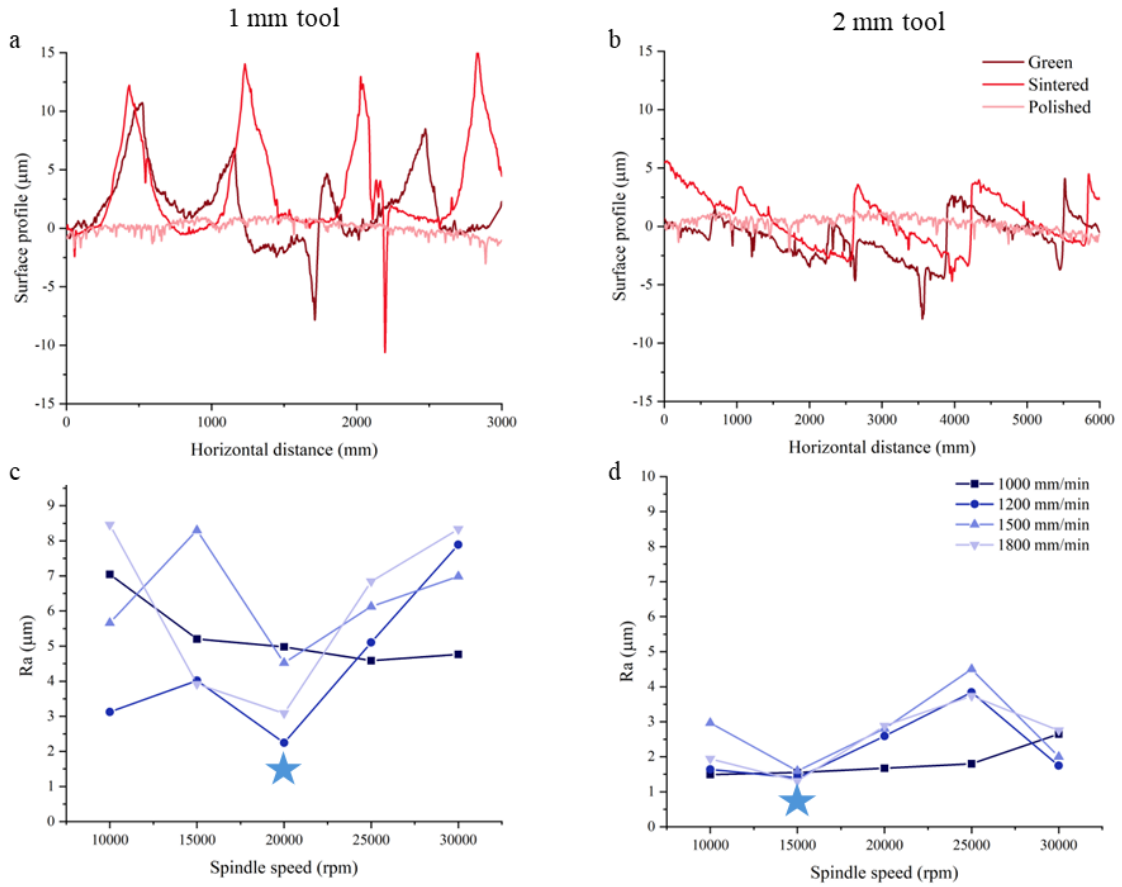

Figure 2.14 Surface profiles of green bodies machined with: a) 1 mm tool (20,000 rpm, 1,200 mm/min), b) 2 mm tool (15,000 rpm, 1,800 mm/min) using optimized parameters, and c) average arithmetic surface roughness values cut at the green state with spindle speeds of 10,000–30,000 rpm and cutting speeds of 1,000–1,800 mm/min using 1 mm and d) 2 mm tools analyzed at the sintered state. The lowest surface roughness, associated with optimized machining parameters, is marked with a star.

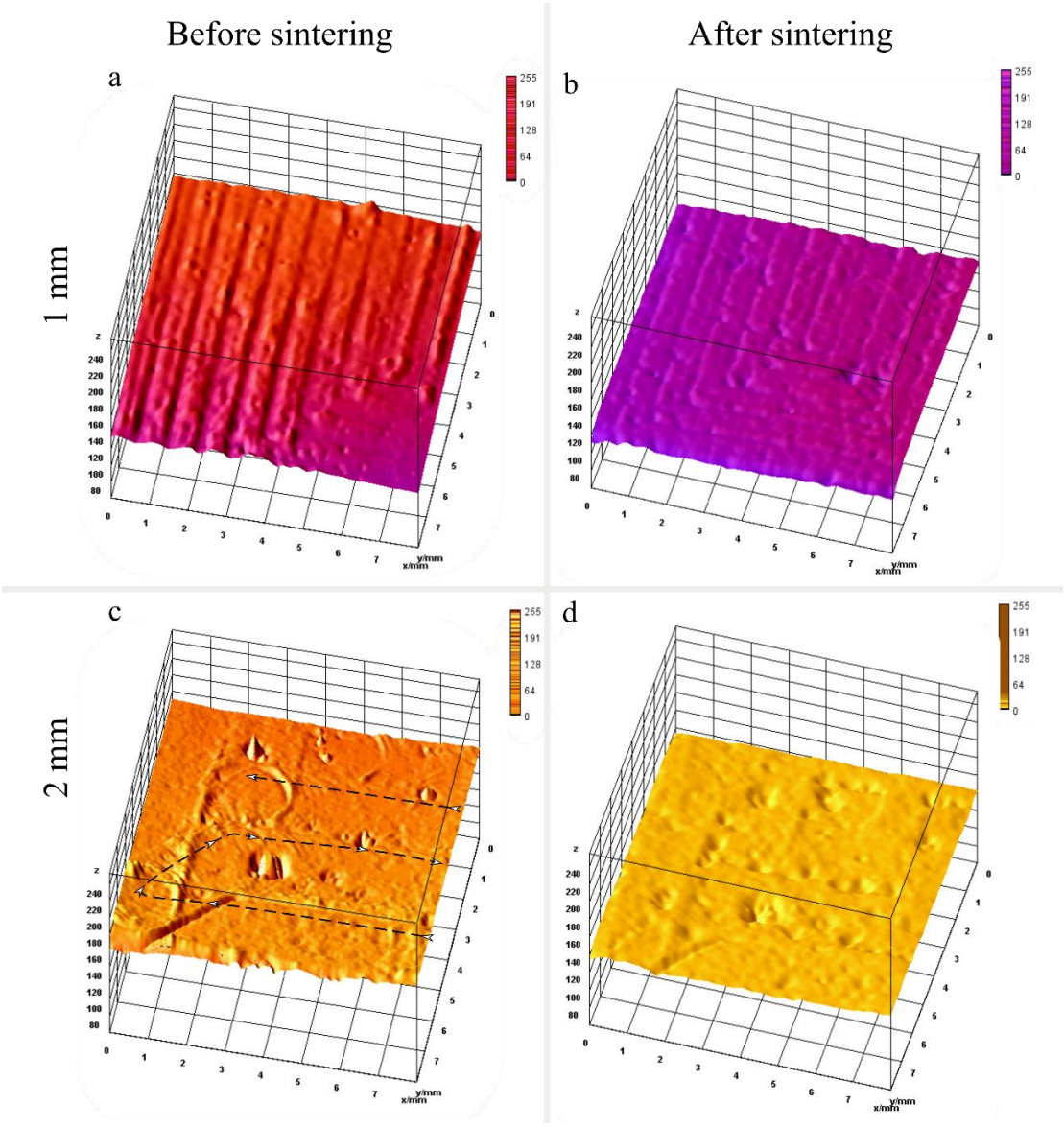

Figure 2.15 Effect of tool diameter on surface roughness, represented by a 3D surface plot of optical images, samples were green-machined with a 1 mm diameter tool a) at the green state, b) after sintering; a 2 mm diameter tool c) at the green state and d) after sintering (machining parameters: spindle speed of 20,000 rpm, cutting speed of 1,200 mm/min)

The hills stand for elevated regions on the machined surface where the material was not effectively removed during the CNC operation, leading to a higher surface profile, and valleys represent the size of the tool's cutting edge as it engages with the sample. In Figure 2.16a–b, the valleys between the hills were estimated as 653.2±24.3 and 1366.6±7.8 μm long (n=10 measurements) for the regions machined using 1 mm and 2 mm tools, respectively.

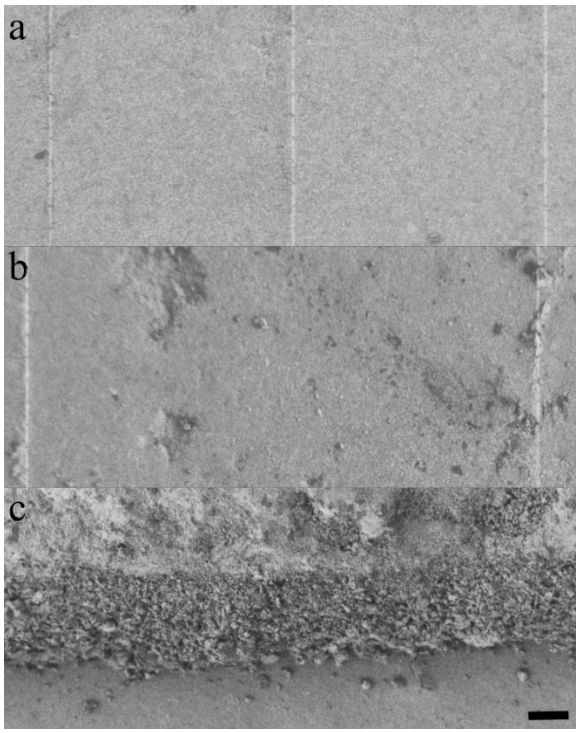

Figure 2.16 SEM images showing sintered bodies: a) machined with a 1 mm tool, b) machined with a 2 mm tool, and c) edge formation during machining with a 2 mm tool. Dotted lines in (a) and (b) indicate hills formed during machining. Scale bars represent 100 µm, magnification 100x.

2.3.4. Showcasing a simple route for a recycling solution

Processing of ceramics generates a significant carbon footprint; for many ceramics, this footprint arises from the mining and extraction steps (Furberg et al., 2019; Gediga et al., 2019; Ibáñez-Forés et al., 2011), for alumina, it is acquiring the bauxite ore (Y. Ma et al., 2022). Therefore, the recycling of advanced ceramics is critical to minimize the use of resources in alignment with the principles of the EU Green Deal (European Commission Directorate-General For Communication, 2019).

To prepare green bodies with recycled content, recycled alumina was sourced from intentionally broken parts at the green state, where only pristine unused alumina samples were crushed in a mortar. These crushed particles were then added to constitute 10, 20, and 30 wt. % of the total alumina powder composition, labeled as 10 wt. % R, 20 wt. % R, and 30 wt. % R, respectively. Following the same procedure, the copolymer was added in equal proportion to the total weight of alumina, including both pristine and recycled portions. Instead of employing additional processes such as ball milling with solvents or

binder removal at elevated temperatures, the additive content was increased to simplify the process, reduce energy consumption, and minimize potential environmental impact. By avoiding complex and resource-intensive steps, a more efficient and sustainable method was developed for incorporating recycled alumina into the dough formulation.

Electrokinetic characterization was also performed, upon preparing a 0.001 wt. % alumina suspension from 100 % recycled alumina at the green state, the zeta potential was found as -41.6 mV, sustaining the stability of the polymer bridging.

Figure 2.17 visually conveys the varied portions (0–30 wt. %) of recycled alumina, prompting a thorough investigation into the structural changes with increasing recycled content. The doughs exhibited a stickier nature with increasing recycled content due to the increase in the total polymer content from 0.75 wt. % to 0.975 wt. %.

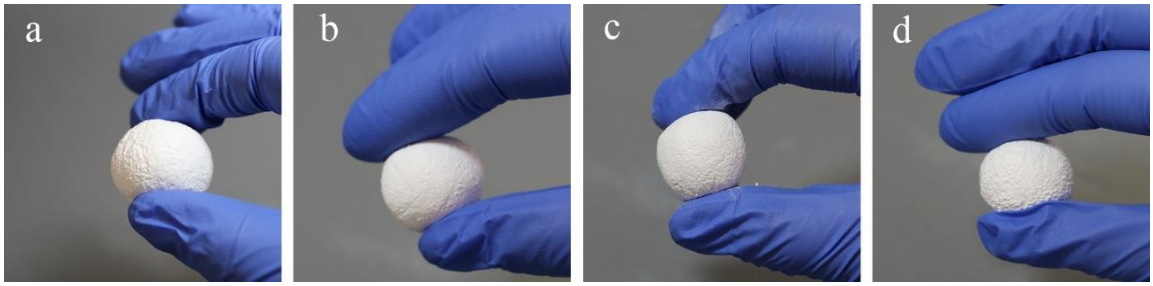

Figure 2.17 Alumina doughs containing a) 0 wt. % (pristine), b) 10 wt. %, c) 20 wt. %, and d) 30 wt. % recycled content

As the recycled content increases, the Z-average particle size and PDI also increase (Table 2.4). Pristine alumina (0 wt. % recycled content) has the smallest particle size (282 nm) and the lowest PDI (0.342), signifying a more uniform particle size distribution. As recycled content is introduced, both the average particle size and PDI increase, reaching a peak Z-average of 931 nm and a PDI of 0.766 at 30 wt. % recycled content. The 100 wt. % recycled sample shows a reduction in Z-average to 554 nm and a PDI of 0.553, indicating some variation in particle size and distribution when fully recycled material is used.

Table 2.4 Z-average and PDI values of 0.001 wt. % alumina suspensions that contain 0, 10, 20, 30, and 100 wt. % recycled alumina

Recycled content	Z-average (nm)	PDI
Pristine (0 wt. %)	282	0.342

10 wt. %	458	0.418
20 wt. %	476	0.546
30 wt. %	931	0.766
100 wt. %	554	0.553

In Figure 2.18, SEM micrograph of the pristine sample (0 wt. % recycled) shows a relatively uniform microstructure with well-defined, interconnected alumina particles, minimal porosity, and smooth surfaces. As the recycled alumina content increases to 10 wt. %, the microstructure starts to show irregularities, increased porosity, and minor agglomeration, indicating the initial impact of incorporating recycled material. At 20 wt. % recycled alumina, the irregularities become more pronounced with significantly lower porosity and larger agglomerates, resulting in a more heterogeneous structure. The 30 wt. % recycled alumina sample displays a highly irregular microstructure with substantial porosity and particle agglomeration, along with a much rougher and less uniform surface featuring noticeable defects and discontinuities.

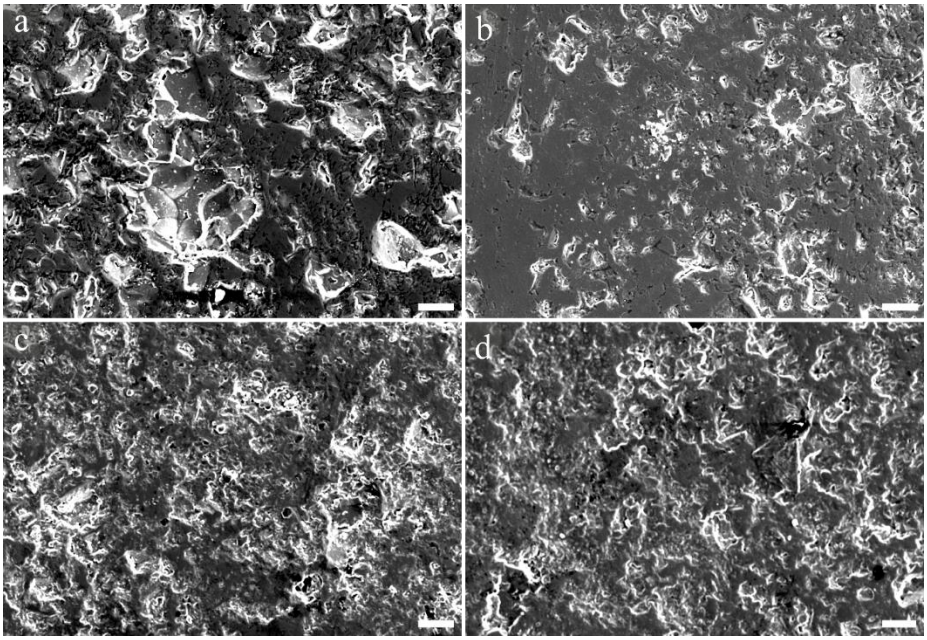

Figure 2.18 SEM micrographs of samples that contain a) 0 wt. % (pristine), b) 10 wt. %, c) 20 wt. %, and d) 30 wt. % recycled alumina at 1,000x magnification (Scale bars

represent 10 μm.)

Machining of alumina green bodies that incorporate recycled alumina was performed by employing the same parameters that were optimized on pristine alumina samples (spindle speed of 20,000 rpm and cutting speed of 1,200 mm/min for 1 mm tool, spindle speed of 15,000 rpm, and cutting speed of 1,800 mm/min for 2 mm tool). As the recycled content increases, more frequent bumps and thus uneven material removal was observed on the CNC-machined surfaces due to the expected variations in particle size and shape between the recycled and pristine ceramics. Agglomeration of the recycled ceramic particles, either due to incomplete mixing or the tendency of particles to cluster, led to localized areas of increased material density.

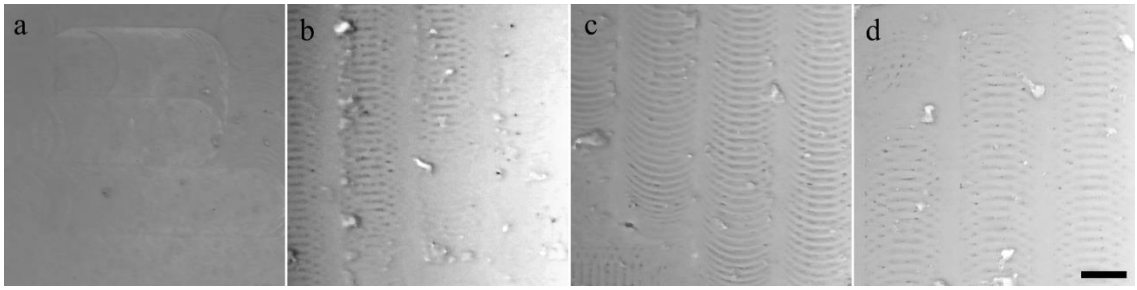

Figure 2.19 Effect of recycled content on surface roughness: a) 0 wt. % recycled (pristine), b) 10 wt. % recycled, c) 20 wt. % recycled, and d) 30 wt. % recycled alumina-containing green bodies machined with a 2 mm tool at a spindle speed of 15,000 rpm and cutting speed of 1,800 mm/min. Lightness-contrast adjusted for better visualization using Inkscape, scale bar represents 1 mm.

The 3D surface plots of optical images of the green bodies that have a recycled portion and are cut using a 1 mm tool are shown in Figure 2.20.

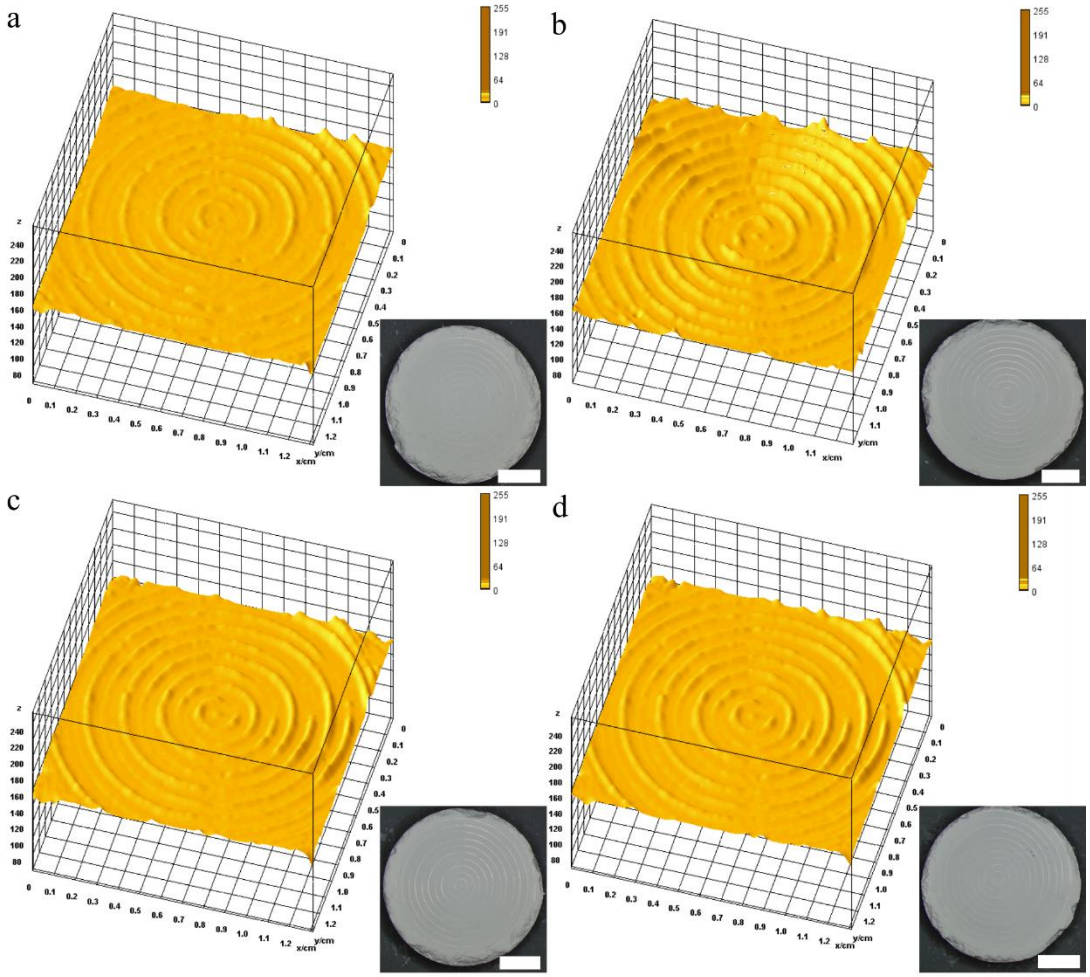

Figure 2.20 Comparison of surface characteristics for a) 0 wt. % recycled (pristine), b) 10 wt. % recycled, c) 20 wt. % recycled, and d) 30 wt. % recycled alumina-containing green bodies machined with a 1 mm tool at a spindle speed of 20,000 rpm and cutting speed of 1,200 mm/min. The data is depicted through a 3D surface plot of optical images, with the optical images of the green bodies presented in the lower right corner. The scale bar represents 5 mm.

The implementation of these optimized machining parameters revealed no significant differences in surface quality, an observation supported by comparable hardness values in the sintered state after polishing. This outcome highlights the effectiveness and consistency of the optimized machining parameters, demonstrating their applicability across both conventional and recycled alumina materials.

2.3.5. Microstructural and mechanical characterization

Figure 2.21a illustrates the variation in the density of green and sintered alumina samples with varying recycled content. A slight fluctuation in the density of the green samples is observed, initially increasing up to 10 wt. % recycled content, followed by a decrease beyond this point. This trend suggests that the initial inclusion of recycled material may enhance packing density up to a certain threshold, beyond which the particle size distribution and potential agglomeration may reduce packing efficiency. Furthermore, the increase in polymer content with rising recycled content could influence packing behavior and densification, potentially introducing more porosity in the green state. Figure 2.21b presents the stress-deformation behavior of green and sintered samples. The green samples demonstrate minimal resistance to deformation due to their low strength, while their coagulated nature allows them to maintain integrity during machining.

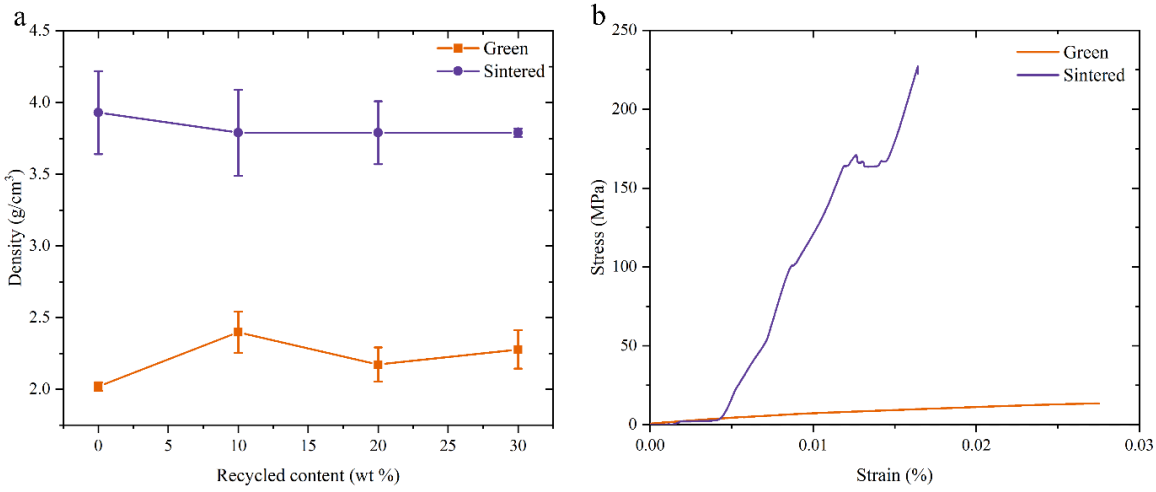

Figure 2.21 Comparison of a) density at both green and sintered states with varying recycled content and b) stress-strain curve of alumina at green and sintered state

Figure 2.22a illustrates the variation in hardness and flexural strength with recycled content. The pristine alumina displayed a hardness of 15.16±1.15 GPa, while the hardness of the 10 wt. %, 20 wt. %, and 30 wt. % recycled alumina remained comparable to that of the pristine alumina. These findings suggest that the inclusion of recycled alumina, up to 30 wt. %, does not significantly affect the hardness of the sintered alumina bodies, indicating robust mechanical performance even with increased recycled content. However, flexural strength showed a declining trend with rising recycled content. This decrease may be attributed to the incorporation of larger recycled particles, which could introduce stress concentration sites and potential defects, thereby reducing flexural strength. The additional polymer content also contributed to this trend by creating voids

or weak points within the structure (Figure 2.18). Overall, hardness is a surface property and is less influenced by internal flaws and porosity, whereas flexural strength is more affected by bulk defects and the overall integrity of the material. As the recycled content increases, deformation at a given stress level increase, indicating reduced stiffness. The stress-strain curves exhibited a decrease in peak stress with higher recycled content, reinforcing the observation that increased recycled content and polymer amount may compromise the structural integrity of the alumina samples.

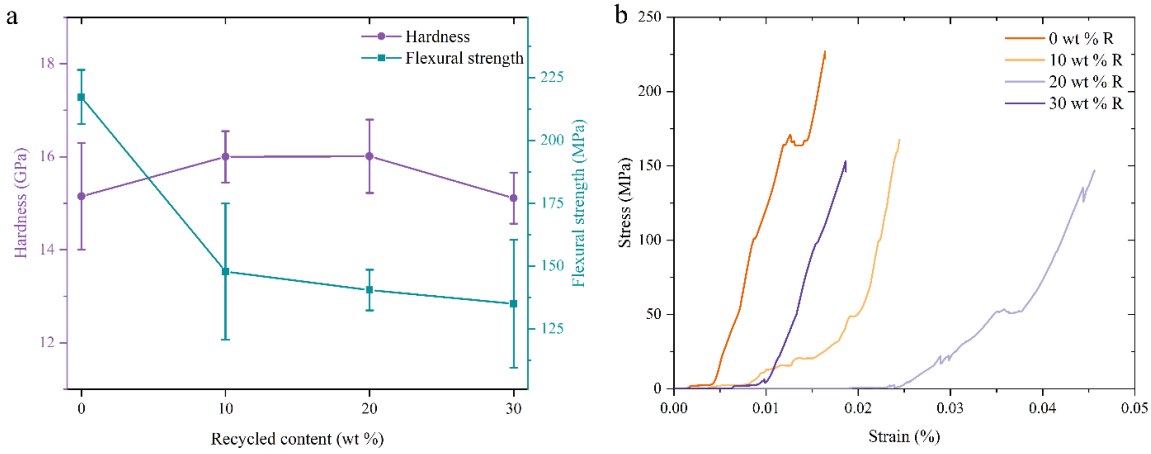

Figure 2.22 a) Hardness and flexural strength and b) stress-strain curve of alumina with varying recycled content (0–30 wt. % R, R stands for recycled portion.)

The average K_{xy}, K_{xz}, and K_{yz} were calculated as -2.0, -1.8, and 2.2 using Eq. (2.1)-(2.3), respectively. A large absolute value of the K-factor implies higher shrinkage anisotropy and K values ≥ 12 were associated with anisotropic shrinkage; thus, a K value of ~2 in this system was referred to as isotropic (Heunisch et al., 2010). All hand-shaped objects without any recycled portion demonstrated linear isotropic shrinkage of ~19% from the dried state to the sintered state and reached a density of 3.93±0.29 g/cm^3 (~99.5% t.d., t.d.=3.95 g/cm^3) with no coarse imperfections or cracks (Figure 2.23). The larger the anisotropy in particle shape, the larger the shrinkage anisotropy of the sintered bodies (Heunisch et al., 2010). The powder composed of isotropic particles (Table 2.4) results in the highest shrinkage upon sintering (Table 2.5). This is due to the minimal resistance these particles offer against rearrangement under the influence of capillary forces during drying (C. Wang et al., 2024). Pristine samples without any recycled content are comparatively denser, whereas the anisometric particles in samples with recycled content obstruct each other, leading to less dense structures.

Table 2.5 Shrinkage and K-factor of sintered alumina bodies at different recycling amounts

Sample	Shrinkage (%)	K_{xy}	K_{xz}	K_{yz}
0 wt. % recycled (pristine)	19.05±0.56	-2.0	-1.8	2.2
10 wt. % recycled	17.86±0.56	2.9	0.9	-2.1
20 wt. % recycled	17.53±1.16	-0.6	3.3	3.8
30 wt. % recycled	17.72±0.77	5.2	-3.3	-9.0

The average size of the sintered alumina particles in Figure 2.23d was approximated as 7.8 μm^2 by using the "Analyze particles" plugin of ImageJ software, showing that grain growth was achieved upon sintering (German, 2016; He & Ma, 2,000; Schneider et al., 2012).

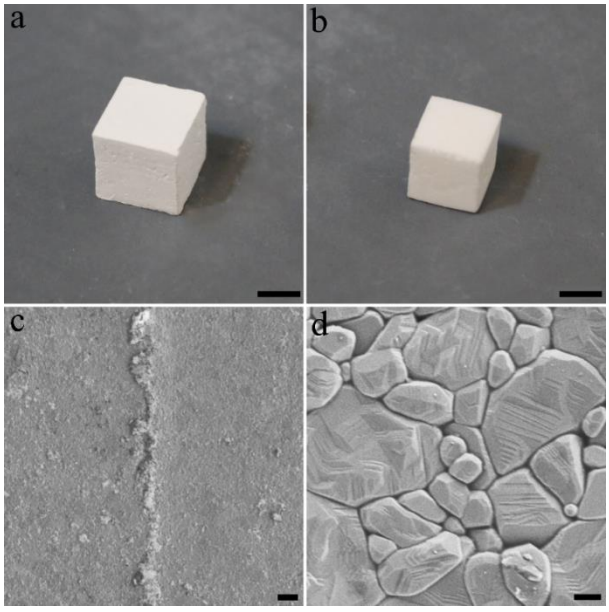

Figure 2.23 Digital images of a 1 cm^3 alumina (scale bars represent 5 mm) at a) green state, b) sintered state, and SEM of c) the green-machined surface at the sintered state at 500x magnification, the line in the middle of the image shows the hill occurred during machining in between tool paths (scale bar represents 10 μm), d) the green-machined surface at the sintered state at 10,000x magnification (scale bar represents 1 μm)

2.3.6. Fabrication of alumina crucibles

Starting from self-standing doughs of alumina, custom-sized crucibles (Figure 2.24) and curvy-shaped objects Figure 2.25 were fabricated. Crucibles with a diameter and a wall thickness in the range of 10–25 mm and 1–5 mm were fabricated, respectively. In alignment with the goal of affordable and accessible prototyping and low-number fabrication, the standardized parameters that are presented here have the potential to impart ceramics processing capabilities to laboratories with limited materials engineering domain knowledge.

Figure 2.24 House-made alumina crucibles with varying dimensions, scale bar represents 1 cm.

Figure 2.25 A complex, curvy-shaped alumina body having a 2 mm wall thickness

2.4.Conclusion

Near-net shaping of advanced ceramics often requires intricate, customized solutions, and the industry currently lacks a straightforward method to streamline low-volume

production using existing setups without investing in expensive pressing techniques and molds. This work began with a simple formulation to create self-standing alumina doughs and demonstrated the parametrization of CNC machining in the green state of alumina. To support the transition of the ceramic industry to greener methods in line with the principles of the EU Green Deal, a recycling method at room temperature without any specialized equipment was presented, showcasing the potential for material regeneration within this system. Overall, the development of standardized, simple, energy- and cost-effective processes with a low barrier to entry for the near-net shaping of ceramics is essential to accelerate innovation, promote widespread adoption, and facilitate advancements in various industries reliant on ceramic materials. This work, which outlines a robust method enabling custom-based and low-volume production, aims to strengthen the ceramics industry, particularly in preparation for potential future supply-chain crises.

Chapter 3

3. EXPANDING FROM SINGLE TO MULTI-COMPONENT SYSTEMS: GREEN MACHINING OF SELF-STANDING SIALON DOUGHS FOR COMPLEX SHAPES IN LOW-VOLUME PRODUCTION

This chapter is based on the article "Self-standing doughs of SiAlONs enable low-volume production through green machining." that was submitted to RSC Nanoscale in June 2024. The methodology used for coagulating alumina in Chapter 2 was expanded to nitrides in a multi-component ceramic system, specifically a SiAlON with a ceramic composition optimized by MDA Ceramics Inc.

3.1.Introduction

Silicon nitride (Si_3N_4) is used in demanding applications such as engine components, bearings, cutting tools, wear parts, and crucibles due to its abrasion resistance, thermal stability, and mechanical strength (Boberski et al., 1989; El-Amir et al., 2021; Jack, 1976; Krstic & Krstic, 2012; Richerson & Stephan, 1991; Rosenflanz, 1999). To enhance the mechanical and thermal properties of silicon nitride, aluminum, oxygen, and other metal oxides are added to its formulation (Boberski et al., 1989; Calis Acikbas & Demir, 2013; Lange, 1980; Zhou et al., 2015). This type of formulation, which is referred to as SiAlONs, offers higher densification and enables better thermal shock and wear resistance (Herrmann et al., 2012; Jack, 1986; Kumar et al., 2009; Z. B. Yu & Thompson, 2006).

SiAlONs are often used to fabricate pins, nozzles, extrusion dies, and weld rolls in custom sizes and low volumes, driven by the distinct demands of various industries (Bhargava &

Sharma, 2011; Cother, 1987; Ferguson & Rae, 1985; Hussey & Wilson, 2012). Although SiAlON ceramics have the potential to be used as cutting tools, they have not been widely used commercially for many years. The main reason for this is the large-scale production difficulties due to the tendency of non-oxide materials such as Si_3N_4 and AlN to react with water in aqueous environments (Krnel & Kosmač, 2001). Moreover, the standard processes that are designed to cater to high-volume production such as uniaxial and cold isostatic pressing, and slip casting can only deliver standard shapes and cannot deal with specific geometries such as holes, threads, and grooves. To reach the final form, SiAlON bodies are near-net shaped at the green or sintered state through machining. Machining at the sintered state suffers from material losses due to the brittle nature of the ceramics as well as tool wear (An et al., 2021; Ayode Otitoju et al., 2020; Bharathi et al., 2021; Bilal et al., 2018; Amir Mahyar Khorasani et al., 2016; H. Ma et al., 2024). On the other hand, green machining provides a lower energy route owing to the softness of the powder compact at the green state (Janssen et al., 2008; Kulkarni & Dabhade, 2019; Liu et al., 2018; Nieto et al., 2014). Current methods to consolidate green bodies rely on the pressing of the powder into a standard shape, and involve a binder, usually in considerable amounts (3–40 vol. %) (Ceylan et al., 2011; Leo et al., 2014; Meshalkin & Belyakov, 2020; Wu et al., 2020), to impart enough strength to the powder compact for enduring machining forces. In Chapter 2, the preparation of self-standing, malleable green bodies of alumina was demonstrated. Here, the materials portfolio was expanded to a nitride-based advanced ceramic in a multi-component system, SiAlON doughs were molded, and complex-shaped products were produced via machining (Figure 3.1).

A specific SiAlON composition that was previously optimized was employed to achieve full densification, where i) $CaCO_3$ is employed in the Y-Sm-Ca multi-cation system to obtain α-SiAlON, ii) Y_2O_3 is added as a sintering aid, and iii) Sm_2O_3 is incorporated to promote elongated β-SiAlON grains, thereby improving the fracture toughness of Si_3N_4 (Calis Acikbas et al., 2012; Mandal et al., 2006). As the additive, a PEG-grafted copolymer of 2-acrylamido-2-methylpropane sulfonic acid (AMPS) and AA was used to coagulate the particles via polymer bridging.

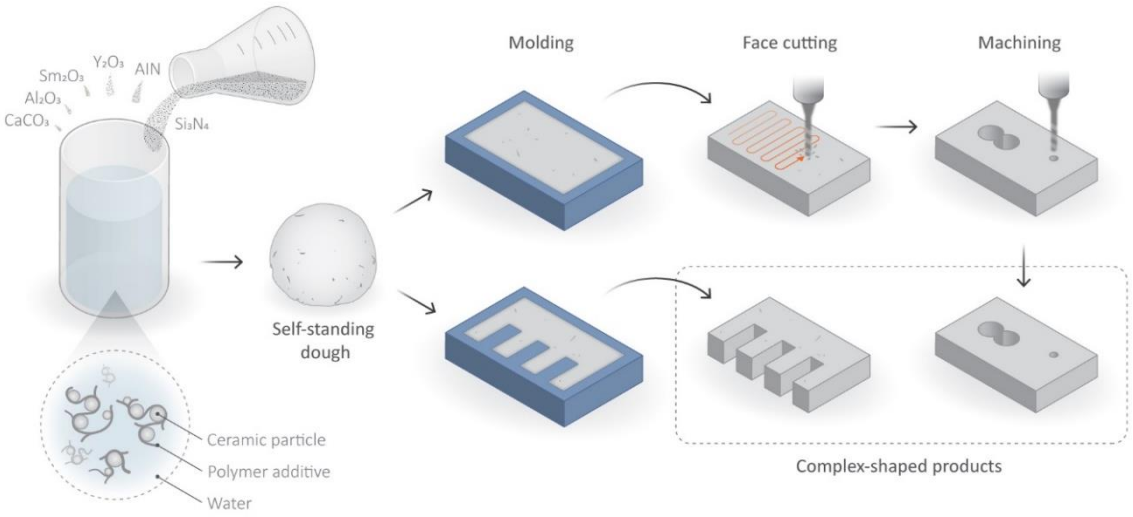

Figure 3.1 Process diagram to formulate complex-shaped SiAlON green bodies

Through electrokinetic and rheological characterization, the minimum copolymer amount was identified as 2 wt. % additive with respect to the solid loading (Figure 3.2), and homogeneously coagulated ~72.7 wt. % aqueous SiAlON suspensions. Following gas pressure sintering (GPS), hand-shaped objects exhibited an isotropic linear shrinkage of ~19% from the dried state, achieving a sintered density of ~3.24 g/cm^3 (~99.99% theoretical density). The sintered microstructure was assessed on polished surfaces using SEM and the Vickers indentation hardness of the sintered sample was compared with a wear part that was produced through pressing.

Figure 3.2 The steps involved in preparing a self-standing dough consisting of 72.7 wt. % SiAlON and 2 wt. % copolymer.

This shift from the current industrial standard (e.g., compacted powder/binder mix) to malleable doughs could be the key for building resilient low-number manufacturing and prototyping schemes for advanced ceramics. These doughs do not require expensive molds or setups yet can easily comply with traditional machining. The SiAlON dough has a much lower flexural modulus of ~0.5 MPa compared to the other reported powder/binder mixes of SiAlONs (20–90 MPa) (Ganesh & Sundararajan, 2010; J. Yu et al., 2009; Zhang et al., 2003). Therefore, it necessitates lower forces for shaping yet its

integrity does not get compromised due to its coagulated nature. In this study, the formation of a SiAlON-based dough was demonstrated; this expansion in the materials portfolio is promising for developing energy-, cost-, and resource-efficient routes for the processing of advanced ceramics.

3.2.Experimental

3.2.1. Materials

The raw materials used included high purity α-Si_3N_4 powder with 1.3 wt. % oxygen (P95H, Vesta Corp.), Y_2O_3 (≥99.9%, Reetec), AlN powder with 1.6 wt. % oxygen (H Grade, Tokuyama Corp.), α-Al_2O_3 powder with 1.4 wt. % oxygen (P172LSB Grade, Alteo), $CaCO_3$ (≥99.75%, Reidel-de Haën), and Sm_2O_3 (≥99.9%, Stanford Materials Corp.). Additionally, AMPS (99%), AA (99%), and KPS (≥99.0%) were sourced from Sigma-Aldrich, while PEG (Mw = 1,000 g/mol), HCl (37%), NaOH (97%), and MA (99%) were obtained from Merck. All chemicals were used without further purification, and solutions were prepared with DI water having a resistivity of 18.2 MΩ·cm, with the pH adjusted to 7.

3.2.2. Synthesis of the additive

In a standard aqueous free radical polymerization of AA/AMPS/MAPEG with a molar ratio of 1:1:0.3, 0.05 mol of AA, 0.05 mol of AMPS, and 0.015 mol of MAPEG (Mw ≈ 550 g/mol) were dissolved in 110 mL of distilled water (Salami & Plank, 2012). The pH of the mixture was adjusted to ~8 using aqueous NaOH solutions. This mixture was then transferred to a 250 mL three-neck flask connected to a reflux condenser. Under nitrogen purge and magnetic stirring, the temperature was raised to 50 °C. Subsequently, 10 mL of KPS solution (initiator, 1 mol % of the total mole of the monomers) was added dropwise to the reaction chamber over 50 minutes. Afterward, the temperature increased to 60 °C, and a second 10 mL initiator solution was added. The temperature of the reaction was further raised to 80 °C, and the reaction continued for 4 h. The reaction was cooled down to room temperature, then the copolymer was precipitated in ethanol and dried at 60 °C for 24 h for further characterization.

The composition of the copolymer (Figure 3.3, Table 3.1, and Table 3.2) was determined using NMR (Varian Unity Inova 500 MHz, Agilent Technologies, USA).

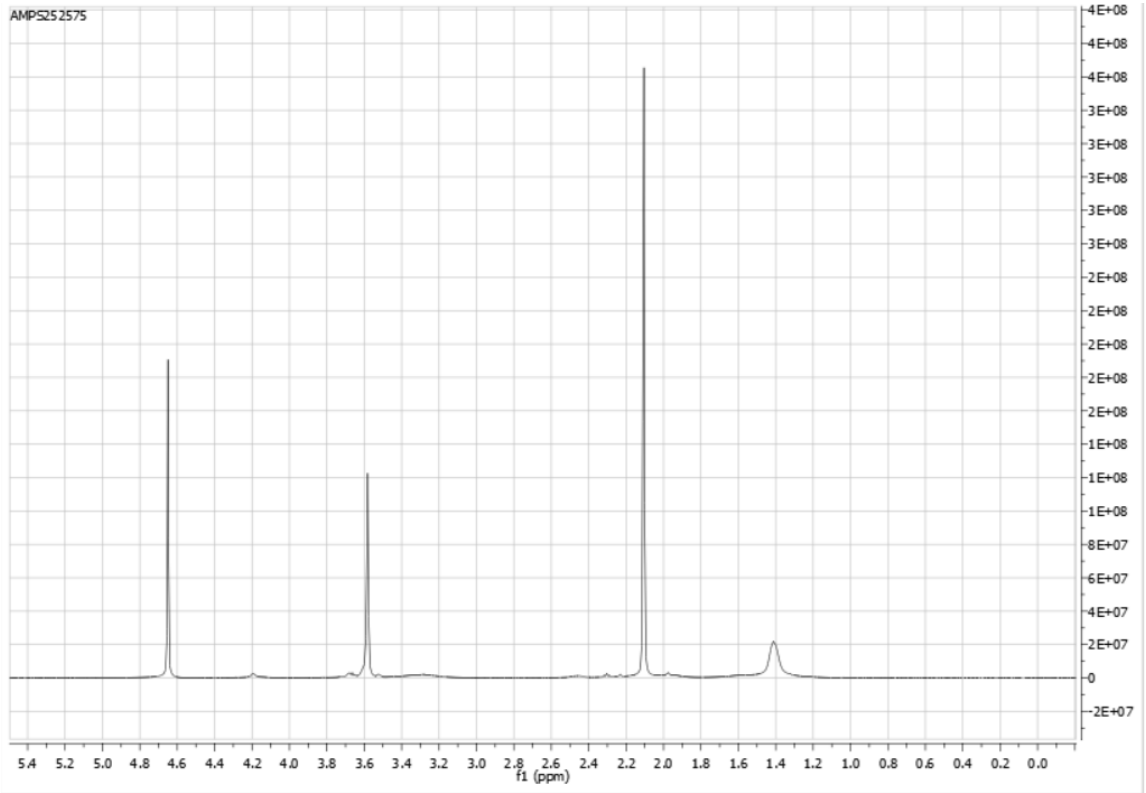

Figure 3.3 ^{1}H NMR spectrum of the AMPS/AA/PEG copolymer in deuterium oxide (D_2O) (The peak at ~4.65 ppm originates from D_2O solvent in the measurement.)

Table 3.1 ^{1}H NMR absolute integral values associated with each functional group of the copolymer

Region	Range	Functional group	Absolute Integral
1	4.39–3.98		2.17
2	3.84–3.63	CH_2-CH_2-O	2.60
3	3.62–3.48	S-CH_2	20.42
4	3.47–3.12		5.63
5	2.80–2.58		0.48
6	2.34–1.81	-CH, -CH-CH	44.58
7	1.80–1.50		4.26

8	1.51–1.36		18.17
9	1.33–1.25		1.69

GPC (Agilent 1260, USA) along with a refractive index detector, operating at a flow rate of 0.7 mL/min was utilized to evaluate the molecular weight distribution (Mw and Mn) and polydispersity index of the copolymer (Table 3.2). Before measurements, the copolymer was dissolved in a phosphate buffer (pH=7.2) at a concentration of 5 mg/mL.

Table 3.2 Properties and characteristics of the copolymer

Molar concentration (AMPS:AA:PEG)	0.05:0.05:0.015
Molar feed ratio (AMPS:AA:PEG)[a]	1:1:0.3
AMPS/AA[a]	3:10
PEG/AMPS+AA[a]	0.06:100
Molecular weight (M_n) (kg/mol)[b]	111.285
PDI (M_w/M_n)[b]	2.11

[a] Determined by ^{1}H-NMR, [b] Determined by gel permeation chromatography (GPC)

3.2.3. Electrokinetic studies

3.2.3.1.Determination of minimum copolymer content

To identify the minimum copolymer amount needed, the electrokinetic characterization focused on Si_3N_4 particles, which make up more than 90 wt. % of the multi-component ceramic system. A zeta potential analyzer (Malvern Instruments, Ltd., Zetasizer Nano series, UK) with a 633 nm laser and a scattered light detector set at a 173° fixed angle was used. Dispersions were prepared by individually dispersing 1, 5, and 10 mg of particles in 100 mL of DI water, resulting in particle concentrations of 0.00001, 0.00005, and 0.0001 g/mL, respectively. Each dispersion underwent 5 minutes of ultrasonication

in a bath sonicator for thorough mixing. An aqueous copolymer solution with a concentration of 0.0001 g/mL was then added to these suspensions to achieve copolymer concentrations ranging from 0.25 to 2.5 wt. % relative to the particle amount. The mixtures were sonicated for 5 minutes and then mechanically stirred for 2 minutes. Three measurements were taken at 25 °C, each consisting of at least 15 runs. The zeta potential and hydrodynamic radius for each copolymer concentration were determined by averaging these three measurements.

3.2.3.2.Determination of particle size

To determine the average particle size of the powder mixture intended for die-pressing in the fabrication of commercial parts, a mixture of Si_3N_4, $CaCO_3$, Al_2O_3, Sm_2O_3, Y_2O_3, and AlN was milled in a slurry form using wax and PVA as pressing aids. The average particle size, measured via DLS, was ~0.8 μm in the sample taken from this slurry. For comparison, the particle size of the mixture used to prepare self-standing doughs was measured. A suspension with a concentration of 0.00001 g/mL in DI water was prepared without milling, and the average particle size was found to be ~1.5 μm. Additionally, the pristine Si_3N_4 particle size was measured as 230 nm using DLS.

3.2.4. Preparation of the green bodies

A commercial-grade SiAlON composition, formulated by MDA Advanced Ceramics Inc. was prepared by milling the composition in DI water along with pressing aids and spray drying the milled slurry into granules (Calis Acikbas et al., 2012). These granules were then used to formulate self-standing doughs and die-pressed commercial-grade SiAlONs. Incidentally, to avoid energy-intensive processes, milling for the preparation of self-standing doughs was not used.

To identify the maximum solid loading exhibiting a dough-like consistency, a matrix with different particle loading amounts and additive content was prepared (Figure 3.4b). The solid content of the aqueous copolymer (ρ=1.06±0.01 g/cm^3) was determined to be ~21.2 wt. % using a solid content analyzer (Shimadzu, uniBloc MOC63u, Japan) before the dough preparation. DI water and additive were added gradually to the pre-weighted

ceramic particles and the suspensions were hand-mixed for 2 minutes until dough-like structures were achieved. Digital images of the suspensions were captured using a Canon EOS 650D camera. At around 72.7 wt. % particle loading in the presence of 2 wt. % additive produced the most consistent results. A 100 g dough of this composition comprises 72.7 g of particles, 25.9 g of DI water, and 1.4 g of additive. The volumetric composition of the dough is 46.39 % (v/v) SiAlON, 2.73 % (v/v) additive, and 50.88 % (v/v) DI water. In all compositions, the copolymer amount is reported relative to the weight of SiAlON particles.

A comparison of microstructural and selected mechanical properties was carried out with the commercially available wear part that was manufactured by MDA Advanced Ceramics Inc. through an automatic pressing machine.

3.2.5. Rheological characterization

An Anton-Paar MCR92 rheometer equipped with a parallel plate geometry of 25 mm with a fixed gap size of 1 mm was used to characterize the rheological behavior of ceramic suspensions at room temperature (25 °C). Samples with 70.1, 72.7, and 74.4 wt. % solid loading containing 2 wt. % additive were prepared. The shear rate was varied from 0.1 to 100 s^{-1}. 25 data points were taken (duration: 99.3 s). To obtain the storage and loss moduli in dynamic mode, the angular frequency was kept constant at 10 rad/s, while the strain increased from 0.001 to 100%.

3.2.6. Green machining of SiAlONs

The green bodies were dried at room temperature (20.4±1 °C) for 24 hours under a relative humidity of 52 %. Following the stabilization of the moisture content of the green body at ∼1.3 % (Figure 3.6a) after 18 hours, subsequent machining operations were performed. The machining was carried out using a bench-top 3-axis REVO M1A CNC milling machine (REVO, Türkiye), operating at a spindle speed of 10,000 rpm and a cutting speed of 1,000 mm/min (depth of cut: 0.2 mm). Solid carbide flat-end mill cutting tools with diameters of 1 mm and 2 mm (Kirtas Sert Metal, Turkiye) were utilized for the machining process. The flat-end mill was selected to ensure a smooth surface finish for precision and dimensional accuracy (Abbar Khleif & Nemat Hasan Nemah Khniefer, 2017; Dhara & Su, 2005; Feng & Menq, 1994; Vickers & Quan, 1989). The material

removal rate (mg/s) was then determined by tracking the weight loss during the machining process.

Optical microscopy (Sanqtid, China) and surface profilometry (Dektak 6M, USA) were employed to evaluate the quality of the machined surface before and after sintering. The surface roughness was determined using surface profilometry with a stylus-type profilometer featuring a 12.5 µm tip radius, applying a force of 2 mg. Measurements were taken perpendicular to the machining direction, with a selected horizontal travel distance of 7.5 mm (resolution 0.833 µm/sample) for machined surfaces.

3.2.7. Sintering profile, density measurements, and shrinkage

The green bodies were sintered by a two-step GPS cycle where the first step (pre-sintering) was carried out at 1900 °C for 1 h at 5 bar nitrogen gas pressure followed by a sintering step at 1950 °C for 1h at 50 bar nitrogen gas pressure (FCT, FPW 180/2200, Germany).

The density of the sintered bodies was determined using Archimedes' method. To assess the percentage of shrinkage during sintering of cube-shaped SiAlON samples, linear dimensional measurements were employed. A K-factor was introduced to quantify the percentage of anisotropic sintering shrinkage using Eq. (2.1)-(2.3) (Heunisch et al., 2010). The shrinkages were calculated along the x, y, and z direction for nine cubical samples, and the average is reported.

3.2.8. Microstructural characterization

The microstructural examination of the sintered SiAlONs was carried out with a Zeiss Supra 50 VP SEM (Germany) on polished samples using back-scattered electron imaging at an accelerating voltage of 20 keV, with a gold coating applied. For the assessment of tool wear, a JEOL LSM 6010 SEM (Japan) was used at an accelerating voltage of 5–10 keV, without any coating, due to the conductive nature of the sample.

3.2.9. Mechanical characterization

Vickers hardness (HV10) was evaluated using an indenter (Emco-Test Prüfmaschinen GmbH, Austria) with a 10 kg load applied for 5 seconds, following the ASTM-C1327 standard. Prior to testing, sintered samples having 20 mm diameter and 5 mm thickness were polished using an automated polishing machine (TegraPol-25, Struers). Five indentations were made and the fracture toughness of the materials was computed utilizing Niihara method (Niihara et al., 1982).

The flexural strength of green SiAlON samples (40 mm×5 mm×4 mm) was evaluated following an 18-hour drying period using a three-point bending configuration with a 25 mm span, employing a Universal Testing Machine (Zwick/Roell Z010, USA) at a testing speed of 0.2 mm/min.

3.3.Results and discussion

3.3.1. Formulating machinable SiAlON green bodies

The stability of Si_3N_4 dispersions was evaluated via zeta potentiometry in the presence of different amounts of the copolymer to determine the minimum amount of additive to prepare a dough (Figure 3.4a). The initial SiAlON suspension, in its pristine form (without the additive), displayed a zeta potential (ζ) of -45 mV at pH ~7 (Figure 3.4a). With the introduction of the additive, the zeta potential increased to -44 mV up to 0.5 wt. %, eventually reaching a plateau at ~-49 mV, indicating complete particle coverage (Schwarz et al., 1998) at 2.0 wt. % (Figure 3.4a). Concurrently, the average hydrodynamic diameter (h_d) initially decreased, followed by an increase beyond 2 wt. % additive. Ceramic particles had the smallest h_d at ~270 nm, aligning with the copolymer amount (2 wt. %) required for the full surface coverage of particles (Figure 3.4a). The upward trend in h_d with polymer dosages exceeding 2.0 wt. % is attributed to mechanisms such as polymer−polymer/free-polymer interactions and bridging flocculation (Doroszkowski, 1999; Furusawa et al., 1992; S. Kim et al., 2015; Piculell & Lindman, 1992a). Moreover, a wider size distribution and an h_d of ~600 nm at higher solid loadings (0.005 and 0.01 wt. %) were observed in the presence of a 2 wt. % copolymer (Figure 3.4).

A matrix that is composed of suspensions with 70.1, 72.7, and 74.4 wt. % particle loading and 1.75, 2, and 2.25 wt. % additive (Figure 3.4b) was prepared. At 70.1 wt. %, all

suspensions flowed rather than forming self-standing doughs. 74.4 wt. % loading although produced doughs at 1.75 and 2 wt. % additive content exhibited cracks. Overall, 72.7 wt. % solid loading and 2 wt. % additive content combination was singled out to formulate SiAlON doughs.

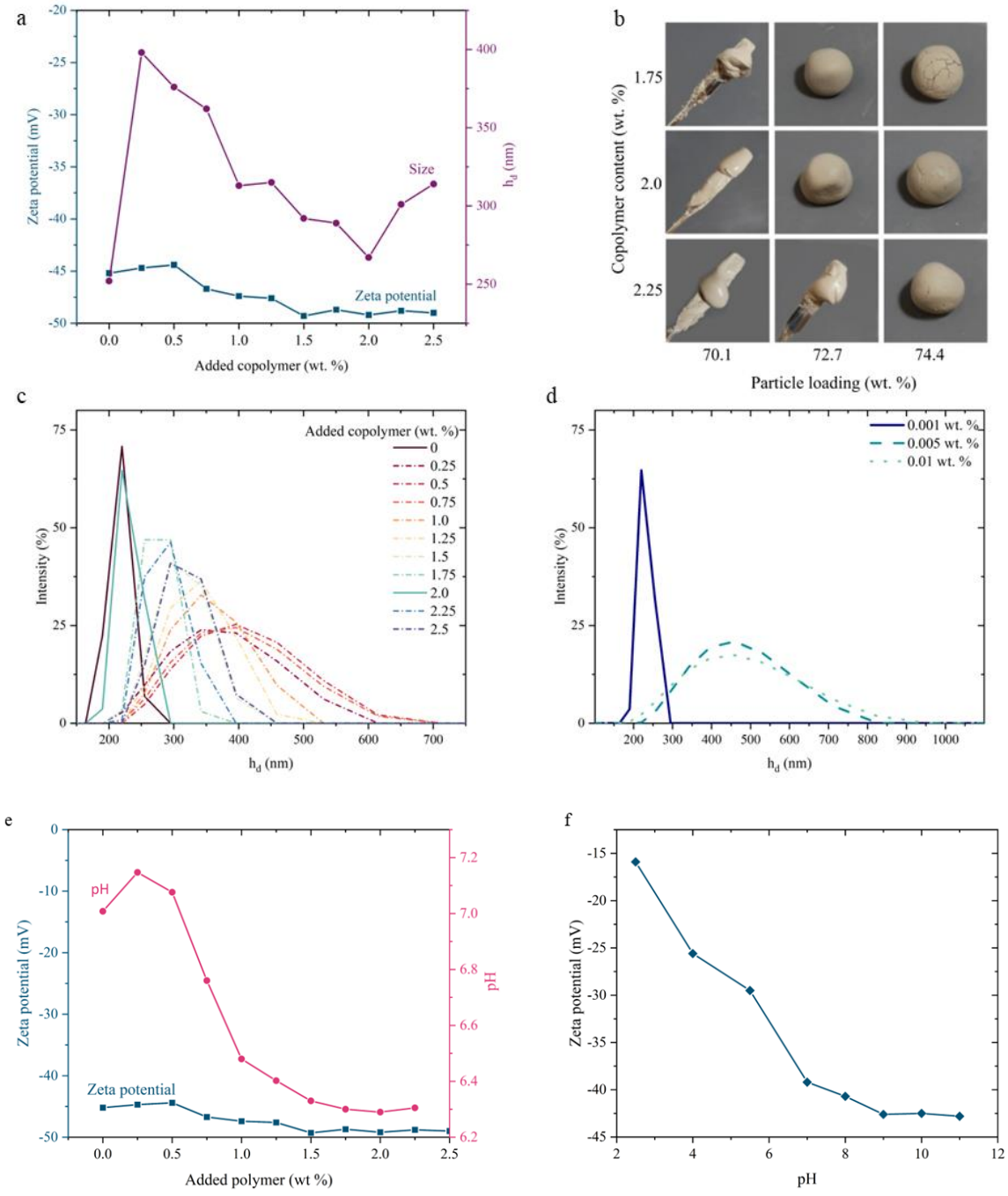

Figure 3.4 a) Zeta potential and h_d of pristine SiAlON particles, and with increasing copolymer content (visualized using a line plot), b) photographic matrix displaying suspensions at different compositions; intensity-weighted size distribution of c) 0.001 wt. % Si_3N_4 dispersion after addition of copolymer, d) 0.001–0.01 wt. % Si_3N_4 dispersion after addition of 2 wt. % copolymer, e) pH variation as a function of an added copolymer,

and f) effect of pH on zeta potential of pristine Si_3N_4 nanoparticles.

3.3.2. The flow behavior of SiAlON suspensions/doughs

The flow behavior of the ceramic suspensions (70.1–74.4 wt. %) in the presence of a 2 wt. % additive was characterized. While tracking steady state shear viscosity, 74.4 wt. % suspension crumbled upon the applied shear force and spread out of the measuring plate, hence assessing its flow behavior was not possible. The structural breakdown, especially with higher solid loading, is attributed to drying during the measurement. 70.1 wt. % suspension exhibited a paste-like behavior (Figure 3.4b and Figure 3.5a) with a relatively lower viscosity compared to the 72.7 wt. % counterpart. At shear rates ranging from 0.1 to 100 s^{-1}, both 70.1 wt. % and 72.7 wt. % SiAlON suspensions displayed a shear-thinning behavior. For the 70.1 wt. % suspension, the viscosity remained below 50 Pa·s in the measurement range and the system formed an "ink" rather than a dough, for instance, this formulation can be extruded from a syringe with ease. In contrast, the 72.7 wt. % SiAlON-loaded formulation exhibited a dough-like behavior across shear rates of 0.1 to 100 s^{-1}. There is a ~10-fold difference in viscosity at the shear rate of 10 s^{-1} between 72.7 wt. % and 70.1 wt. % loading, and sustaining a viscosity over 100 Pa·s is critical to achieve a malleable dough.

Figure 3.5b displays the viscoelastic properties of suspensions with different solid loadings. All suspensions exhibited an elastic behavior where the storage modulus is higher than the loss modulus (G′>G″). The trend of increasing yield stress and viscosity was consistent with the particle loading.

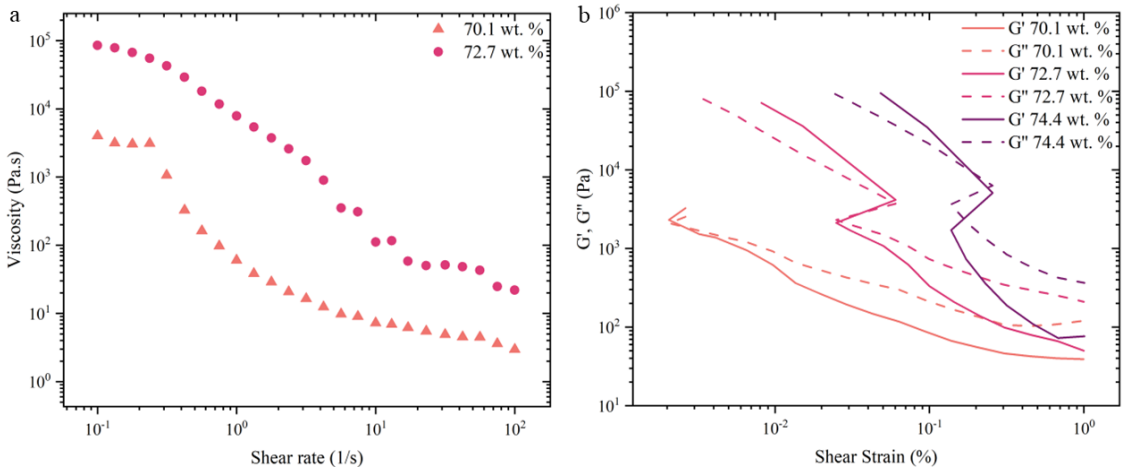

Figure 3.5 a) Viscosity as a function of shear rate and b) oscillatory rheological response of suspensions/doughs in the presence of 2 wt. % of additive with varied solid loading

(70.1–74.4 wt. %)

3.3.3. Green machining of SiAlONs

All hand-shaped objects demonstrated linear shrinkage of ~2.2% from molding to the dried state. To assess machinability, the moisture content of the molded doughs over 24 hours of drying (Figure 3.6a) under ambient conditions (temperature: 20.4±1 °C, relative humidity: 52%) was tracked using a solid content analyzer. The SiAlON dough exhibited a flexural strength of 0.5 MPa (Figure 3.6b), demonstrating its ability to withstand machining forces and maintain its structural integrity.

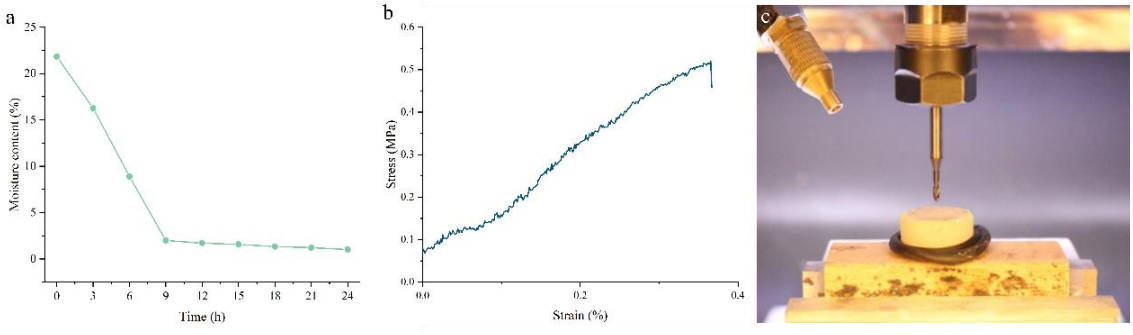

Figure 3.6 a) The moisture content of the dough that contains 72.7 wt. % SiAlON and 2.0 wt. % copolymer as a function of time, b) stress-strain curve of green SiAlON, c) fixation of the green body onto the CNC machine

To assess the performance of self-standing doughs during machining, tools with two different diameters, 1 and 2 mm, were used. Figure 3.7a and d show the optical images of the green compacts after machining. When machining a SiAlON surface in its green state using a 2 mm cutting tool, a higher degree of damage is observed at the edges compared to the case of a 1 mm cutting tool. The machinability of a material was assessed by evaluating wear at the cutting edge of the tool as well. In Figure 3.7c and f, SEM of the clearance faces of the tools following the machining of the SiAlON compacts are presented, no tool wear was observed in both cases.

The material removal rate for SiAlON with a 1 mm tool was estimated as ~6.46 mg/s while employing a 2 mm tool yielded a rate of ~12.32 mg/s. The averages of arithmetic surface roughness were 85±4.6 and 76±5.5 μm for the surfaces machined with 1 and 2 mm diameter tools, respectively (Figure 3.7g). The larger diameter of the 2 mm tool offers a broader contact area during machining, resulting in more uniform material removal and a smoother finish, hence a lower surface roughness (A. Mahyar Khorasani et al., 2012; W. Wang et al., 2005). Overall, employing a larger diameter tool for machining achieved

a smoother surface, and a small diameter tool performed better at drilling with lower edge damage.

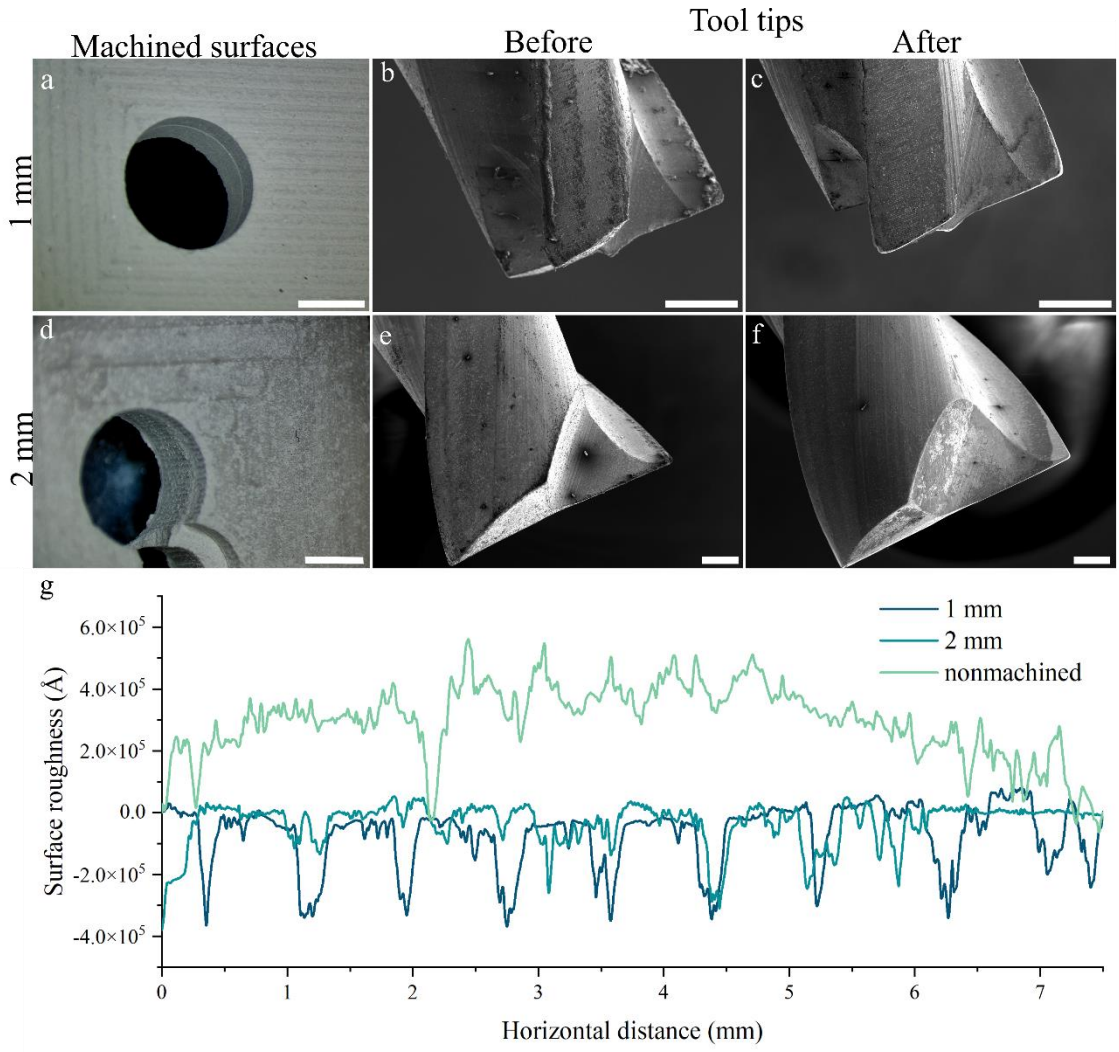

Figure 3.7 Upper row: a) A close-up of a hole machined using a 1 mm flat end tool, b) SEM micrographs of the surfaces of the 1 mm tool before use, c) 1 mm tool after use, middle row: d) a close-up of a hole machined using a 2 mm flat end tool, e) SEM micrographs of the surfaces of the 2 mm tool before use, and f) after use, lower row: g) surface roughness of the machined SiAlON surfaces with different tool diameters and nonmachined surfaces, scale bars on the optical images and SEM micrographs represent 2 mm and 250 μm, respectively.

3.3.4. Microstructural and mechanical characterization

In the preparation of commercial-grade wear parts, Si_3N_4 and pressing aid particles were milled to achieve a particle size of 0.8 μm before die-pressing. To design a low-energy process, milling was skipped, resulting in a final particle size of 1.5 μm for the Si_3N_4 and pressing aid particle mixture used to prepare SiAlON doughs.

Following GPS, molded objects exhibited a linear shrinkage of ~19 % from the dried state, achieving a sintered density of ~3.24 g/cm^3 (~99.99 % theoretical density). The average K_{xy}, K_{xz}, and K_{yz} were calculated as -1.04, -2.45, and 1.40 using Eq. (2.1)-(2.3), respectively. A large absolute value of the K-factor implies higher shrinkage anisotropy and K values ≥ 12 were associated with anisotropic shrinkage; thus, a K value of ~2 in this system was referred to as isotropic (Heunisch et al., 2010).

Figure 3.8a and b show SEM backscattered electron images of the sintered commercial-grade and self-standing SiAlON, respectively. In Figure 3.8a, and b, dark grains represent β-SiAlON, gray grains represent α-SiAlON and white spots represent the intergranular phase due to the sintering additives. Upon comparison with Figure 3.8a and b, it is evident that the sintered self-standing SiAlON comprises larger grains. These large grains in Figure 3.8b can be attributed to the absence of milling of the powders before dough preparation.

For the commercial-grade product, XRD patterns (Figure 3.8c) exhibit distinct peaks corresponding to both α-SiAlON and β-SiAlON phases, consistent with the observed dark and gray grains in Figure 3.8a. The presence of both α and β phases, as confirmed by XRD analysis, correlates with the observed microstructure and contributes to the mechanical properties of the commercial-grade product. XRD analysis of the self-standing SiAlON, which predominantly consists of β-SiAlON, shows sharp diffraction peaks corresponding primarily to the β phase. XRD analysis of the self-standing SiAlON, which predominantly consists of β-SiAlON, shows sharp diffraction peaks corresponding primarily to the β phase. AlN reacts with pure water at room temperature, forming an amorphous AlOOH layer on its surface, which converts to $Al(OH)_3$ as in reactions 3.1–3.3 (Krnel & Kosmač, 2,000):

$$AlN+2H_2O \rightarrow AlOOH+NH_3 \quad (3.1)$$

$$NH_3+H_2O \rightarrow NH_4^+ + OH^- \quad (3.2)$$

$$AlOOH+H_2O \rightarrow Al(OH)_3 \quad (3.3)$$

The ammonia (NH_3) produced in reactions 3.1 and 3.2 rapidly increases the pH of the slurry due to its basicity, causing particle agglomeration. As a result of particle agglomeration (flocculation), a stable ceramic slurry cannot be obtained. If reaction 3.3 occurs, the system becomes enriched with oxygen, leading to deviations from the desired chemical composition. These compositional changes due to these reactions can cause microstructural defects and changes in the phase amounts in the final product (Krnel & Kosmač, 2001). On the other hand, similar reactions occur during the interaction of Si_3N_4

with water, although their effects are not considered very strong. This is because Si_3N_4 can be easily prepared in aqueous environments (Krnel & Kosmač, 2001). It has been shown that Si_3N_4 powders with different grain sizes can hydrolyze under different grinding conditions, resulting in reaction 3.4 (Laarz et al., 2000; Özcan et al., 2017):

$$Si_3N_4+2H_2O\rightarrow 3SiO_2+4NH_3 \quad (3.4)$$

The oxide (SiO_2) layer on the surface of Si_3N_4 dissolves in aqueous environments. As a result of the reaction of SiO_2 with water, ortho-silicic acid ($Si(OH)_4$) is formed as in reaction 3.5:

$$SiO_2+2H_2O\rightarrow Si(OH)_4 \quad (3.5)$$

Hence, the destabilization of the small amount of α phase, the reduction in the crystallization degree, and the alteration in the chemical composition of the grain boundary phase suggest an increase in oxygen content within the system.

The hardness and extrapolated indentation fracture toughness of sintered self-standing SiAlONs were calculated as 13.48±0.35 GPa and 6.22±0.28 $MPa\cdot m^{1/2}$, respectively, aligning with the commercial-grade reference values of 14.40±0.39 GPa and 6.40±0.40 $MPa\cdot m^{1/2}$. The AlN hydrolysis reaction is base-catalyzed and influenced by hydroxyl ion concentration (Krnel & Kosmač, 2000, 2001). At low pH (~1), pH affects the reaction rate more than anions in the suspension. At higher pH (~3), the reaction rate reveals the impact of various acids (Krnel & Kosmač, 2000, 2001). Monoprotonic acids (HCl, HF, HNO_3) that fully dissociate and form water-soluble salts with aluminum do not affect hydrolysis, as they adsorb onto the powder surface without hindering water penetration to the AlN core. Incompletely dissociated diprotonic acids (H_2SO_4, H_2CO_3) adsorb more strongly due to higher anion charges and hydrogen bonding. Phosphoric acid anions, with even higher charges, can form chemical bonds with Al–OH groups on the powder surface, preventing water access to the AlN core (Krnel & Kosmač, 2000, 2001). This aligns with the finding of a negative zeta potential (Figure 3.4) in alignment with the literature (Krnel & Kosmač, 2000, 2001), suggesting that the comparable hardness achieved may result from suppressed hydrolysis due to the carboxylic and phosphoric acids in the additives used.

The difference in particle size contributed to the observed densification difference, with finer particles achieving higher density and, consequently, greater mechanical strength. Additionally, the larger particle size in the SiAlON dough resulted in ∼6.39% lower hardness and 2.81% lower indentation fracture toughness compared to the commercial-grade wear part. Despite these microstructural differences, significant variations in

fracture toughness were not observed, though the SiAlON shaped from the dough exhibited slightly lower hardness than the commercial wear part of the same composition.

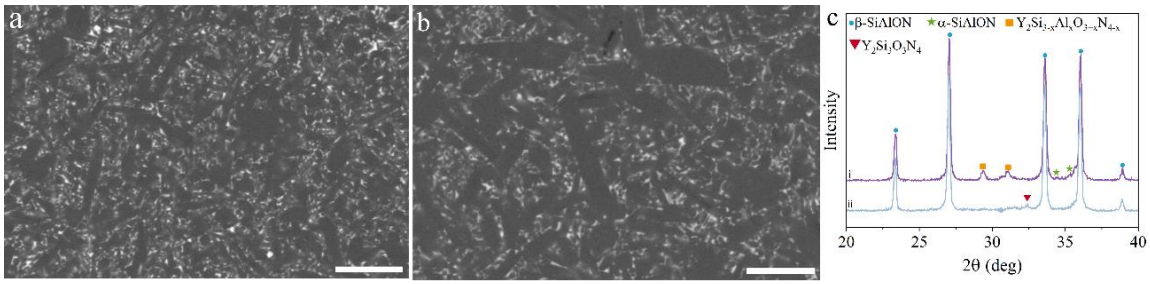

Figure 3.8 SEM back-scattered electron micrographs of a) a commercial-grade wear part, b) SiAlON part prepared from the dough (Scale bars represent 10 μm.), and c) XRD spectra of i) commercial-grade, and ii) self-standing SiAlON

3.3.5. Fabrication of custom-based shapes

The capability of the process and the fabrication of shapes that include holes, threads, and grooves were demonstrated to serve the distinct demands of the industry. The fabrication of high aspect ratio thin tubes from SiAlONs faced obstacles due to their inherent softness, which posed limitations in machining. Given the necessity for codes to enable the machining of complex geometries, complex shape production was showcased through molding as an alternative approach. A gear, a four-tooth comb, a clover, and a spline, which can be considered complex shapes, were prototyped (Figure 3.9). The process enables laboratories with limited materials engineering expertise to engage in ceramics processing for prototyping and low-volume fabrication without requiring expensive setups, aligning with the goal of affordability and accessibility.

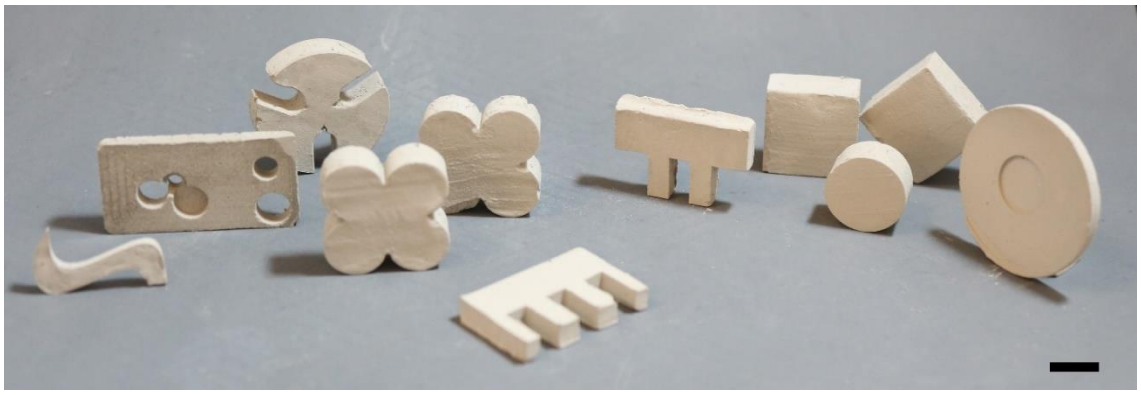

Figure 3.9 Custom-sized shapes at their green state after machining (Scale bar represents 1 cm.)

3.4.Conclusion

Near-net shaping of advanced ceramics often requires tailored solutions due to the brittle nature of ceramics. Currently, the industry lacks a straightforward approach for streamlining low-volume production and prototyping without investing in costly setups and molds. Recently, the preparation of self-standing doughs of advanced metal oxide ceramics was introduced to offer an easy-to-adapt and cost-effective shaping route. In this study, the portfolio has been expanded to include a multi-component ceramic system for fabricating SiAlON green bodies, demonstrating the feasibility of machining at the green state. Despite exhibiting significantly lower mechanical strength compared to other green body formulations, these doughs are malleable and sustain their structural integrity. Consequently, the near-net shaping of these materials can be handled at lower machining forces with minimal tool wear. Overall, this easy-to-implement, one-step coagulation method has the potential to enable the green machining of various types of advanced ceramics without requiring domain knowledge and existing setups.

Chapter 4

4. THE DESIGN AND PROTOTYPING OF CONTROLLED-RELEASE SYSTEMS FOR AGROCHEMICALS

This chapter is written based on the article “Coaxial direct ink writing of core-shell meshes enables zero-waste room temperature encapsulation of multivariate fertilizers” which was published in Colloids and Surfaces A: Physicochemical and Engineering Aspects in March 2024.

4.1.Introduction

Fertilizers improve crop growth with a projected worldwide use of 200 million tons in 2025 (International Fertilizer Association, 2021). Traditionally, fertilizers are either applied via foliar spraying or directly integrated into the soil during plantation. These deployment methods inherently fail to offer a homogeneous distribution and lead to excessive use of chemicals, whereby leaks to the nearby habitat are hard to prevent (FAO, 2001, 2019, 2021). Extensive use of agrochemicals has led to detrimental effects on the environment and human health. These chemicals, including fertilizers, pesticides, and fungicides, are often synthetic and their overuse can result in pollution of air and groundwater (Shang et al., 2019; Shaviv & Mikkelsen, 1993). Moreover, direct contact with fertilizers during deployment can be harmful to agricultural workers (Gurney et al., 1991). In the last three decades, efforts have been made to address these issues through devising delivery systems for fertilizers (Trenkel, 1997).

Core-shell structures, where the core material is coated with a polymeric shell, represent a prevalent release system. These structures can take the form of particles or fibers, with

fabrication methods categorized into chemical and physical approaches (Hack et al., 2012; Lawrencia et al., 2021; Nooeaid et al., 2021; Qiao et al., 2016; Tan et al., 2021). Chemical methods involve reactions or strong intermolecular forces such as electrostatic interactions, hydrogen bonding, and hydrophobic interactions, typically requiring high temperatures and generating chemical waste. Each ion of interest (e.g., Fe^{3+}, Zn^{2+}, Mn^{2+}) necessitates a separate step, complicating the use of these methods for multi-material systems. Physical methods, on the other hand, often use benchtop techniques at room temperature such as electrospinning and electrospraying (Bennacef et al., 2023).

The design of core-shell systems is influenced by factors including particle size and material selection. Formulation development considers the employed technology, shell composition, active ingredient properties, desired release mechanism, and intended application, including regulatory compliance and processing requirements. For agricultural chemicals, this involves using approved shell materials and designing small capsules to avoid clogging spray nozzles. Successful development often integrates new technologies into existing facilities to ensure cost-effectiveness. Ideally, these technologies should enable the encapsulation of multiple actives, especially those with similar properties like polarity or solubility. Core-shell particles for crop protection usually range from 1 to 20 micrometers, with methods such as interfacial polymerization, sol-gel technologies, and spray drying commonly used. Electrospun polymeric fibers are studied for plant nutrient delivery due to their high surface area-to-volume ratio compared to conventional polymer-coated fertilizers (Nooeaid et al., 2021). Coaxial electrospinning can prolong fertilizer delivery by enhancing structural stability, though it can only produce sub-100 μm fibers, limiting encapsulated material and release duration to hours or days (Javazmi et al., 2021; Malafatti et al., 2023; Scaffaro et al., 2023). Electrospinning also requires solvents and temperature control, adding to the carbon footprint (Angammana & Jayaram, 2016; Rathore & Schiffman, 2021; Yoon et al., 2018).

Industrial scale-up is crucial for the economic viability of new formulations, alongside ease of registration for controlled-release products. There is a need for low-carbon footprint fabrication methods that achieve high encapsulation efficiency and loading capacity. Coaxial direct ink writing (cDIW), a room-temperature mechanical approach, can produce sub-mm core-shell fibers by extruding two or more materials simultaneously. Unlike traditional methods such as coating, electrospraying, and chemical synthesis, cDIW can combine multiple nutrients without needing conductive polymers or organic solvents.

The potential of cDIW in mechanically encapsulating multivariate fertilizers, addressing the need for diverse chemicals for optimal plant growth and reducing excessive application, is demonstrated to produce a core-shell release system. Mechanical encapsulation in biodegradable polymeric shells is a zero-waste process, utilizing all materials without generating byproducts. Core and shell materials were selected for their rheological compatibility, biodegradability, non-toxicity, agricultural application studies, and resource sustainability (European Commission Directorate-General for Agriculture and Rural Development, 2019; Food and Agriculture Organization of the United Nations, 2018; Foroughi et al., 2021; Mohammed et al., 2023; United States Department of Agriculture, 2001). Polysaccharide-based polymer matrices, known to enhance crop growth and safety (Campos et al., 2015; Supare & Mahanwar, 2022; Tomadoni et al., 2019; J. Wang & Zhuang, 2022), were used for both inks. The optimal shell combination was sodium alginate (ALG), methylcellulose (MC), and hydroxypropyl cellulose (HPC), while the core ink used viscosity modifiers HPC and poly(ethylene glycol) (PEG). Fertilizer release kinetics were studied using ICP-OES, electrical conductivity, and FTIR. The 3D-printed meshes released 95% of the fertilizer within eight weeks. Compared to the system where the fertilizer was embedded in a polymeric matrix, the core-shell mesh released fertilizer about 14 times slower. Mechanical properties were tested via three-point bending and rollability tests, with load-bearing capacity assessed using standard weights. When used to grow wheat (Triticum aestivum L.), the core-shell meshes showed ∼1.7-fold and ∼1.5-fold shoot length growth compared to control and traditional methods in four weeks, respectively. This method is zero-waste, room temperature, and scalable, offering safe, easy-to-transport, flexible release systems. Advancing controlled-release systems for agrochemicals can address conventional application challenges and promote sustainable agriculture.

4.2.Materials and methods

4.2.1. Materials

PEG (MW 200 g/mol) was sourced from Merck, HPC (MW 10,0000 g/mol) and nitric acid (HNO_3, 70%) from Alfa-Aesar, and sodium alginate (SA, ALG, W201502),

methylcellulose (MC), from Sigma-Aldrich. Calcium chloride dihydrate ($CaCl_2.2H_2O$, food grade), COMBI-MAX fertilizer (particle size 0.01–1 mm), and Triticum aestivum L. seed (Product No. 1016) were procured from ZAG Kimya, GMT Tarım, and Tekfen Agri, respectively. DI water with a resistivity of 18 MΩ·cm was obtained from a Milli-Q water purification system (Millipore, USA).

4.2.2. Preparation of the inks

4.2.2.1.Preparation of MC-based shell inks

The combinations of MC, HPC, PEG, and ALG were tested based on their mechanical properties upon drying and compatibility with the core ink. The material combinations and their formulations that were referred to as "non-optimized" were provided in Table 4.1–

Table 4.3. ALG, HPC, and PEG were dissolved in deionized water, whereas poly(ε-caprolactone) (PCL) was dissolved in chloroform at their respective weight percentages.

Table 4.1 Combinations of ALG and HPC for shell ink

Ink	ALG (wt. %)	HPC (wt. %)	ALG:HPC
AH1	10.0	3.3	3:1
AH2	12.7	2.5	5:1
AH3	12.9	0.8	16:1
AH4	13.0	2	6.5:1
AH5	18.7	6.3	3:1
AH6	21.4	7.1	3:1
AH7	9.6	3.2	3:1

Table 4.2 Combinations of ALG and PEG for shell ink

Ink	ALG (wt. %)	PEG (wt. %)	ALG:PEG
AP1†	1.8	25.4	1:14
AP2†	1.9	22.6	1:11.9
AP3†	2.0	19.6	1:9.8
AP4†	2.1	16.3	1:7.8
AP5†	2.1	12.8	1:6.1
AP6‡	12.7	2.5	5.1:1
AP7‡	12.2	6.1	2:1
AP8‡	10.9	23.0	1:2.1

AP9‡	12.9	22.5	1:1.7

† The molecular weight of PEG is 1,000 g/mol.

‡ The molecular weight of PEG is 10,000 g/mol.

Table 4.3 Combinations of ALG and PCL for shell ink

Ink	ALG (wt. %)	PCL (wt. %)	ALG:PCL
APC1	6.7	16.6	1:2.5
APC2	4.4	18.3	1:4.2
APC3	8.7	14.4	1:1.7

To determine the printability range of MC-based shell inks (S), the flowability of MC-ALG solutions was tracked for MC:ALG weight ratios ranging from 0:1 to 5:1 (Figure 4.5). To obtain MC-ALG inks that are given in Table 4.4, i) aqueous stock solutions of ALG were prepared, ii) these stocks were cross-linked with 3 mg/ml $CaCl_2$ solution, and iii) they were magnetically stirred at ~300 rpm for 12 hours at room temperature. Thereafter, to tailor printability, corresponding amounts of MC were added to the blend and the mixing continued until the MC powder was fully dissolved at 80 °C.

Table 4.4 Combinations of MC and ALG for the optimization of the shell ink

Ink	MC (wt. %)	ALG (wt. %)	MC:ALG	ALG:$CaCl_2$
S1	2.90	1.45	2:1	40:1
S2	6.79	2.72	2.5:1	40:1
S3*	4.50	1.50	3:1	25:1
S4	8.03	2.68	3:1	40:1
S5	5.19	1.30	4:1	28:1
S6	6.58	1.32	5:1	17:1

*S3 was decided as the optimal formulation, and it was used in degradation and plant growth throughout this study.

4.2.2.2.Preparation of fertilizer-loaded core inks

The formulations of the core inks (C) containing fertilizer are provided in Table 4.5. Initially, PEG200 was mechanically mixed with the fertilizer at 360 rpm until a

homogeneous mixture was achieved at room temperature. Next, appropriate amounts of HPC were added to the blend to enhance viscosity. The mixture was then mechanically stirred continuously until uniformity was obtained.

Table 4.5 Core ink formulations

Ink	Fertilizer (wt. %)	HPC (wt. %)	PEG (wt. %)
C1*	18.0	9.0	61.8
C2	12.0	6.0	82.0
C3	12.0	9.0	79.0
C4	17.0	8.5	74.5
C5	23.7	2.4	73.9
C6	23.1	4.6	72.3
C7	19.0	9.5	71.5
C8	22.9	5.7	71.4
C9	16.0	16.0	68.0
C10	21.6	10.8	67.6

* Only this formulation contains deionized water (11.2 wt. %), it is the chosen formulation for the core ink.

4.2.3. Coaxial direct writing of core-shell meshes

The inks were gently mixed and loaded into a 3-cc printing cartridge fitted with a 15/19-gauge stainless steel coaxial nozzle. Before printing, the MC-ALG ink inside the cartridge was centrifuged (Centrifuge 5810, Eppendorf, Germany) for 15 minutes at 5000 rpm to eliminate air bubbles. The extrusion pressure was determined as the pressure at which a continuous ink flow started from the nozzle tip, ensuring stable flow and preventing buckling during printing. The inks were printed onto a Teflon surface at 22 °C using an extrusion-based coaxial printer with a pneumatic system (Axo A1, Axolotl Biosystems, Turkiye). The distance from the needle tip to the surface was set to ~5 mm to avoid ink accumulation at the outlet. To achieve the recommended fertilizer loading (~2 mg/cm² as per product information), a printing infill of 8% was used. A constant printing speed of 1 mm/s was maintained for all inks to ensure the formation of continuous filaments. The number of layers (two, four, or six) and the print geometry were customized to deliver

the specified amount of fertilizer to the soil in the desired application area. After cDIW, the meshes were dried under ambient conditions.

4.2.4. Rheological analysis

The rheological properties of the inks were analyzed using an MCR 302 Anton Paar rheometer equipped with a 25 mm diameter stainless steel cone and plate, with a cone angle of 2° and a truncation gap of 103 μm, at room temperature. To prevent sample evaporation and moisture exposure during measurements, a thin layer of paraffin oil with a viscosity of 0.2 Pa·s at room temperature was applied around the outer edge of the plates. For steady-state tests, viscosity was measured across shear rates ranging from 0.01 to 1,000 s^{-1}. In the dynamic regime, the frequency was set to 10 rad/s, and the strain ranged from 0.01 to 1,000%.

4.2.5. Determination of the fertilizer content and loading capacity

The chemical content of fertilizer was determined through i) XRD, ii) FTIR, and iii) ICP-OES:

i) In XRD, fertilizer was ground into a fine powder prior to analysis. Patterns were collected using a Bruker D2 PHASER desktop X-ray diffractometer with a step size of 0.02° and 0.1 s per step, measuring between 5 and 90° 2θ. The radiation source was Ni-filtered CuKα.

ii) The presence of salts of zinc, copper, manganese, and iron in the fertilizer was confirmed in the middle infrared range (wavenumber from 4000 to 400 cm^{-1}) at 2 cm^{-1} resolution with 64 scans and corrected against an air background (Thermo Scientific, Nicolet iS10).

iii) In ICP-OES, certain amounts of fertilizer powder were dissolved in 10 ml of deionized water, then the solutions were filtered with a syringe filter having 0.45 μm pore size to remove particles that may clog the nebulizer. The solutions were digested with 1 vol % acid (70% HNO_3) for metal dissolution.

The loading capacity (LC) of the mesh was estimated by dividing the amount of fertilizer in the core ink (18 wt. % of core formulation) that was loaded into the mesh over the total weight of the mesh, using Eq. (4.1),

$$LC\ (\%) = 100 \times E/W \tag{4.1}$$

where E_f is the total amount of fertilizer encapsulated in fibers (mg), and W is the average

weight of nine meshes (g).

4.2.6. Imaging

The core-shell structure of the meshes was analyzed using optical microscopy (Nikon Eclipse ME600, Tokyo, Japan). Digital images were captured with a Spot Insight QE camera (Diagnostic Instruments, Silver Spring, USA). To obtain images of the cross-sections of the printed meshes, the samples were immersed in liquid nitrogen and then physically broken. Various magnifications were used to capture images in dark field mode with episcopic illumination at room temperature. The shell thickness of the printed meshes was estimated using Image-J software (National Institutes of Health, Wayne Rasband, Bethesda, MD, USA). For further examination, scanning electron microscopy (SEM, JEOL JSM 6010, Japan) was utilized. The samples were fractured in liquid nitrogen to expose the core-shell structure and then fixed onto specimen stubs at a 90° angle for cross-sectional imaging. To prevent charging, the samples were coated with a ~9 nm layer of Au/Pd using a Cressington 108 sputter coater at 40 mA for 60 seconds.

4.2.7. Mechanical testing

The 3-point bending tests were conducted using a universal testing machine (Model Z100, Zwick/Roell, Germany) equipped with a 10 kN load cell, adhering to the ASTM D790 standard. The test specimens measured 50.8 mm in length and 12.7 mm in width, with thicknesses below 1.6 mm, and were supported over a span of 25.4 mm. A crosshead speed of 1 mm/min was used, consistent with previous studies (Raj et al., 2021; Tripathi & Kumar, 2011). Five samples for each ink formulation were tested and displacement-load curves were generated. Additionally, the load-bearing capacity of 7.5 cm×7.5 cm meshes was evaluated by supporting cast-iron calibration weights ranging from 10 to 500 g.

4.2.8. Degradation kinetics

Degradation kinetics were monitored over eight weeks using 24 mesh constructs, comprising three replicates each of shell and core-shell meshes. A simultaneous one-week

study examined the degradation of fertilizer mixed with the MC/ALG/HPC/PEG polymer matrix. Both the meshes and the fertilizer-polymer mixture were immersed separately in Falcon tubes containing 40 mL of deionized water at room temperature. Each week, three meshes were removed and dried until they reached a constant weight. The average weight loss of these three replicates was calculated using Eq. (4.2), where the degradation rate is expressed as a percentage of weight loss over the degradation period:

$$\text{Weight loss } (\%) = \frac{W_i - W_t}{W_i} \times 100 \tag{4.2}$$

W_i is the initial weight (g) and W_t is the dried weight (g) post-immersion at time t. Due to the soluble nature of the fertilizer-polymer matrix, its weight loss could not be tracked. The degradation of the specimens was analyzed using FTIR Spectroscopy (Nicolet™ iS10, Thermo Scientific, USA) before and after hydrolytic degradation, within the range of 400 to 4000 cm^{-1} using 64 scans at a resolution of 2 cm^{-1}.

4.2.9. The ion release behavior and kinetic model

Ion release from the degradable mesh was quantified using ICP-OES (Agilent 5510). During the degradation kinetics study, a 0.2 mL aliquot from each Falcon tube containing the mesh was diluted to 40 mL with DI water weekly and filtered through a 0.45 μm pore size filter to remove particles that could clog the nebulizer. The solutions were then digested with 1 vol % acid (70% HNO_3) to ensure metal dissolution. The average ion concentrations released from three meshes were reported weekly. Concurrently, electrical conductivity (EC) was measured to evaluate the degradation rate of both the meshes and the fertilizer-polymer matrix mix using a WTW inoLab pH/Cond 720. The release behavior of the degradable meshes and the polymer matrix was expressed as EC (μS/cm) over immersion time. To analyze the release mechanism, the Ritger-Peppas model was applied to fit the cumulative ion release curve using Eq. (4.3):

$$\frac{C_t}{C_\infty} = kt^n \tag{4.3}$$

where C_t and C_∞ denote the electrical conductivity resulting from ions released at time t and when ions are fully dissolved, respectively. t is the release time, k is a constant, and n is the diffusion exponent characterizing the release mechanism.

4.2.10. The design of the plant study and application of the meshes

A plant study was designed to showcase the application of these meshes. The suggested application amount of the commercial-grade fertilizer (~2 mg/cm^2, as per the production information) referred to as "x", was applied onto pots. Pots were filled with 210 g of soil, having an 8 cm diameter surface area of 50.2 cm^2. The suggested amount of fertilizer per pot, x, was calculated as 100 mg. Each pot was planted with five Triticum aestivum L. seeds, weighing 45±2 mg each. The soil used had a pH of 8.0 and a low organic matter content of 1% (Torun et al., 2019), originating from an ion-deficient region in Eskişehir, Türkiye. The plant height of Triticum aestivum L. was used as a non-destructive indicator to evaluate the relative growth-promoting effects (Tiwari et al., 2011) of different fertilizer application methods. The experimental setup and fertilizer content for each application are detailed in Table 4.6 and illustrated in Figure 4.1.

Two fertilizer application modes were tested: traditional (T) and mesh (M), indicated by the prefixes T and M, respectively. The abbreviation "Ct" represents the control group with no fertilizer applied. The control samples included: i) Ct1, a blank sample with no chemicals, ii) Ct2, with only the shell material, and iii) Ct3, with only the core material applied via syringe, as the HPC-PEG mixture was not printable without the fertilizer due to low solid content. All plants were watered daily with 10 ml. The fertilizer load was adjusted by varying the infill percentage and the number of layers. For instance, Mx and Tx, and M2x and T2x had similar fertilizer loads of ~ 100 mg and 200 mg, respectively. The treatments Ct1, Ct2, Ct3, Tx, T2x, T3x, M0.7x, Mx, and M2x used a total of 15, 5, 5, 15, 15, 5, 5, 10, and 10 seeds (5 seeds per pot), respectively.

Table 4.6 Nomenclature of the samples used in the assessment of the plant growth, and their corresponding layer numbers and infill percentages (if printable), fertilizer loads

Sample	Mode of application	Layer number	Infill %	Fertilizer load (mg)	Application concentration (mg/cm^2)
Ct1	No fertilizer	N/A	N/A	0	0
Ct2	No fertilizer	2	8	0	0
Ct3	No fertilizer	N/A	N/A	0	0
Tx	Traditional	N/A	N/A	100	2
T2x	Traditional	N/A	N/A	200	4
T3x	Traditional	N/A	N/A	300	6
M0.7x	Mesh	2	5	70	1.4

Mx	Mesh	2	8	103	2.1
M2x	Mesh	4	8	210	4.2

N/A: Not applicable as Ct1, Ct3, Tx, T2x, and T3x were not printable.

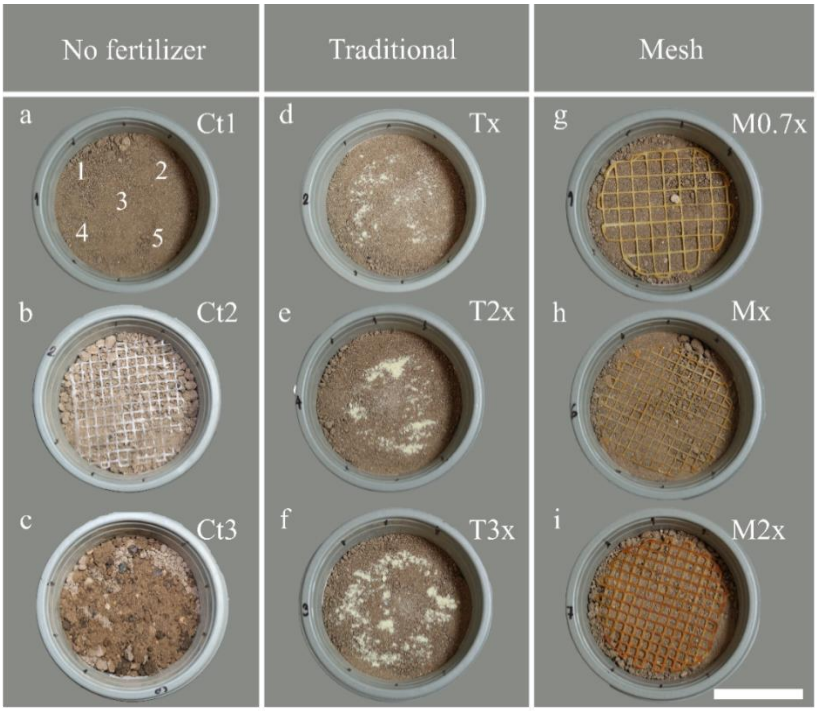

Figure 4.1 The experimental setup illustrates the application modes for: a) Ct1 (no fertilizer) with seed coordinates (1–5), b) Ct2 (printed with S3 formulation), c) Ct3 (C1 formulation without fertilizer), d) Tx, e) T2x, f) T3x, g) M0.7x, h) Mx, and i) M2x. The scale bar indicates 5 cm.

4.3.Results and discussion

4.3.1. Selection of the ink materials

In cDIW, ensuring the physical and chemical compatibility of core and shell inks, as well as controlling their flow behavior, is crucial for effectively encapsulating the core material and achieving consistent core-shell morphology along the length of the fiber. Various polysaccharide-based systems, such as ALG, cellulose, chitin, starch, and chitosan, have been explored for delivering agrochemicals due to their ability to improve crop growth simultaneously (Supare & Mahanwar, 2022; Tomadoni et al., 2019; J. Wang & Zhuang, 2022). Among these, chitin and chitosan require a harsh solvent (e.g., acetic acid or sodium hydroxide/urea) for dissolution at room temperature (Bisht et al., 2021; J. Wang & Zhuang, 2022; Zhong et al., 2020). On the other hand, starch has poor mechanical properties, it needs chemical (e.g., etherification, esterification, grafting, and

oxidation) or physical modification (e.g., pre-gelatinization, microwave, and heat-moisture treatment) to be printable (Amaraweera et al., 2021; Li et al., 2022; Rong et al., 2023). In this study, the shell ink formulation involved ALG, combined with cellulose derivatives (MC and HPC), chosen for their good water solubility and viscosity-modifying properties (Dai et al., 2019; Tang et al., 2023; J. Wang & Zhuang, 2022; Xu et al., 2018). ALG was particularly chosen for its ability to improve the water retention and mechanical properties of cellulose derivatives through hydrogen bonding (Mignon et al., 2019; Zamboulis et al., 2022). The solid loading of these aqueous inks was limited by their ability to be extruded at a pressure within the printer's working range. The upper limit of the solid loading of these aqueous inks (ALG-HPC: ~28.5 wt. %, MC-ALG: ~11 wt. %) was set based on their ability to be extruded from the nozzle at a pressure within the working range of the printer. Upon printing, ALG-HPC blends lacked dimensional stability and experienced considerable shrinkage (up to ~50%) leading to brittle structures, which restrict their use in a rolled or folded form for ease in transportation. These ALG-HPC formulations and their printed structures are given in Table 4.1 and Figure 4.2, respectively.

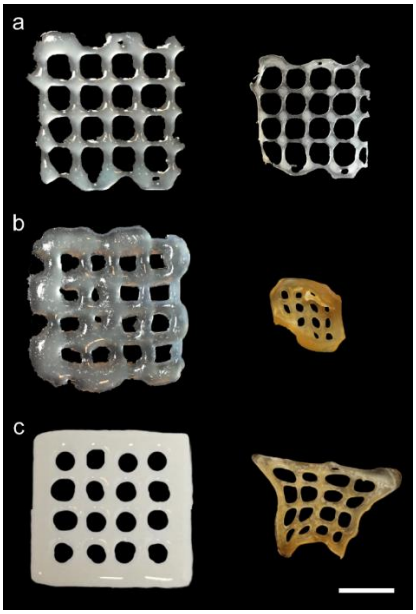

Figure 4.2 Digital images of ink formulations: a) AH2, b) AH3, c) AH4, showing poor printing performance. Scale bars represent 1 cm. Images on the left were taken 5 minutes after printing, and images on the right were taken 1 day after printing.

The visual for non-optimized ALG-PEG (AP) inks is provided in Figure 4.3. One limitation of these ink formulations is their tendency to experience dimensional instability and considerable shrinkage upon printing. This led to the formation of brittle structures upon drying, restricting their use in certain applications where dimensional stability is

crucial, such as in rolled or folded forms for ease of transportation. The shrinkage and brittleness of these inks impact the structural integrity of printed objects, potentially limiting their utility.

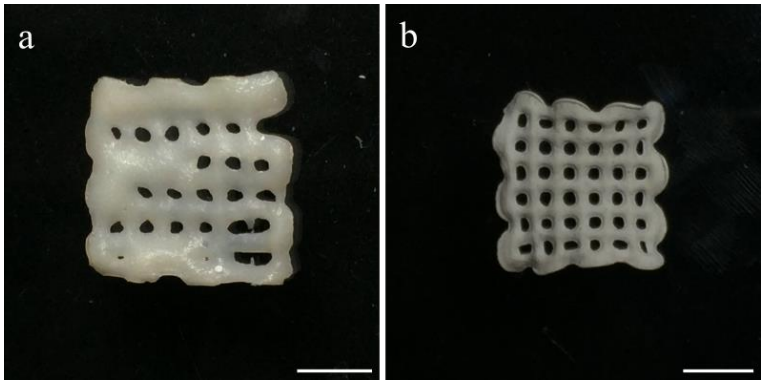

Figure 4.3 Digital images of ink formulations:a) AP6 (image taken 6 hours after printing), b) AP7 (image taken 1 day after printing), demonstrating poor printing performance. Scale bars represent 1 cm.

Inks that were prepared with organic solvents were also investigated. An unsuccessful printing example is given in Figure 4.4, when C3 was used as a core ink and ALG-PCL as a shell ink. In Figure 4.4a and b, the fast solidification of ALG-PCL due to the presence of chloroform in the formulation caused dried lumps on the mesh that restricted the nozzle movement. The presence of water-soluble sodium alginate and chloroform-soluble PCL led to phase separation if they were not mixed well before filling into the printing cartridge, in Figure 4.4c, and a visible phase separation was observed.

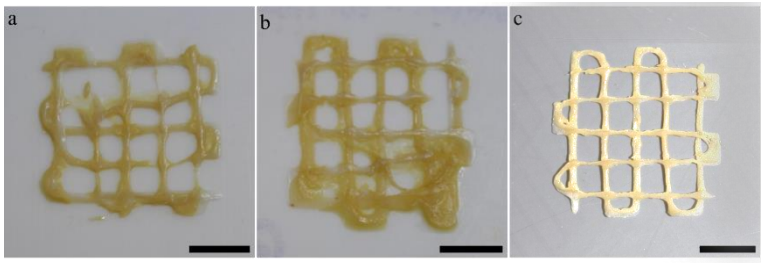

Figure 4.4 Digital images demonstrate the printing studies with a non-optimized fertilizer mixture (C3) with ALG-PCL shell, scale bars represent 1 cm.

On the other hand, all MC-ALG formulations (S1–6) were printable, and they retained their shape upon printing while their brittleness increased proportionally with the solid content (from 4 to 11 wt. %). Therefore, MC-ALG formulations were further assessed to determine the optimum ink.

Figure 4.5 shows the photographs of MC-ALG solutions at different weight ratios varying between 0:1 and 5:1, and a solid content of 2–12 wt. % at room temperature. Among

these, S4—the ink with the highest MC content (~8.0 wt. %)—exhibited significant resistance to flow. In comparison, S2 had a lower MC content (~6.8 wt. %) but a similar ALG content (~2.7 wt. %), allowing it to flow more easily than S4. S6 had a comparable MC content (~6.6 wt. %) to S2, but a lower ALG content (~1.3 wt. %) and higher crosslinking ratio (17:1), resulting in better resistance to flow than S2. Meanwhile, S3 and S5, with comparable solid content (~6.0 and ~6.5 wt. %), demonstrated similar resistance to flow. Samples with 0:1, 1:1, and 2:1 weight ratios of MC:ALG flow freely without the need for external pressure. The sample with a 5:1 weight ratio required a printing pressure that was higher than the capacity of the printer ($P>5.5\times10^5$ Pa). The solid content (g) in Figure 4.5 is the sum of MC and ALG to prepare ink of 10 ml.

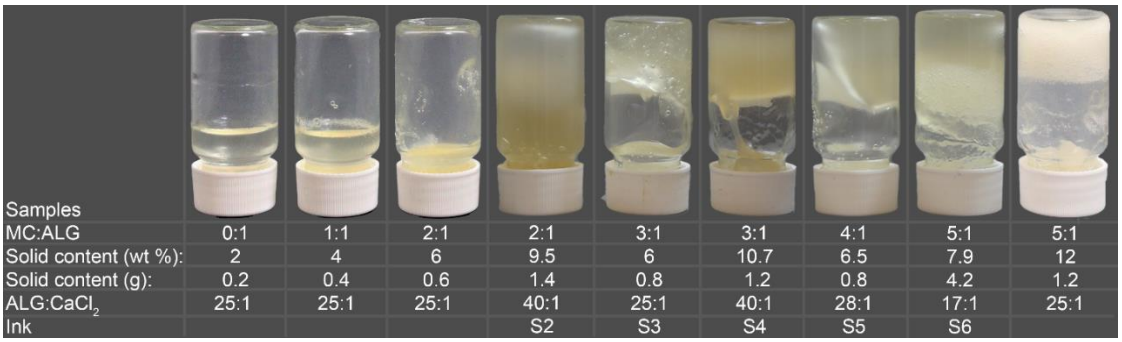

Figure 4.5 The vial upside-down images of the solutions with varying MC:ALG weight ratios and solid content illustrate that the solutions with high viscosities showed resistance to flow.

The core ink was formulated to host the fertilizer, where the polymer matrix is expected to act as a carrier through the soil and tailor the particle release together with the shell. In alignment with previous reports, PEG coupled with HPC was chosen as an agrochemical carrier (Gao et al., 2021; Garduque et al., 2020; Pascoli et al., 2018). They act as a viscosity-modifying agent for the fertilizer to be printable and ensure a fully aqueous system.

Figure 4.6 shows the XRD patterns of fertilizer (25.4% crystallinity). A series of Bragg peaks at 2θ values of 21.7°, 24.4°, 27.4°, 33.8°, and 36.9° appeared at ambient temperature, the peaks showed a good match with the XRD patterns of crystalline manganese(II) sulfate ($MnSO_4$, PDF #33-0906), iron(II) sulfate ($FeSO_4$, PDF #83-0078), zinc sulfate ($ZnSO_4$, PDF #01-0621), and copper sulfate ($CuSO_4$, PDF #12-0782) at room temperature.

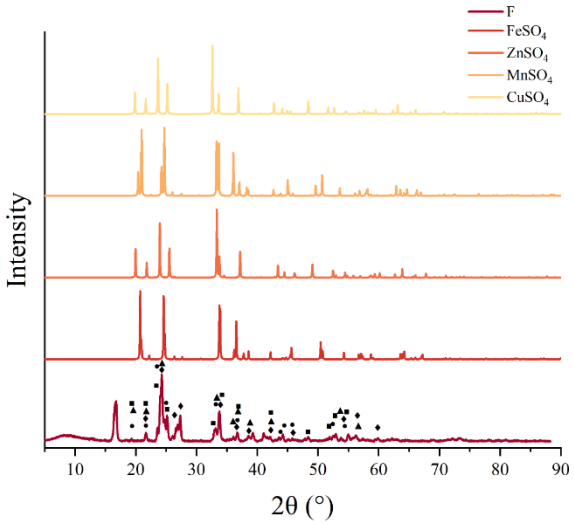

Figure 4.6 XRD pattern of fertilizer (F) and reference metal salts (Dark blue square, gray triangle, pink sphere, blue diamond shape represent peaks that matched with reference $CuSO_4$, $MnSO_4$, $ZnSO_4$, and $FeSO_4$, respectively.)

FTIR spectrum of fertilizer in Figure 4.7 was compared with spectra of manganese(II) sulfate ($MnSO_4$), iron(II) sulfate ($FeSO_4$), zinc sulfate ($ZnSO_4$), and copper sulfate ($CuSO_4$) listed in HR Inorganics library and National Institute of Standards and Technology (NIST) database. The broadband structure between 3600–3200 cm^{-1} results from the hydrogen bonding of the -OH groups between molecules, showing that the fertilizer was moisturized. The single broad peaks around 1100 cm^{-1} are assigned to different sulfates.

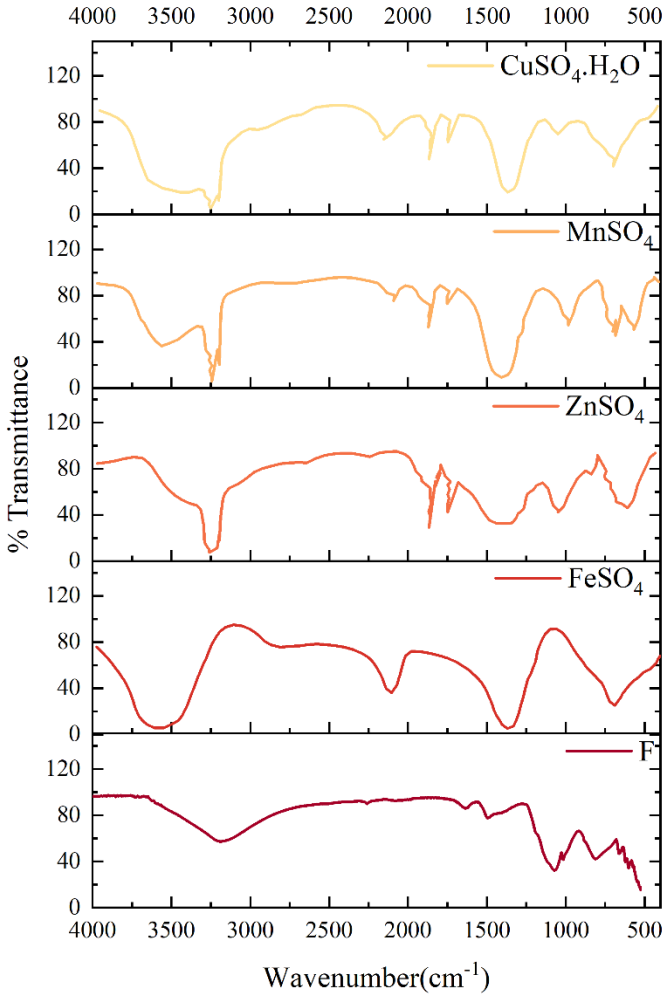

Figure 4.7 FTIR spectrum of the fertilizer and its comparison with FTIR spectra of references retrieved from NIST database and HR Inorganics library

The ion concentration in 10 ml of water was provided in Figure 4.8, showing that the concentration of ions in the solution matched with the added amount of fertilizer.

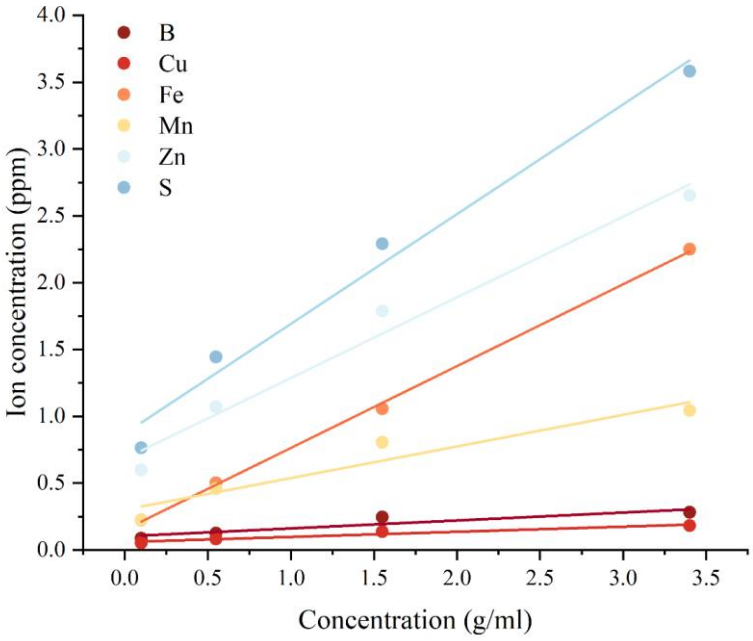

Figure 4.8 Ion concentration of stock fertilizer solutions at different concentrations

In terms of printability, core inks that contain HPC lower than 9 wt. % with a total solid (fertilizer and HPC) content of less than 27 wt. % (C2–5) could not be encapsulated as they readily diffused out of the shell after printing. Core inks that possess a solid content greater than 27 wt. % (C6–10) failed to be continuously printed, partially clogging the nozzle due to the increased viscosity. This increase was attributed to the greater number of hydrogen-bonding sites between the hydroxyl groups of HPC and the ether of PEG molecules (Sudharsan Reddy et al., 2012). Although C1 and C7 have comparable solid content (C1: 27 wt. %, C7: 28.5 wt. %), the difference in their printing performance was due to the presence of water (C1: 11.2 wt. %, C7: no water) that dissolved HPC and the fertilizer. Since C1 was the only formulation that was printable, it was singled out as the core ink. The optimized inks, C1 for the core and S3 for the shell were printed with an air pressure of 4.5×10^5 and 1.4×10^5 Pa, respectively.

The rheological response of the inks was evaluated to determine the compatibility of the core and shell inks by measuring their apparent viscosity, yield stress, storage (G'), and loss moduli (G''). The analysis focused on the optimum core ink formulation, C1, and its response was compared with the shell inks to ensure a compatible viscosity for a coherent flow. All ink formulations that are given in Figure 4.10a exhibited shear-thinning behavior allowing the ink extrusion through the nozzle which is characterized by decreasing viscosity with increasing shear rates. In terms of compatibility of viscosity

during extrusion, the flow behavior of shell inks S3 (MC:ALG of 3; total solid content 6 wt. %) and S5 (MC:ALG of 4; total solid content 6.5 wt. %) were found similar to C1 (Figure 4.10a). S3 and C1 are shear thinned with an apparent viscosity of $\sim 10^2$ Pa·s at a shear rate of 1 s^{-1}. To determine the most compatible shell ink between S3 and S5, three-point bending tests were carried out in addition to the rheological assessment. Based on flexural stress at break and flexure modulus, S3 showed ~72x and ~6x better performance compared to S5, respectively; hence, S3 was chosen as the shell ink.

To evaluate the shape retention of extrudates, elastic properties, and yield stress of the chosen core and shell ink, C1 and S3 were investigated via oscillatory measurements (Figure 4.10b). C1 and S3 exhibit nearly identical plateau storage moduli ($G' \approx 4.3\times10^2$ and 2.4×10^2 Pa) and yield stresses ($\tau_f \approx 226$ and 186 Pa). The relative magnitude of G' and G" (i.e., G"> G') shows the viscous liquid-like behavior of C1. At low shear rates, G' remained constant for C1 and S3, and a linear viscoelastic region (LVR) was observed (Figure 4.10b). The condition of G'>G" confirmed the solid-like behavior of S3 in LVR, the broad LVR indicated high resistance to the applied stresses to maintain the structures. This behavior was attributed to cross-linking of the ALG with $CaCl_2$ for S3. The gradual decrease in G" indicated the collapse of the structure of the material and subsequent breakdown resulting in a liquid-like behavior. The shear stress at the inner nozzle wall was estimated as 1.5×10^5 Pa for C1 by using Eq. (4.4)

$$\tau_\omega(r)=\frac{\Delta P}{2L_c}r \tag{4.4}$$

where ΔP (Pa) is the applied pressure, L_C (mm) is the length of the inner nozzle, and r (mm) is the core nozzle radius in Figure 4.9. The volumetric flow rates (Q) of core and shell ink were estimated as 3.33×10^{-2} and 6.03×10^{-2} mm^3/s, respectively by considering the time to finish one layer with a printing speed of 1 mm/s and the length traveled for one layer.

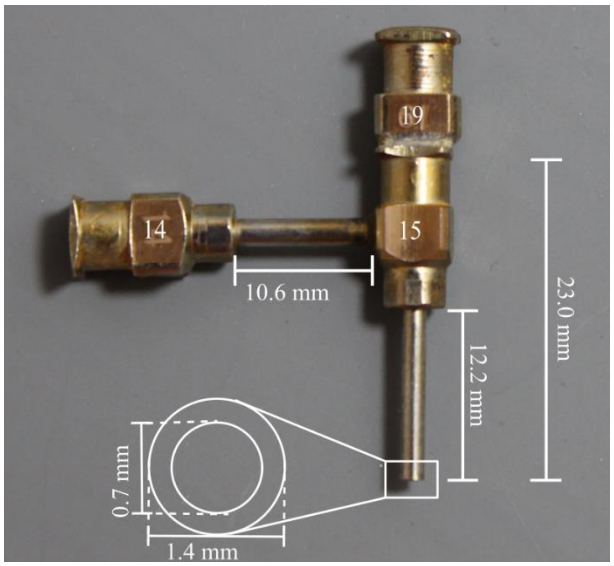

Figure 4.9 Dimensions of the coaxial nozzle

The yield stress of the C1 was 226 Pa (shown by an arrow in Figure 4.10b) which was still below the maximum shear stress (1–2×10^5 Pa) at the wall of the nozzle that will cause the plug flow. On the other hand, C10, the core ink with maximum solid content (~32.4 wt. %) was assessed to elaborate on the rheological response of non-printable inks and how they differ from printable inks in terms of their viscosity. C10, despite exhibiting shear thinning behavior (Figure 4.10a), was not printable due to pressure limitations caused by its high viscosity at rest, which can be attributed to its high solid content (~32.4 wt. %), requiring a significant amount of pressure to initiate flow beyond the printer's capabilities. Additionally, the yield stress of C10 is 4700 Pa—an order of magnitude higher than the yield stress of C1 and S3.

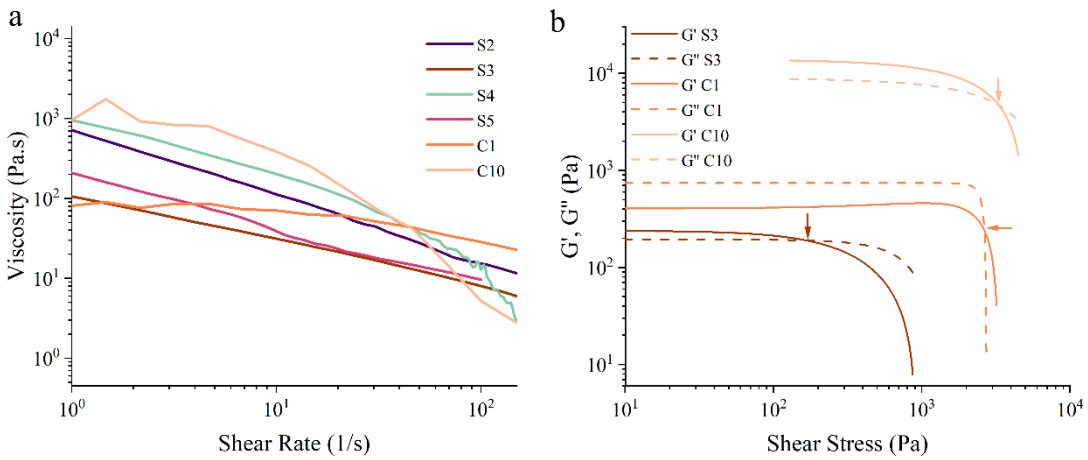

Figure 4.10 Rheological analysis of the core and shell ink formulations a) viscosity as a function of shear rate and b) oscillatory rheological response of inks (Arrows in panel b

show the crossover point of G' and G" which corresponds to the yield stress of the inks.)

G′, G″, yield point, and viscosity at shear rates 1 and 500 s^{-1} were estimated by using data given in Figure 4.10 for chosen inks (Table 4.7).

Table 4.7 Rheological properties of shell and core inks

	G′ – Value in the LVR (Pa)	G″ – Value in the LVR (Pa)	Yield point, τ_f (Pa)	η at (Pa.s)	η at (Pa.s)
S3	240	195	186	106	4
C1	432	740	226	81	1
C10	12600	8320	4700	958	10

Figure 4.11 represents the encapsulation of fertilizer with an MC-ALG shell (S3), the free-flowing nature of core ink (C1) was suppressed by enveloping it in the shell. The difference between core and shell ink is shown in Figure 4.11b. Meshes were also evaluated for the pore and uniformity factors (Soltan et al., 2019). Using Image J, a pore factor that is used to assess how well the pores of the meshes matched with the designed pores, was estimated as 0.998 by using Eq. (4.5) where Pr =1 shows a properly gelled material. The uniformity factor, the ratio of the length of the printed filament to the length of the designed filament, was found as ~1.0 using Eq. (4.6), indicating the filament was uniform.

$$Pr = \frac{\text{Perimeter of the pore}^2}{16 \times \text{area of the pore}} \quad (4.5)$$

$$U = \frac{\text{length of the printed filament}}{\text{theoretical filament length}} \quad (4.6)$$

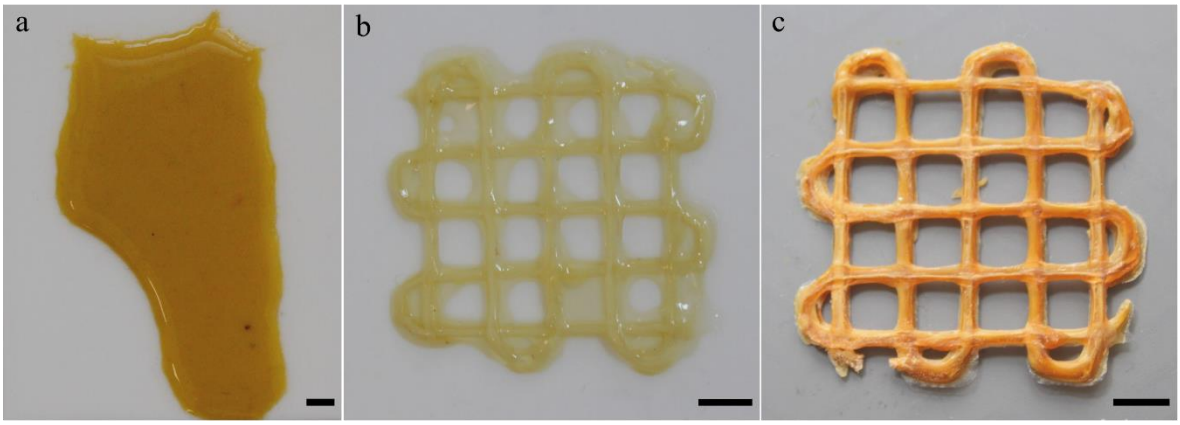

Figure 4.11 a) Core ink (C1) printed with 19-gauge nozzle without a shell encapsulation, b) C1/S3 mesh, the image was taken 5 minutes after printing, c) C1/S3 mesh dried at room temperature for 24 hours the image was taken 1 day after the printing, scale bars represent 5 mm.

An unsuccessful printing example is given in Figure 4.12, when C3 was used as a core ink. The viscosity of ink C3 was insufficient, leading it to spread beyond the intended shell boundaries. This effect was visually demonstrated, highlighting how the low viscosity of ink posed challenges during printing. Due to its low viscosity, the ink kept flowing from the nozzle even after the pressure was discontinued, leading to shell leakage. This continuous flow resulted in the formation of excessively thin fibers, causing uneven fiber thickness within the mesh.

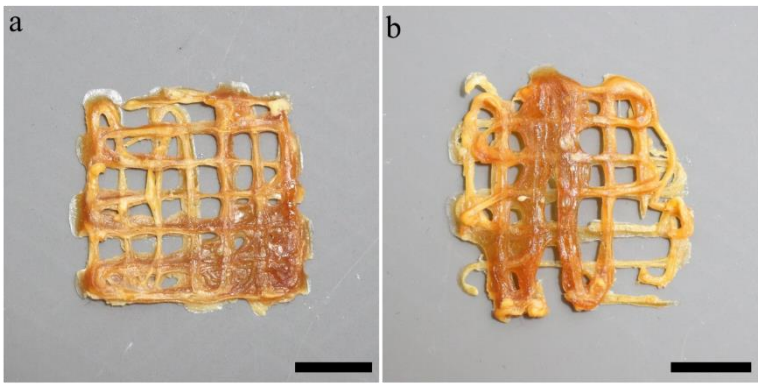

Figure 4.12 Printing with non-optimized fertilizer mixture (C3) with S3 shell, scale bars represent 1 cm.

4.3.2. Mechanical properties

To assess the ease of application and transportation, the rollability and foldability of the shell formulations were evaluated. The foldability of the 2-layered meshes (58 mm × 15

mm) of MC-ALG formulations, S1–6, was investigated visually. Only certain MC and ALG combinations, S3 (MC:ALG of 3; total solid content 6 wt. %) and S5 (MC:ALG of 4; total solid content 6.5 wt. %) folded without being deformed. In addition, S3 exhibited the highest resistance to deformation among all MC-ALG formulations (Figure 4.13a). Along with its compatibility with the core ink, this confirmed the selection of S3 for the shell formulation. The load-bearing tests on S3 meshes with different numbers of layers (2 and 4) and infill percentages (5% and 8%) were carried out. Both 2-layered meshes having 5 and 8% infill safely carried 1715x and 1532x of their own weight (i.e., 200 g); yet, failed to carry 500 g loads (Figure 4.13b,c). 4-layered meshes were able to hold 500 g weights corresponding to 1999x of its weight.

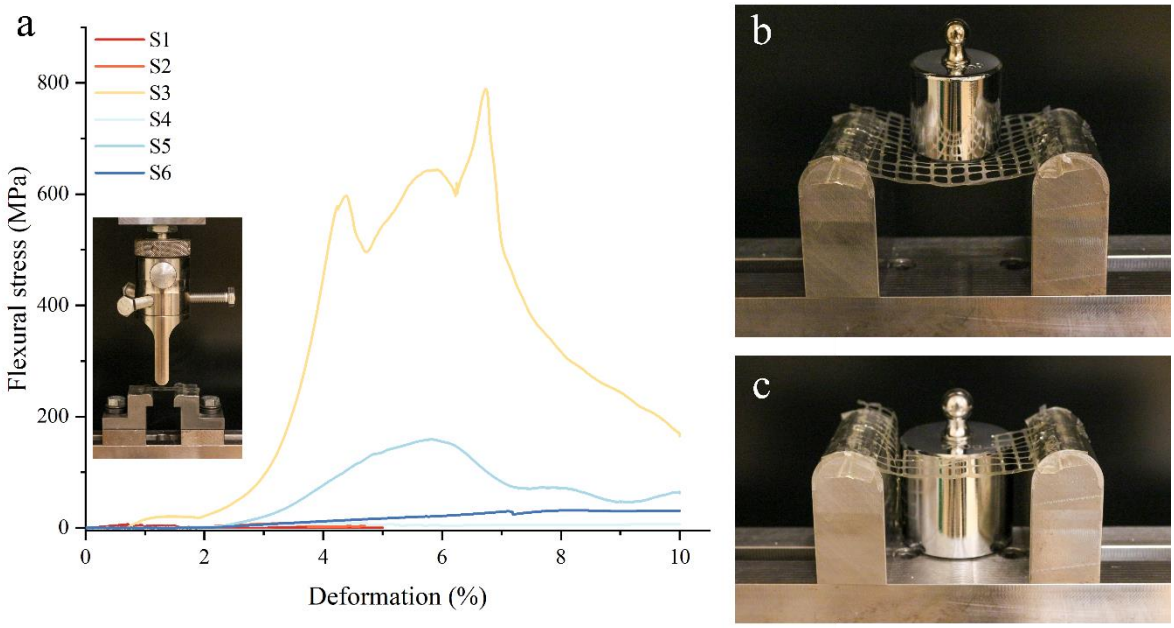

Figure 4.13 a) Flexural stress of ASTM D790 standard meshes and their corresponding percent deformation, the inset of the image shows a sample during a three-point bending test with a 25.4 mm span and 10 kN gripper, b) a 2-layered mesh with 8% infill carrying 1532x of its own weight (a 200 g load), and c) a 2-layered mesh with 8% infill failed to withstand a 500 g load.

In Figure 4.14, although both 2-layered meshes having 5 and 8% infill failed to carry 500 g loads, they safely carried 1715x (200 g) and 1532x (200 g) of their own weight, respectively. The loads between 200 and 500 g were not tested. 4-layered mesh with 8% infill successfully held 500 g, which is 1999x of its weight. The force and pressure exerted by each load were calculated using Eq.(4.7) and Eq. (4.8), reported in Table 4.8.

The exerted force was estimated by using Eq. (4.7),

$$F=m\cdot g \tag{4.7}$$

where m was the mass of the load (kg) applied and g was gravity (g=9.81 m/s^2). The maximum applied pressure (Pa) was found by using Eq. (4.8),

$$P=F/A_p \tag{4.8}$$

where A_p was the basal area of the corresponding calibration weight (m^2).

Table 4.8 Applied loads, their projected areas of the meshes resisting the loads, and corresponding exerted pressure

Load (g)	20	50	100	200	500
F (N)	0.20	0.49	0.98	1.96	4.91
A_p (mm^2)	174	314	488	804	1521
P_{app} (Pa)	1.13×10^3	1.56×10^3	2.01×10^3	2.44×10^3	3.23×10^3

2-layered meshes with 5 and 8% infill could not withstand a pressure of 3.23×10^3 Pa, when 500 g was used as a load, while 4-layered structure with 8% infill was able to hold this weight.

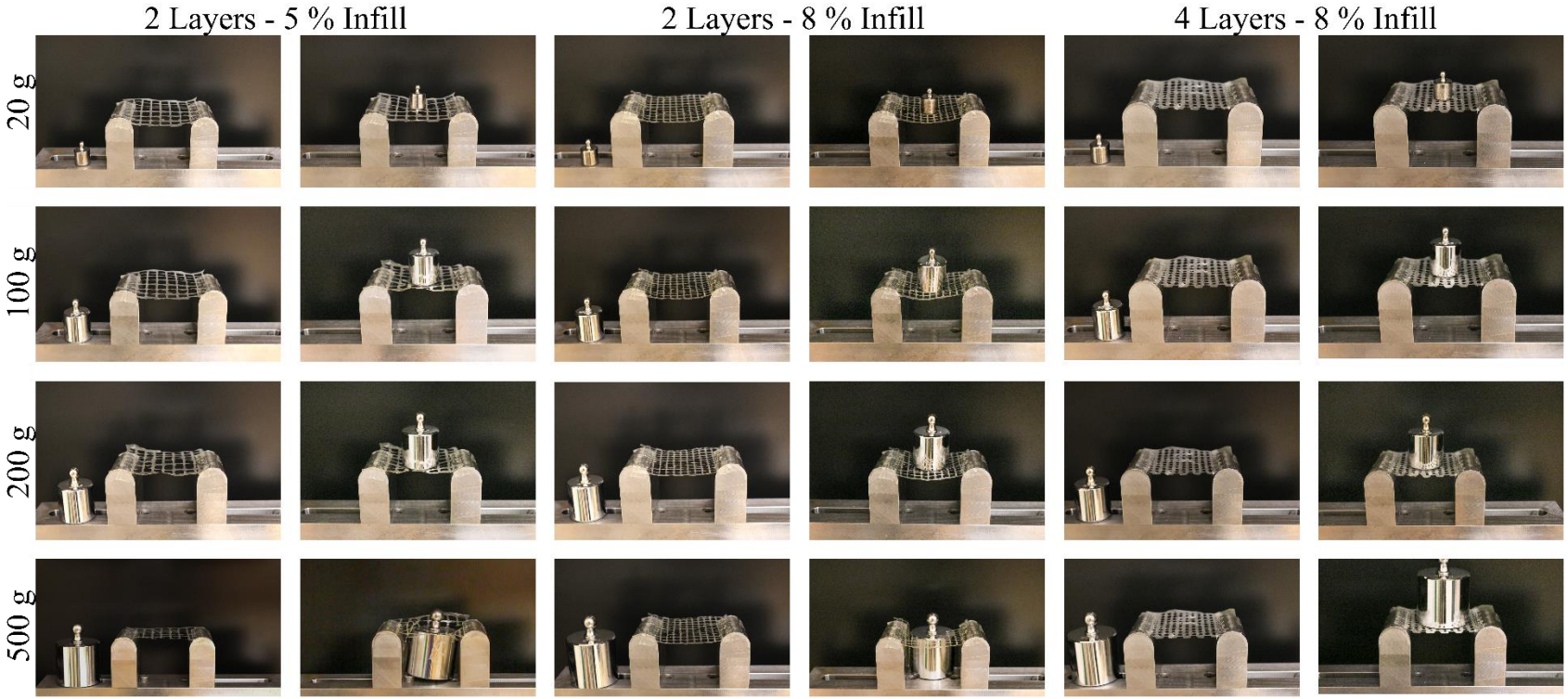

Figure 4.14 Load-bearing capacity of meshes when cast-iron calibration weights with a range of 20–500 g were used.

The infill percentages and number of layers were modeled for tailoring the rollability of the meshes and encapsulating the suggested fertilizer amount needed. Specifically, the number of layers influenced the rollability of the meshes. The rollability of the structure has been assessed by measuring the curvature of the rolled structures (Mary & Brouhard, 2019; Suo et al., 1999). The curvature (κ) of the rod was found as 0.25 mm^{-1}, κ of 2-layered mesh and 4-layered mesh were estimated as 0.26 and 0.17, respectively in Figure 4.15a and b. The details of the κ estimation are provided in Table 4.9. Overall, the 2-layered structure fulfilled the rollability criteria while the 4-layered structure failed the rollability test in Figure 4.15b despite its performance in bearing weights. Figure 4.15c and d depict the occupied volume, highlighting that five rolled meshes (V=2.2 cm^3) occupy a smaller volume in comparison to five stacked meshes (V=3.5 cm^3) on top of each other.

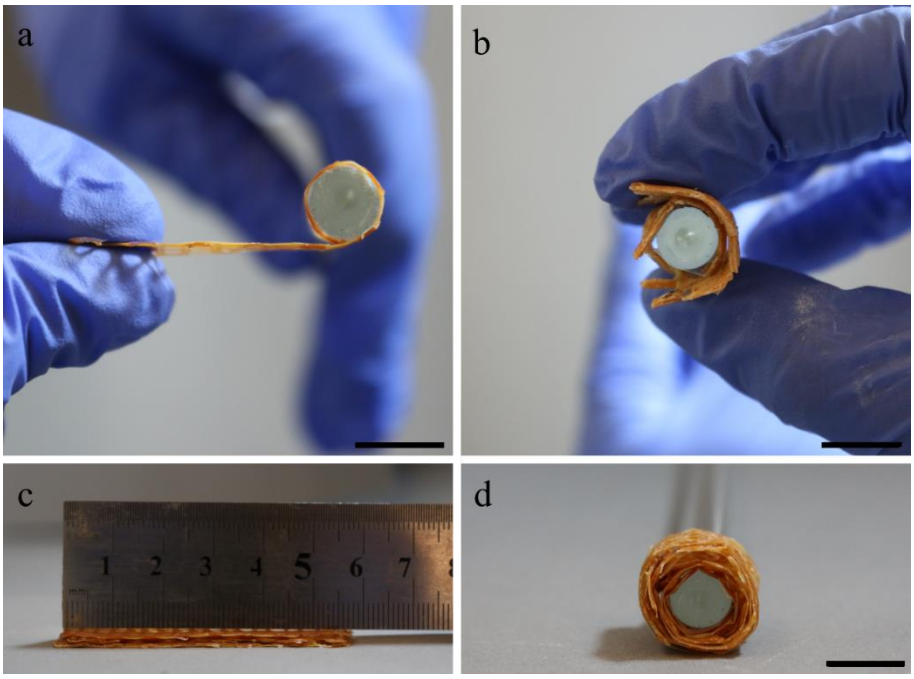

Figure 4.15 a) A 2-layered mesh and b) a 4-layered mesh rolled around a rod with 8 mm diameter, c) the volume that five stacked meshes, and d) five meshes rolled around a rod occupy (Scale bars represent 1 cm.)

Table 4.9 Details of the B-Splines used to estimate the curvature (κ)

Number of layers	Avg. curvature (μm^{-1})	Curve length (μm)	Curvature σ^2 (μm^{-1})	Point curvature (μm^{-1})	Number of points
2	2.56×10^{-4}	2.45×10^{4}	1.27×10^{-4}	0.93×10^{-4}	35
4	1.73×10^{-4}	3.08×10^{4}	1.65×10^{-4}	0.02×10^{-4}	31

4.3.3. Morphology

The optical microscopy and SEM of coaxially printed structures revealed that they preserved their printed shapes after drying in Figure 4.16. Two horizontal lines in Figure 4.16a represent the length of the core and shell filaments, and vertical lines in Figure 4.16b show each layer of the 6-layered mesh. The average diameter of the core filament (0.68±0.02 mm) and shell thickness (0.18±0.02 mm) matched the dimensions of 15/19-gauge nozzle (15G – Inner diameter (ID): 1.40 mm, Outer diameter (OD):1.80 mm; 19G – ID:0.67 mm, OD:1.07 mm, shell thickness: 0.165 mm). Figure 4.16c represents the cross-section of the coaxially printed mesh where the diameter of the core was measured as 0.62±0.04 mm, and the shell as 0.17±0.08 mm, aligning closely with the dimensions observed in optical microscopy.

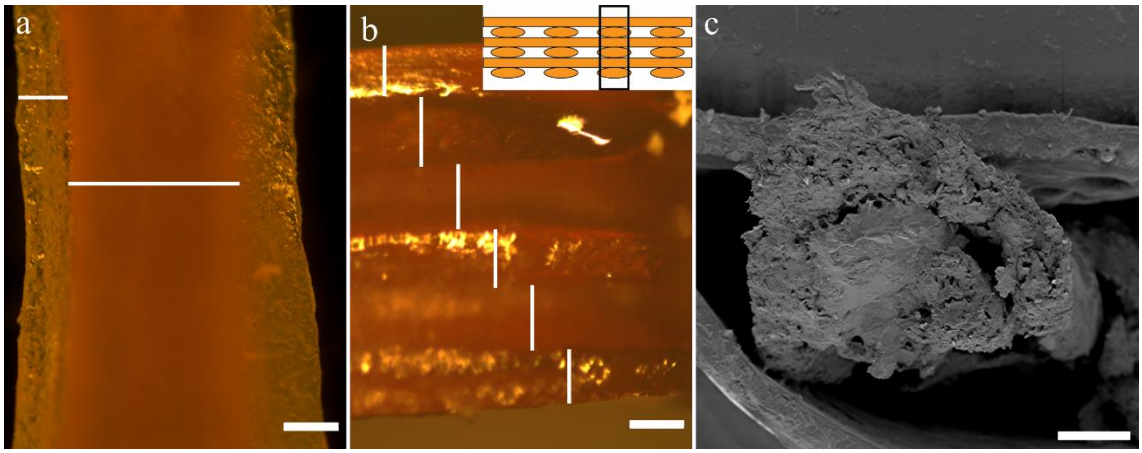

Figure 4.16 a) Dark-field optical image of MC-ALG encapsulated fertilizer top view (5x magnification) and b) side view of mesh layers under episcopic illumination (5x magnification) with schematic, c) SEM cross-section of coaxially printed core-shell mesh, scale bars represent 200 μm.

4.3.4. Degradation and release behavior

The electrical conductivity was saturated at the end of week 1, which was attributed to its rapid dissolution of MC-ALG due to its intrinsically high water solubility (Figure 4.18a). Micronutrients (i.e., Cu^{2+}, Mn^{2+}, Zn^{2+}, B^{3+}, and Fe^{2+}) in commercial-grade multivariant fertilizer play a critical role in the early stages of wheat growth, making it advisable to apply them during the planting phase. Therefore, a week-long dissolution ensures that the essential micronutrients are readily available to support the initial phases of wheat

development, promoting optimal crop health and productivity. After the full dissolution of the MC-ALG shell, degradation was prolonged due to the PEG-HPC carrier system. The weight loss reached 97% at week 8. The Debye length (λ_D) is a fundamental parameter that characterizes the extent of ionic interactions in solution, which in turn affects the electrical conductivity of the medium. An increase in ion concentration due to ion release typically leads to a decrease in the λ_D of the solution, resulting in greater conductivity. The λ_Ds of multivalent ions in solution were estimated as in Table 4.10. The linear increase in electrical conductivity for increasing fertilizer concentrations (Figure 4.17) was ascribed to the predominance of divalent ions compared to the low concentration trivalent ions in the bulk solution. This linear increase also showed that the ions were dissolved homogeneously.

A calibration curve in Figure 4.17 for 0.1–3.4 g/ml of fertilizer in DI water was prepared, and then used in the estimation of the concentration of a solution from the conductivity data and to guide standard solution preparation for ICP-OES.

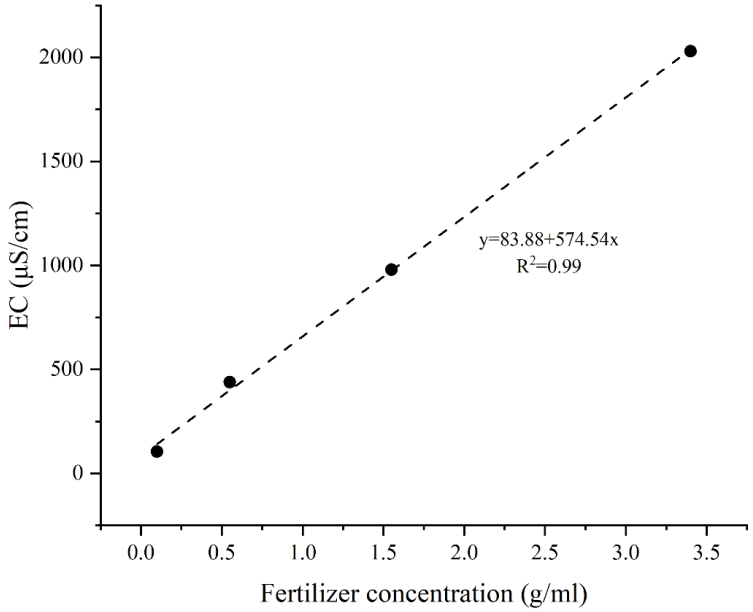

Figure 4.17 Calibration curve for electrical conductivity measurements of fertilizer

For the core-shell mesh structure, characterized by a n of 0.279 and k of 12.3, the model demonstrated a strong correlation with the experimental data (R^2=0.94), suggesting hindered Fickian diffusion as the dominant release mechanism. Fertilizer-polymer matrix mix, with an n value of 0.717 and k value of 2.92, demonstrated anomalous transport with a faster release rate, and the model fit well with the experimental data (R^2=0.90) (Jin et al., 2022; Yoo & Won, 2020). The dissolution of the shell shows a monophasic release

profile consisting of a zero-order release phase (Yoo & Won, 2020). The core-shell system released its fertilizer content ~14 times slower than the monolayer matrix incorporating the same amount of fertilizer.

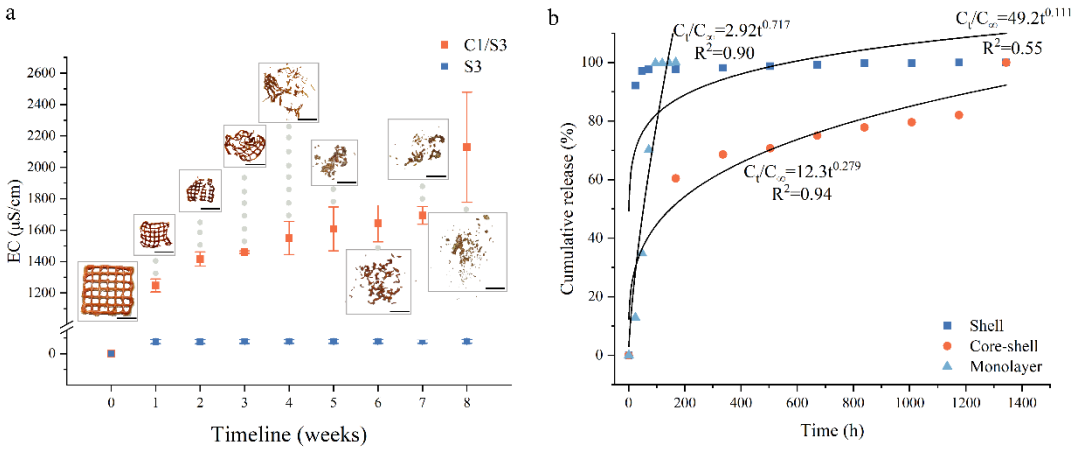

Figure 4.18 a) Changes in electrical conductivity due to the release of ions in 8 weeks, the meshes experienced shrinkage after being dried following the degradation test, scale bars represent 1 cm. b) The fitting curve for dissolution of the shell, ion release from core-shell and monolayered structure

Debye length was calculated by using Eq. (4.9),

$$\delta = \sqrt{\frac{\varepsilon k T}{e^2 \sum_i c_i z_i^2}} \tag{4.9}$$

where ε, k, T, and e are the permittivity of water at room temperature, Boltzmann's constant (J/K), temperature (K), and charge of proton (C), respectively, and taken as constant throughout the calculation. The effective nuclear charge and concentration are z and c (moles/m^3), respectively. They are provided in Table 4.10, by plugging them into Eq. (4.9), an arbitrary value for Debye length was estimated and used for Debye length comparison.

Table 4.10 The effective nuclear charges and concentrations of ions, and their respective arbitrary Debye lengths

Ions	Cu^{2+}	Mn^{2+}	Zn^{2+}	B^{3+}	Fe^{2+}
z	2	2	2	3	2
c (moles/m^3)	0.76×10^{-3}	3.21×10^{-3}	7.06×10^{-3}	3.85×10^{-3}	3.00×10^{-3}
$\delta/\sqrt{\varepsilon kT/e^2}$	18.18	8.82	5.95	5.38	9.12

Figure 4.19 shows the FTIR spectra of C1/S3 mesh before and after the hydrolytic degradation. Since the fertilizer mixture contains sulfate salts of metals (Figure 4.6–Figure 4.8) and the shell is made of MC-ALG hydrogel, the focus was on the SO_4^{2-}

functional group, glycosidic bond, and -OH stretching vibrations to prove the hydrolytic degradation of the mesh. The distinctive peaks appearing at 1460, 1380, 1320, and 950 cm^{-1} in the spectrum of MC have been attributed to the stretching of C-H bonds in CH_2 and CH_3 groups (Oliveira et al., 2015). In addition, the observation of a prominent peak at ~1100 cm^{-1} is indicative of the existence of C-O-C bonds, a distinctive trait of cellulose ethers. The peak for the -OH functional group, which is present at MC, ALG, HPC, and PEG, was observed at 3200–3400 cm^{-1}. The multiple sub-peaks can be assigned to sulfate groups in different bonding states with their molecular neighborhood. The peak around 1100–1,000 cm^{-1} was also broadened due to the strong overlapping of C–O–C vibrations of PEG chains with the sulfate stretching vibrations (Oliveira et al., 2015; Secco, 1988). From week 1 to week 8, the intensity of these peaks decreased, showing that those bonds were hydrolytically broken, and the mesh was degraded, the peaks were shifted up to ~10 cm^{-1}.

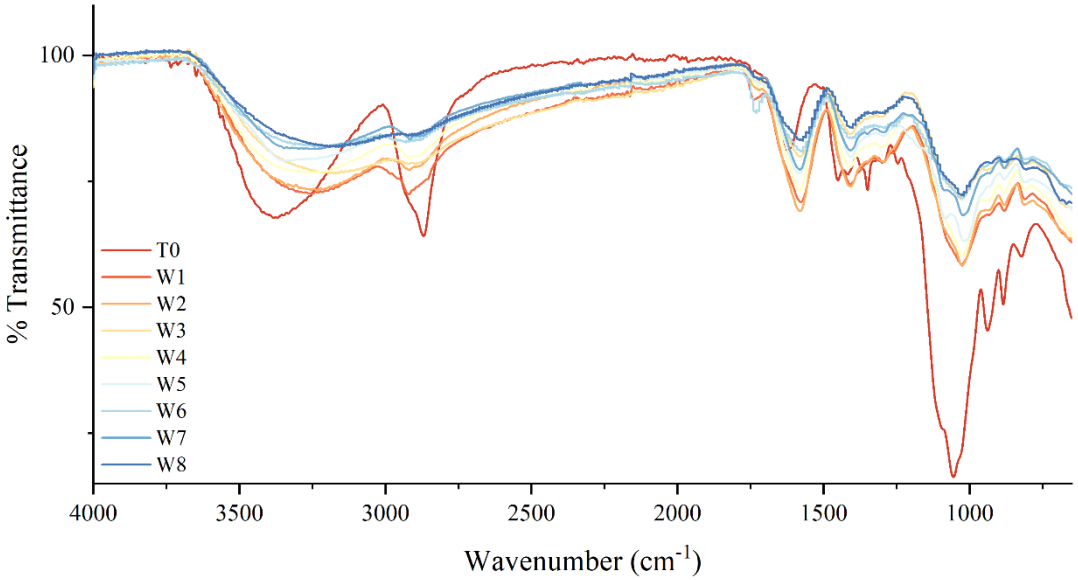

Figure 4.19 FTIR spectra of C1/S3 before and after the hydrolytic degradation (T0 refers to measurement before starting hydrolytic degradation, W stands for week.)

In agreement with the increase in electrical conductivity, ICP-OES showed an increase in ion concentrations from week 1 to week 8 (Figure 4.20).

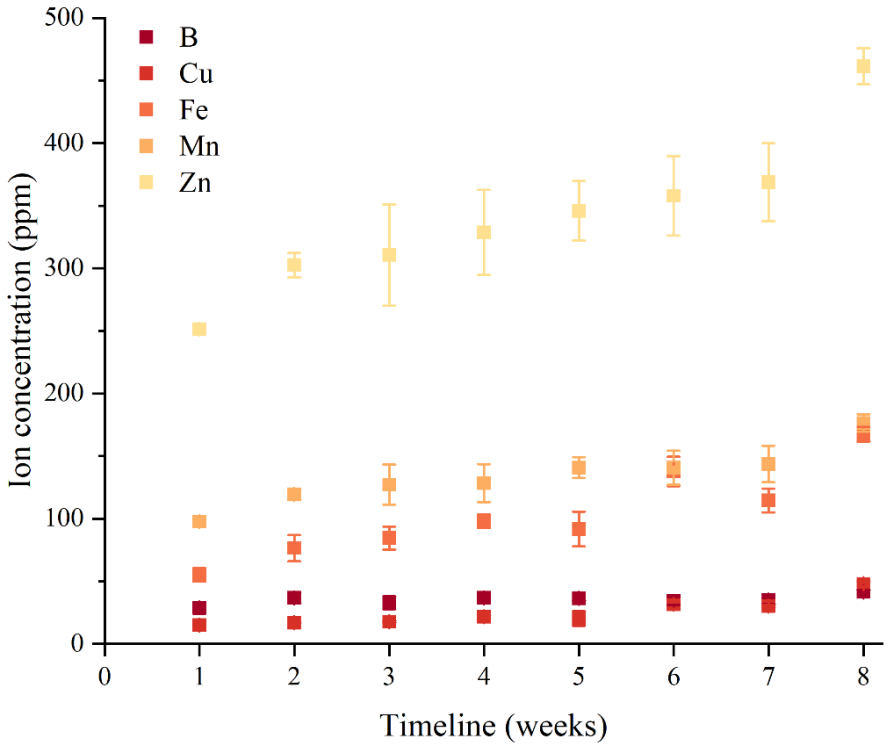

Figure 4.20 Changes in ion concentration in hydrolytic degradation study medium (DI water) over 8 weeks

4.3.5. Assessment of plant growth

A circular mesh designed to fit an 8 cm diameter pot was employed to ensure uniform plant growth across the soil surface (Figure 4.1). Figure 4.21 presents the average maximum shoot length of five Triticum aestivum L. plants per pot. Treatments involving the core-shell mesh structure for fertilizer release demonstrated superior performance over traditional applications, supporting the hypothesis that fertilizer release through the core-shell structure is more effective. Despite having the same fertilizer content, the mesh (Mx) and traditional (Tx) applications resulted in different plant heights (Table 4.11, difference: 9 cm). Among the mesh treatments, Mx, which contained the suggested amount of fertilizer, exhibited the highest shoot length (~ 1.5 times that of Tx), followed by M2x and M0.7x. The treatment with a mesh containing only the shell formulation (Ct2 in Figure 4.21b) had a higher shoot length (~ 1.2 and 1.3 times, respectively) compared to the treatment with only the core formulation without any fertilizer (Ct3 in Figure 4.21c) and no chemicals (Ct1 in Figure 4.21a). This difference suggests that the presence of ALG and MC in the shell contributed to plant growth. On the contrary, M2x, which had twice the suggested amount of fertilizer, also increased plant growth (~1.2 times compared to

T2x). In comparison to traditionally applied fertilizer, the mesh with 30% lower fertilizer content achieved ~1.2 times growth. The increased growth could be attributed to the presence of the polysaccharide matrix as well as the fertilizer. Among traditional applications, Tx had a higher shoot length compared to T2x and T3x, as Tx had the suggested amount of fertilizer, whereas T2x and T3x had excessive amounts. Moreover, the absence of the core-shell structure in these treatments resulted in a rapid release of the fertilizer, which may have led to nutrient loss and reduced efficacy. Overall, the polysaccharide matrix enhanced plant growth compared to the sole application of fertilizer in a traditional manner.

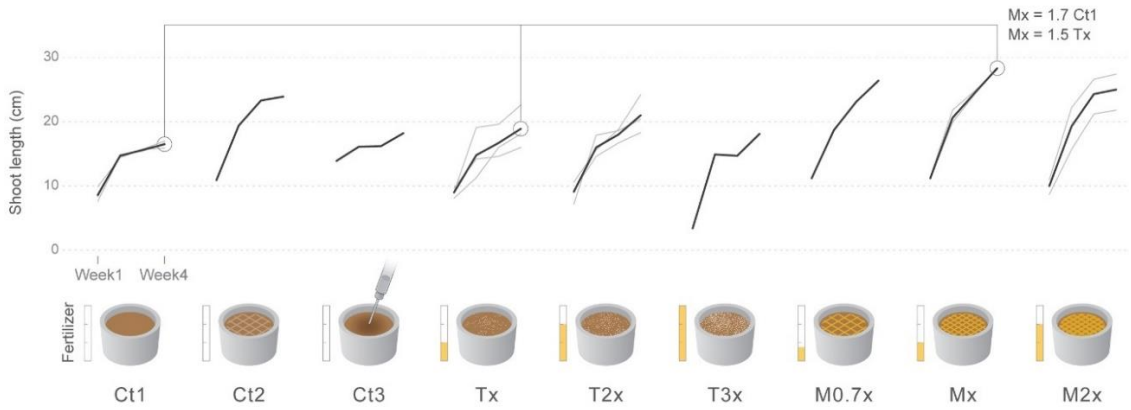

Figure 4.21 Changes in shoot length in 4 weeks under different treatments with a range of fertilizer amounts; black and gray lines represent average shoot length among all pots and for each pot, respectively.

Mean values for plant heights are given in Table 4.11. Data were analyzed by one-way analysis of variance (ANOVA) using OriginPro 2021. Differences between means were compared by using Tukey and tests for equal variance were performed by using “Levene | |” at a 0.05 significance level. Absolute mean differences (Figure 4.22) between treatments were found and compared with the Q critical values obtained from the studentized range Q table, if the difference is greater than the Q critical value, the effects of treatments on plant growth were found to be significantly different. All control treatments (Ct1, Ct2, and Ct3) were found to be nonsignificantly different. The mean heights of plants treated with Mx and Tx were found to be significantly different, indicating that the core-shell mesh structure for the delivery of fertilizer employed in the mesh treatments resulted in higher plant growth compared to the traditional application. M2x and T2x resulted in nonsignificantly different plant heights, this has been attributed

to higher fertilizer content.

Table 4.11 Average plant heights measured at week 4 with different treatments

Treatment	Mean (cm)	Standard deviation
Ct1	16.7	1.2
Ct2	21.0	3.0
Ct3	18.3	0.6
Tx	19.0	3.7
T2x	21.1	3.4
T3x	16.2	1.5
M0.7x	23.7	5.6
Mx	28.4	1.0
M2x	25.1	5.6

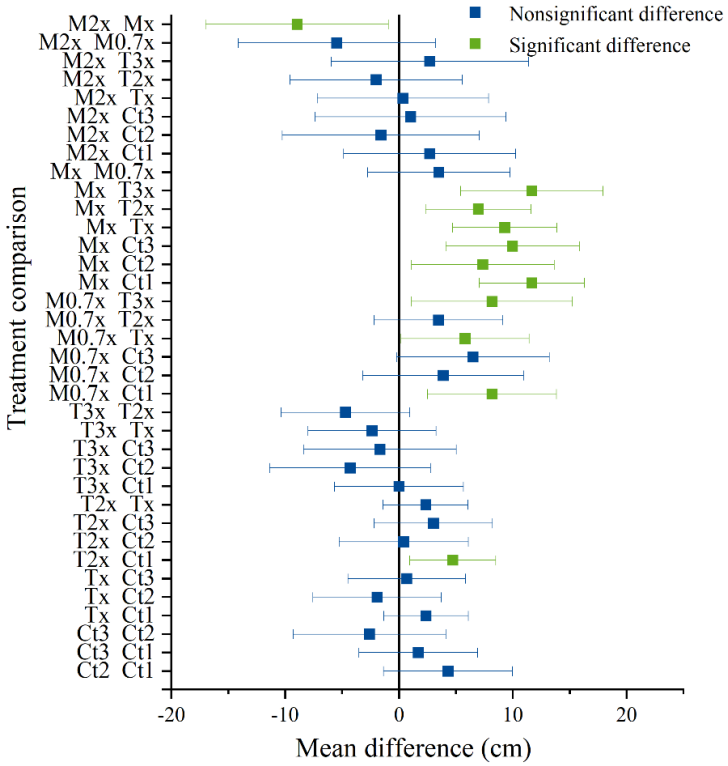

Figure 4.22 Means comparison using Tukey test

4.4.Conclusion

A mechanical fabrication route has been utilized to generate coaxial sub-mm fibers with 100% encapsulation efficiency and optimal fertilizer loading. The core and shell inks for coaxial printing were formulated through rheological and mechanical characterization, leading to the production of robust meshes. The fertilizer was embedded into the polysaccharide matrix and encapsulated with a polysaccharide-based shell of MC-ALG, resulting in wheat shoot growth being boosted by 1.5-fold compared to traditional application methods. The sub-mm fiber size of the mesh ensured a high load-bearing capacity, offering ease in deployment and transportation. In comparison to routes involving chemical synthesis, this zero-waste, organic solvent-free, room temperature method provides a potentially significant decrease in carbon footprint. Further controlled plant growth studies, as well as the incorporation of other agrochemicals, can unlock the prospects of this method for real applications.

Chapter 5

5. CONCLUSION AND FUTURE ASPECTS

In Part I, the processing of alumina and SiAlON ceramics using malleable doughs, have been reported. These approaches offer promising avenues for energy-efficient and cost-effective ceramic manufacturing, with potential applications in various industries. Future research should focus on further assessing their scalability and industrial applicability. Efforts should also be made to evaluate the economic feasibility and environmental impact of these approaches compared to conventional methods, to realize their full potential in ceramic engineering and beyond.

Part II has provided a multifaceted exploration of advancements in agricultural practices, focusing on the development and implementation of fertilizer delivery systems produced via colloidal processing. The discussion on coaxial direct ink writing has highlighted its potential to revolutionize fertilizer release system formulations and deployment, through its ability to fabricate core-shell structures with enhanced encapsulation efficiency. By leveraging this technology, longstanding challenges in agricultural practices, such as excessive chemical use and environmental pollution, while promoting sustainable and efficient nutrient delivery to crops were addressed. Moving forward, future work in this area should focus on further optimizing cDIW techniques for large-scale production and commercialization, as well as exploring polysaccharide-based materials and formulations to enhance the performance and versatility of fertilizer delivery systems. Additionally, continued research into the environmental impact and efficacy of these systems, as well as their integration into existing agricultural practices, will be crucial for realizing their full potential in promoting sustainable agriculture.

BIBLIOGRAPHY

Abbar Khleif, A., & Nemat Hasan Nemah Khniefer, M. (2017). A comparative study of CNC milling cutting path strategies. *Journal for Engineering Sciences (NJES)*, *20*(1), 214–221.

Acosta, M., Wiesner, V. L., Martinez, C. J., Trice, R. W., & Youngblood, J. P. (2013). Effect of polyvinylpyrrolidone additions on the rheology of aqueous, highly loaded alumina suspensions. *Journal of the American Ceramic Society*, *96*(5), 1372–1382. https://doi.org/10.1111/jace.12277

Amaraweera, S. M., Gunathilake, C., Gunawardene, O. H. P., Fernando, N. M. L., Wanninayaka, D. B., Dassanayake, R. S., Rajapaksha, S. M., Manamperi, A., Fernando, C. A. N., Kulatunga, A. K., & Manipura, A. (2021). Development of starch-based materials using current modification techniques and their applications: A review. *Molecules*, *26*(22), 6880. https://doi.org/10.3390/molecules26226880

An, Q., Chen, J., Ming, W., & Chen, M. (2021). Machining of SiC ceramic matrix composites: A review. *Chinese Journal of Aeronautics*, *34*(4), 540–567. https://doi.org/10.1016/j.cja.2020.08.001

Angammana, C. J., & Jayaram, S. H. (2016). Fundamentals of electrospinning and processing technologies. *Particulate Science and Technology*, *34*(1), 72–82. https://doi.org/10.1080/02726351.2015.1043678

ASTM. (2022). *Standard test method for microindentation hardness of materials (ASTM E384-22)*. https://doi.org/10.1520/E0384-22

Atkinson, H. V., & Davies, S. (2000). Fundamental aspects of hot isostatic pressing: An overview. *Metallurgical and Materials Transactions A*, *31*(12), 2981–3000. https://doi.org/10.1007/s11661-000-0078-2

Ayode Otitoju, T., Ugochukwu Okoye, P., Chen, G., Li, Y., Onyeka Okoye, M., & Li, S. (2020). Advanced ceramic components: Materials, fabrication, and applications. *Journal of Industrial and Engineering Chemistry*, *85*, 34–65. https://doi.org/10.1016/j.jiec.2020.02.002

Ben-Nissan, B., Choi, A. H., & Cordingley, R. (2008). 10 - Alumina ceramics. In T. Kokubo (Ed.), *Bioceramics and their clinical applications* (pp. 223–242). Elsevier.

Bennacef, C., Desobry-Banon, S., Probst, L., & Desobry, S. (2023). Alginate core-shell capsules production through coextrusion methods: principles and technologies. *Marine Drugs*, *21*(4), 235. https://doi.org/10.3390/md21040235

Bharathi, V., Anilchandra, A. R., Sangam, S. S., Shreyas, S., & Shankar, S. B. (2021). A review on the challenges in machining of ceramics. *Materials Today: Proceedings*, *46*, 1451–1458. https://doi.org/10.1016/j.matpr.2021.03.019

Bhargava, A. K., & Sharma, C. P. (2011). *Mechanical behaviour and testing of materials*. Prentice Hall India Pvt., Limited. https://books.google.com.tr/books?id=pGwNKvG9GNcC

Bilal, A., Jahan, M., Talamona, D., & Perveen, A. (2018). Electro-Discharge Machining of Ceramics: A Review. *Micromachines*, *10*(1), 10. https://doi.org/10.3390/mi10010010

Bisht, M., Macário, I. P. E., Neves, M. C., Pereira, J. L., Pandey, S., Rogers, R. D., Coutinho, J. A. P., & Ventura, S. P. M. (2021). Enhanced dissolution of chitin using acidic deep eutectic solvents: A sustainable and simple approach to extract chitin from crayfish shell wastes as alternative feedstocks. *ACS Sustainable Chemistry & Engineering*, *9*(48), 16073–16081. https://doi.org/10.1021/acssuschemeng.1c04255

Boberski, C., Hamminger, R., Peuckert, P., Aldinger, F., Dillinger, R., Heinrich, J., & Huber, J. (1989). High-performance silicon nitride materials. *Advanced Materials*, *1*(11), 378–387. https://doi.org/10.1002/adma.19890011104

Bocanegra-Bernal, M. H. (2004). Hot isostatic pressing (HIP) technology and its applications to metals and ceramics. *Journal of Materials Science*, *39*(21), 6399–6420. https://doi.org/10.1023/B:JMSC.0000044878.11441.90

Bouhamed, H., Boufi, S., & Magnin, A. (2009). Alumina interaction with AMPS–MPEG copolymers produced by RAFT polymerization: Stability and rheological behavior. *Journal of Colloid and Interface Science*, *333*(1), 209–220. https://doi.org/10.1016/j.jcis.2009.01.030

Calis Acikbas, N., & Demir, O. (2013). The effect of cation type, intergranular phase amount and cation mole ratios on z value and intergranular phase crystallization of SiAlON ceramics. *Ceramics International*, *39*(3), 3249–3259. https://doi.org/10.1016/j.ceramint.2012.10.013

Calis Acikbas, N., Yurdakul, H., Mandal, H., Kara, F., Turan, S., Kara, A., & Bitterlich, B. (2012). Effect of sintering conditions and heat treatment on the properties,

microstructure and machining performance of α-β-SiAlON ceramics. *Journal of the European Ceramic Society*, *32*(7), 1321–1327. https://doi.org/10.1016/j.jeurceramsoc.2011.11.030

Campos, E. V. R., de Oliveira, J. L., Fraceto, L. F., & Singh, B. (2015). Polysaccharides as safer release systems for agrochemicals. *Agronomy for Sustainable Development*, *35*(1), 47–66. https://doi.org/10.1007/s13593-014-0263-0

Ceylan, A., Suvaci, E., & Mandal, H. (2011). Role of organic additives on non-aqueous tape casting of SiAlON ceramics. *Journal of the European Ceramic Society*, *31*(1–2), 167–173. https://doi.org/10.1016/j.jeurceramsoc.2010.07.034

Chang, D.-Y., & Lin, S.-Y. (2012). Tool wear, hole characteristics, and manufacturing tolerance in alumina ceramic microdrilling process. *Materials and Manufacturing Processes*, *27*(3), 306–313. https://doi.org/10.1080/10426914.2011.577881

Childs, T. H. C. (2000). *Metal machining: Theory and applications*. Arnold. https://books.google.com.tr/books?id=ZawJuCugpCgC

Cother, N. E. (1987). Syalon ceramics — their development and engineering applications. *Materials & Design*, *8*(1), 2–9. https://doi.org/10.1016/0261-3069(87)90053-7

Dabak, T., & Yucel, O. (1987). Modeling of the concentration particle size distribution effects on the rheology of highly concentrated suspensions. *Powder Technology*, *52*(3), 193–206. https://doi.org/10.1016/0032-5910(87)80105-5

Dadhich, P., Srivas, P. K., Mohanty, S., & Dhara, S. (2015). Microfabrication of green ceramics: Contact vs. non-contact machining. *Journal of the European Ceramic Society*, *35*(14), 3909–3916. https://doi.org/10.1016/j.jeurceramsoc.2015.06.025

Dai, L., Cheng, T., Duan, C., Zhao, W., Zhang, W., Zou, X., Aspler, J., & Ni, Y. (2019). 3D printing using plant-derived cellulose and its derivatives: A review. *Carbohydrate Polymers*, *203*, 71–86. https://doi.org/10.1016/j.carbpol.2018.09.027

Davis, R. F. (1991). Hot Isostatic Pressing. In *Concise Encyclopedia of Advanced Ceramic Materials* (pp. 210–215). Elsevier. https://doi.org/10.1016/B978-0-08-034720-2.50061-7

Demarbaix, A., Ducobu, F., Preux, N., Petit, F., & Rivière-Lorphèvre, E. (2020). Green ceramic machining: Influence of the cutting speed and the binder percentage on the Y-TZP behavior. *Journal of Manufacturing and Materials Processing*, *4*(2), 50. https://doi.org/10.3390/jmmp4020050

Demir, A., Birinci, A. U., & Ozturk, H. (2021). Determination of the surface

characteristics of medium density fibreboard processed with CNC machine and optimisation of CNC process parameters by using artificial neural network. *CIRP Journal of Manufacturing Science and Technology*, *35*, 929–942. https://doi.org/10.1016/j.cirpj.2021.10.005

Dhara, S., & Su, B. (2005). Green machining to net shape alumina ceramics prepared using different processing routes. *International Journal of Applied Ceramic Technology*, *2*(3), 262–270. https://doi.org/10.1111/j.1744-7402.2005.02021.x

Doroszkowski, A. (1999). The physical chemistry of dispersion. In *Paint and Surface Coatings* (pp. 198–242). Elsevier. https://doi.org/10.1533/9781855737006.198

El-Amir, A. A. M., El-Maddah, A. A., Ewais, E. M. M., El-Sheikh, S. M., Bayoumi, I. M. I., & Ahmed, Y. M. Z. (2021). Sialon from synthesis to applications: an overview. *Journal of Asian Ceramic Societies*, *9*(4), 1390–1418. https://doi.org/10.1080/21870764.2021.1987613

European Commission Directorate-General for Agriculture and Rural Development. (2019). *Food VI – Feed IV Final Report*. https://agriculture.ec.europa.eu/system/files/2020-01/egtop-final-report-food-vi-feed-iv_en_0.pdf

European Commission Directorate-General For Communication. (2019). *Factsheets on the European Green Deal*. https://commission.europa.eu/publications/factsheets-european-green-deal_en

FAO. (2001). *Global estimates of gaseous emissions of NH3, NO and N2O from agricultural land*. https://www.fao.org/3/Y2780E/y2780e00.htm#P-1_0

FAO. (2019). *World fertilizer trends and outlook to 2022*.

FAO. (2021). *Pesticides use. Global, regional and country trends, 1990–2018*.

Feng, H.-Y., & Menq, C.-H. (1994). The prediction of cutting forces in the ball-end milling process—II. Cut geometry analysis and model verification. *International Journal of Machine Tools and Manufacture*, *34*(5), 711–719. https://doi.org/10.1016/0890-6955(94)90053-1

Ferguson, P., & Rae, A. W. J. M. (1985). Sialons for engineering and refractory applications. In W. Smothers (Ed.), *Proceedings of the conference on raw materials for advanced and engineered ceramics: Ceramic engineering and science proceedings* (pp. 1296–1304). https://doi.org/10.1002/9780470320297.ch12

Food and Agriculture Organization of the United Nations. (2018). *Report of the 50th*

session of the codex committee on food additives. https://doi.org/https://www.fao.org/fao-who-codexalimentarius/sh-proxy/en/?lnk=1&url=https%253A%252F%252Fworkspace.fao.org%252Fsites%252Fcodex%252FMeetings%252FCX-711-50%252FReport%252FREP18_FAe.pdf

Foroughi, F., Rezvani Ghomi, E., Morshedi Dehaghi, F., Borayek, R., & Ramakrishna, S. (2021). A review on the life cycle assessment of cellulose: From properties to the potential of making it a low carbon material. *Materials*, *14*(4), 714. https://doi.org/10.3390/ma14040714

Furberg, A., Arvidsson, R., & Molander, S. (2019). Environmental life cycle assessment of cemented carbide (WC-Co) production. *Journal of Cleaner Production*, *209*, 1126–1138. https://doi.org/10.1016/j.jclepro.2018.10.272

Furusawa, K., Shou, Z., & Nagahashi, N. (1992). Polymer adsorption on fine particles; the effects of particle size and its stability. *Colloid & Polymer Science*, *270*(3), 212–218. https://doi.org/10.1007/BF00655472

Ganesh, I., & Sundararajan, G. (2010). Hydrolysis-induced aqueous gelcasting of β-SiAlON–SiO2 ceramic composites: The effect of AlN additive. *Journal of the American Ceramic Society*, *93*(10), 3180–3189. https://doi.org/10.1111/j.1551-2916.2010.03885.x

Gao, Y., Liu, Y., Qin, X., Guo, Z., Li, D., Li, C., Wan, H., Zhu, F., Li, J., Zhang, Z., & He, S. (2021). Dual stimuli-responsive fungicide carrier based on hollow mesoporous silica/hydroxypropyl cellulose hybrid nanoparticles. *Journal of Hazardous Materials*, *414*, 125513. https://doi.org/10.1016/j.jhazmat.2021.125513

Garduque, R. G., Gococo, B. J., Yu, C. A., Nalzaro, P. J., & Tumolva, T. (2020). Synthesis and characterization of sodium carboxymethyl cellulose/sodium alginate/hydroxypropyl cellulose hydrogel for agricultural water storage and controlled nutrient release. *Solid State Phenomena*, *304*, 51–57. https://doi.org/10.4028/www.scientific.net/SSP.304.51

Gediga, J., Morfino, A., Finkbeiner, M., Schulz, M., & Harlow, K. (2019). Life cycle assessment of zircon sand. *The International Journal of Life Cycle Assessment*, *24*(11), 1976–1984. https://doi.org/10.1007/s11367-019-01619-5

German, R. M. (2016). Sintering trajectories: Description on how density, surface area, and grain size change. *JOM*, *68*(3), 878–884. https://doi.org/10.1007/s11837-015-1795-8

Gonçalves Júnior, M., de Angelo Sanchez, L. E., França, T. V., Fortulan, C. A., da Silva, R. H. L., & Foschini, C. R. (2019). Analysis of the tool nose radius influence in the machining of a green ceramic material. *The International Journal of Advanced Manufacturing Technology*, *105*(7–8), 3117–3125. https://doi.org/10.1007/s00170-019-04430-6

Gurney, J. W., Unger, J. M., Dorby, C. A., Mitby, J. K., & Von Essen, S. G. (1991). Agricultural disorders of the lung. *RadioGraphics*, *11*(4), 625–634. https://doi.org/10.1148/radiographics.11.4.1887117

Hack, B., Egger, H., Uhlemann, J., Henriet, M., Wirth, W., Vermeer, A. W. P., & Duff, D. G. (2012). Advanced agrochemical formulations through encapsulation strategies? *Chemie Ingenieur Technik*, *84*(3), 223–234. https://doi.org/10.1002/cite.201100212

Hafidh Obaeed, N. (2019). Study the effect of process parameters of CNC milling surface generation using Al-alloy 7024. *DJES*, *12*(3), 103–112. https://doi.org/10.24237/djes.2019.12312

He, Z., & Ma, J. (2000). Grain-growth rate constant of hot-pressed alumina ceramics. *Materials Letters*, *44*(1), 14–18. https://doi.org/10.1016/S0167-577X(99)00289-X

Heimann, R. B. (2010). Classic and advanced ceramics: From fundamentals to applications. In *Classic and Advanced Ceramics: From Fundamentals to Applications*. https://doi.org/10.1002/9783527630172

Herrmann, M., Höhn, S., & Bales, A. (2012). Kinetics of rare earth incorporation and its role in densification and microstructure formation of α-Sialon. *Journal of the European Ceramic Society*, *32*(7), 1313–1319. https://doi.org/10.1016/j.jeurceramsoc.2011.05.026

Heunisch, A., Dellert, A., & Roosen, A. (2010). Effect of powder, binder and process parameters on anisotropic shrinkage in tape cast ceramic products. *Journal of the European Ceramic Society*, *30*(16), 3397–3406. https://doi.org/10.1016/j.jeurceramsoc.2010.08.012

Hussey, R. J., & Wilson, J. (2012). *Advanced technical ceramics directory and databook*. Springer US. https://books.google.com.tr/books?id=hYrhBwAAQBAJ

Ibáñez-Forés, V., Bovea, M.-D., & Simó, A. (2011). Life cycle assessment of ceramic tiles. Environmental and statistical analysis. *The International Journal of Life Cycle Assessment*, *16*(9), 916–928. https://doi.org/10.1007/s11367-011-0322-6

International Fertilizer Association. (2021). *Public summary: Medium-term fertilizer outlook 2021 – 2025* (Issue August).

Jack, K. H. (1976). Sialons and related nitrogen ceramics. *Journal of Materials Science*, *11*(6), 1135–1158. https://doi.org/10.1007/BF02396649

Jack, K. H. (1986). Sialons: A study in materials development. In *Non-Oxide Technical and Engineering Ceramics* (pp. 1–30). Springer Netherlands. https://doi.org/10.1007/978-94-009-3423-8_1

Janssen, R., Scheppokat, S., & Claussen, N. (2008). Tailor-made ceramic-based components—Advantages by reactive processing and advanced shaping techniques. *Journal of the European Ceramic Society*, *28*(7), 1369–1379. https://doi.org/10.1016/j.jeurceramsoc.2007.12.022

Javazmi, L., Young, A., Ash, G. J., & Low, T. (2021). Kinetics of slow release of nitrogen fertiliser from multi-layered nanofibrous structures. *Scientific Reports*, *11*(1), 4871. https://doi.org/10.1038/s41598-021-84460-x

Jin, X., Wei, C., Wu, C., & Zhang, W. (2022). Customized hydrogel for sustained release of highly water-soluble drugs. *ACS Omega*, *7*(10), 8493–8497. https://doi.org/10.1021/acsomega.1c06106

Johansson, D., Lindvall, R., Windmark, C., M'Saoubi, R., Can, A., Bushlya, V., & Ståhl, J.-E. (2019). Assessment of metal cutting tools using cost performance ratio and tool life analyses. *Procedia Manufacturing*, *38*, 816–823. https://doi.org/10.1016/j.promfg.2020.01.114

Juneja, B. L. (2003). *Fundamentals of metal cutting and machine tools*. New Age International Publishers. https://books.google.com.tr/books?id=r8paflRca90C

Kamani, K., Donley, G. J., & Rogers, S. A. (2021). Unification of the rheological physics of yield stress fluids. *Physical Review Letters*, *126*(21), 218002. https://doi.org/10.1103/PhysRevLett.126.218002

Kastyl, J., Chlup, Z., Stastny, P., & Trunec, M. (2020). Machinability and properties of zirconia ceramics prepared by gelcasting method. *Advances in Applied Ceramics*, *119*(5–6), 252–260. https://doi.org/10.1080/17436753.2019.1675402

Khan, U. A., Hussain, A., Shah, M., Shuaib, M., & Qayyum, F. (2016). Investigation of mechanical properties based on grain growth and microstructure evolution of alumina ceramics during two step sintering process. *IOP Conference Series: Materials Science and Engineering*, *146*, 012046. https://doi.org/10.1088/1757-

899X/146/1/012046

Khorasani, A. Mahyar, Yazdi, M. R. S., & Safizadeh, M. S. (2012). Analysis of machining parameters effects on surface roughness: a review. *International Journal of Computational Materials Science and Surface Engineering*, *5*(1), 68. https://doi.org/10.1504/IJCMSSE.2012.049055

Khorasani, Amir Mahyar, Gibson, I., Goldberg, M., Nomani, J., & Littlefair, G. (2016). Machinability of metallic and ceramic biomaterials: A review. *Science of Advanced Materials*, *8*(8), 1491–1511. https://doi.org/10.1166/sam.2016.2783

Kim, J., Choi, Y., Gal, C. W., Park, H., Yoon, S., & Yun, H. (2022). Effect of dispersants on structural integrity of 3D printed ceramics. *International Journal of Applied Ceramic Technology*, *19*(2), 968–978. https://doi.org/10.1111/ijac.13965

Kim, S., Hyun, K., Moon, J. Y., Clasen, C., & Ahn, K. H. (2015). Depletion stabilization in nanoparticle–polymer suspensions: Multi-length-scale analysis of microstructure. *Langmuir*, *31*(6), 1892–1900. https://doi.org/10.1021/la504578x

Krnel, K., & Kosmač, T. (2000). Reactivity of aluminum nitride powder in dilute inorganic acids. *Journal of the American Ceramic Society*, *83*(6), 1375–1378. https://doi.org/10.1111/j.1151-2916.2000.tb01396.x

Krnel, K., & Kosmač, T. (2001). Protection of AlN powder against hydrolysis using aluminum dihydrogen phosphate. *Journal of the European Ceramic Society*, *21*(10–11), 2075–2079. https://doi.org/10.1016/S0955-2219(01)00175-3

Krstic, Z., & Krstic, V. D. (2012). Silicon nitride: the engineering material of the future. *Journal of Materials Science*, *47*(2), 535–552. https://doi.org/10.1007/s10853-011-5942-5

Kulkarni, H., & Dabhade, V. V. (2019). Green machining of powder-metallurgy-steels (PMS): An overview. *Journal of Manufacturing Processes*, *44*, 1–18. https://doi.org/10.1016/j.jmapro.2019.05.009

Kumar, R., Calis Acikbas, N., Kara, F., Mandal, H., & Basu, B. (2009). Microstructure–mechanical properties–wear resistance relationship of SiAlON ceramics. *Metallurgical and Materials Transactions A*, *40*(10), 2319–2332. https://doi.org/10.1007/s11661-009-9930-1

Laarz, E., Zhmud, B. V., & Bergström, L. (2000). Dissolution and deagglomeration of silicon nitride in aqueous medium. *Journal of the American Ceramic Society*, *83*(10), 2394–2400. https://doi.org/10.1111/j.1151-2916.2000.tb01567.x

Lange, F. F. (1980). Silicon nitride polyphase systems: fabrication, microstructure, and properties. *International Metals Reviews*, *25*(1), 1–20. https://doi.org/10.1179/imtr.1980.25.1.1

Lawrencia, D., Wong, S. K., Low, D. Y. S., Goh, B. H., Goh, J. K., Ruktanonchai, U. R., Soottitantawat, A., Lee, L. H., & Tang, S. Y. (2021). Controlled release fertilizers: A review on coating materials and mechanism of release. *Plants*, *10*(2), 238. https://doi.org/10.3390/plants10020238

Lee, K., Chen, C., Hsiang, H., Yen, F., & Huang, C. (2019). Fully sintered alumina with a higher Vickers hardness prepared using a gel-casting process. *International Journal of Applied Ceramic Technology*, *16*(4), 1493–1500. https://doi.org/10.1111/ijac.13218

Leo, S., Tallon, C., Stone, N., & Franks, G. V. (2014). Near-net-shaping methods for ceramic elements of (Body) armor systems. *Journal of the American Ceramic Society*, *97*(10), 3013–3033. https://doi.org/10.1111/jace.13192

Li, G., Hu, L., Liu, J., Huang, J., Yuan, C., Takaki, K., & Hu, Y. (2022). A review on 3D printable food materials: types and development trends. *International Journal of Food Science & Technology*, *57*(1), 164–172. https://doi.org/10.1111/ijfs.15391

Liu, Y., Deng, J., Wang, W., Duan, R., Meng, R., Ge, D., & Li, X. (2018). Effect of texture parameters on cutting performance of flank-faced textured carbide tools in dry cutting of green Al2O3 ceramics. *Ceramics International*, *44*(11), 13205–13217. https://doi.org/10.1016/j.ceramint.2018.04.146

Liu, Y., Deng, J., Wu, F., Duan, R., Zhang, X., & Hou, Y. (2017). Wear resistance of carbide tools with textured flank-face in dry cutting of green alumina ceramics. *Wear*, *372–373*, 91–103. https://doi.org/10.1016/j.wear.2016.12.001

Lu, S.-H., Liu, G., Ma, Y.-F., & Li, F. (2010). Synthesis and application of a new vinyl copolymer superplasticizer. *Journal of Applied Polymer Science*, NA-NA. https://doi.org/10.1002/app.31984

Ma, H., Dong, Z., Wang, Z., Yang, F., Kang, R., & Bao, Y. (2024). Tool wear in cutting carbon fiber reinforced polymer/ceramic matrix composites: A review. *Composite Structures*, *337*, 118033. https://doi.org/10.1016/j.compstruct.2024.118033

Ma, J., Xie, Z., Miao, H., Huang, Y., Cheng, Y., & Yang, W. (2003). Gelcasting of alumina ceramics in the mixed acrylamide and polyacrylamide systems. *Journal of the European Ceramic Society*, *23*(13), 2273–2279. https://doi.org/10.1016/S0955-

2219(03)00041-4

Ma, Y., Preveniou, A., Kladis, A., & Pettersen, J. B. (2022). Circular economy and life cycle assessment of alumina production: Simulation-based comparison of Pedersen and Bayer processes. *Journal of Cleaner Production*, *366*, 132807. https://doi.org/10.1016/j.jclepro.2022.132807

Malafatti, J. O. D., de Oliveira Ruellas, T. M., Sciena, C. R., & Paris, E. C. (2023). PLA/starch biodegradable fibers obtained by the electrospinning method for micronutrient mineral release. *AIMS Materials Science*, *10*(2), 200–212. https://doi.org/10.3934/matersci.2023011

Mandal, H., Kara, F., Kara, A., & Turan, S. (2006). *Doped alpha-beta sialon ceramics* (Patent No. US 7,064,095 B2). United States Patent.

Mary, H., & Brouhard, G. J. (2019). Kappa (K): Analysis of curvature in biological image data using B-splines. *BioRxiv*, 852772. https://doi.org/10.1101/852772

Meshalkin, V. P., & Belyakov, A. V. (2020). Methods used for the compaction and molding of ceramic matrix composites reinforced with carbon nanotubes. *Processes*, *8*(8), 1004. https://doi.org/10.3390/pr8081004

Micallef, C., Zhuk, Y., & Aria, A. I. (2020). Recent progress in precision machining and surface finishing of tungsten carbide hard composite coatings. *Coatings*, *10*(8), 731. https://doi.org/10.3390/coatings10080731

Mignon, A., De Belie, N., Dubruel, P., & Van Vlierberghe, S. (2019). Superabsorbent polymers: A review on the characteristics and applications of synthetic, polysaccharide-based, semi-synthetic and 'smart' derivatives. *European Polymer Journal*, *117*, 165–178. https://doi.org/10.1016/j.eurpolymj.2019.04.054

Mohammed, A., Ward, K., Lee, K.-Y., & Dupont, V. (2023). The environmental impact and economic feasibility assessment of composite calcium alginate bioplastics derived from Sargassum. *Green Chemistry*, *25*(14), 5501–5516. https://doi.org/10.1039/D3GC01019H

Mohanty, S., Das, B., & Dhara, S. (2013). Poly(maleic acid) – A novel dispersant for aqueous alumina slurry. *Journal of Asian Ceramic Societies*, *1*(2), 184–190. https://doi.org/10.1016/j.jascer.2013.05.005

Mohanty, S., Rameshbabu, A. P., Mandal, S., Su, B., & Dhara, S. (2013). Critical issues in near net shape forming via green machining of ceramics: A case study of alumina dental crown. *Journal of Asian Ceramic Societies*, *1*(3), 274–281.

https://doi.org/10.1016/j.jascer.2013.06.005

Nieto, M. I., Santacruz, I., & Moreno, R. (2014). Shaping of dense advanced ceramics and coatings by gelation of polysaccharides. *Advanced Engineering Materials*, *16*(6), 637–654. https://doi.org/10.1002/adem.201400076

Niihara, K., Morena, R., & Hasselman, D. P. H. (1982). Evaluation of KIc of brittle solids by the indentation method with low crack-to-indent ratios. *Journal of Materials Science Letters*, *1*(1), 13–16. https://doi.org/10.1007/BF00724706

Nooeaid, P., Chuysinuan, P., Pitakdantham, W., Aryuwananon, D., Techasakul, S., & Dechtrirat, D. (2021). Eco-friendly polyvinyl alcohol/polylactic acid core/shell structured fibers as controlled-release fertilizers for sustainable agriculture. *Journal of Polymers and the Environment*, *29*(2), 552–564. https://doi.org/10.1007/s10924-020-01902-9

Oliveira, R. L., Vieira, J. G., Barud, H. S., Assunção, R. M. N., Rodrigues Filho, G., Ribeiro, S. J. L., & Messadeqq, Y. (2015). Synthesis and characterization of methylcellulose produced from bacterial cellulose under heterogeneous condition. *Journal of the Brazilian Chemical Society*. https://doi.org/10.5935/0103-5053.20150163

Özcan, S., Açıkbaş, G., Özbay, N., & Açıkbaş, N. Ç. (2017). The effect of silicon nitride powder characteristics on SiAlON microstructures, densification and phase assemblage. *Ceramics International*, *43*(13), 10057–10065. https://doi.org/10.1016/j.ceramint.2017.05.024

Ozhan, A. B., Demir, G., & Akbulut, O. (2023). Local optimization of low power laser machining of MgO at the green state enables cost- and energy-efficient benchtop fabrication. *Journal of Manufacturing Processes*, *98*, 206–215. https://doi.org/10.1016/j.jmapro.2023.04.049

Pabla, B. S., & Adithan, M. (1994). *CNC machines* (pp. 1–107). New Age International.

Pascoli, M., Lopes-Oliveira, P. J., Fraceto, L. F., Seabra, A. B., & Oliveira, H. C. (2018). State of the art of polymeric nanoparticles as carrier systems with agricultural applications: a mini review. *Energy, Ecology and Environment*, *3*(3), 137–148. https://doi.org/10.1007/s40974-018-0090-2

Piculell, L., & Lindman, B. (1992a). Association and segregation in aqueous polymer/polymer, polymer/surfactant, and surfactant/surfactant mixtures: similarities and differences. *Advances in Colloid and Interface Science*, *41*, 149–

178. https://doi.org/10.1016/0001-8686(92)80011

Piculell, L., & Lindman, B. (1992b). Association and segregation in aqueous polymer/polymer, polymer/surfactant, and surfactant/surfactant mixtures: Similarities and differences. *Advances in Colloid and Interface Science*, *41*, 149–178. https://doi.org/10.1016/0001-8686(92)80011-L

Prabhakaran, K., Ananthakumar, S., & Pavithran, C. (1999). Gel casting of alumina using boehmite as a binder. *Journal of the European Ceramic Society*, *19*(16), 2875–2881. https://doi.org/10.1016/S0955-2219(99)00075-8

Qiao, D., Liu, H., Yu, L., Bao, X., Simon, G. P., Petinakis, E., & Chen, L. (2016). Preparation and characterization of slow-release fertilizer encapsulated by starch-based superabsorbent polymer. *Carbohydrate Polymers*, *147*, 146–154. https://doi.org/10.1016/j.carbpol.2016.04.010

Raj, S. S., Michailovich, K. A., Subramanian, K., Sathiamoorthyi, S., & Kandasamy, K. T. (2021). Philosophy of selecting ASTM standards for mechanical characterization of polymers and polymer composites. *Materiale Plastice*, *58*(3), 247–256. https://doi.org/10.37358/MP.21.3.5523

Rathore, P., & Schiffman, J. D. (2021). Beyond the single-nozzle: Coaxial electrospinning enables innovative nanofiber chemistries, geometries, and applications. *ACS Applied Materials & Interfaces*, *13*(1), 48–66. https://doi.org/10.1021/acsami.0c17706

Richerson, D. W., & Stephan, P. M. (1991). Evolution of applications of Si3N4-based materials. *Materials Science Forum*, *47*, 282–0. https://doi.org/10.4028/www.scientific.net/MSF.47.282

Riedel, R., Ionescu, E., & Chen, I. -We. (2008). Modern trends in advanced ceramics. In *Ceramics Science and Technology* (pp. 1–38). Wiley. https://doi.org/10.1002/9783527631926.ch1

Rizzo, A., Goel, S., Luisa Grilli, M., Iglesias, R., Jaworska, L., Lapkovskis, V., Novak, P., Postolnyi, B. O., & Valerini, D. (2020). The critical raw materials in cutting tools for machining applications: A review. *Materials*, *13*(6), 1377. https://doi.org/10.3390/ma13061377

Rong, L., Chen, X., Shen, M., Yang, J., Qi, X., Li, Y., & Xie, J. (2023). The application of 3D printing technology on starch-based product: A review. *Trends in Food Science & Technology*, *134*, 149–161. https://doi.org/10.1016/j.tifs.2023.02.015

Rosenflanz, A. (1999). Silicon nitride and sialon ceramics. *Current Opinion in Solid State and Materials Science*, *4*(5), 453–459. https://doi.org/10.1016/S1359-0286(00)00004-8

Salami, O. T., & Plank, J. (2012). Synthesis, effectiveness, and working mechanism of humic acid-{sodium 2-acrylamido-2-methylpropane sulfonate -co - N,N -dimethyl acrylamide- co -acrylic acid} graft copolymer as high-temperature fluid loss additive in oil well cementing. *Journal of Applied Polymer Science*, *126*(4), 1449–1460. https://doi.org/10.1002/app.36725

Scaffaro, R., Settanni, L., & Gulino, E. F. (2023). Release profiles of carvacrol or chlorhexidine of PLA/graphene nanoplatelets membranes prepared using electrospinning and solution blow spinning: A comparative study. *Molecules*, *28*(4), 1967. https://doi.org/10.3390/molecules28041967

Schneider, C. A., Rasband, W. S., & Eliceiri, K. W. (2012). NIH Image to ImageJ: 25 years of image analysis. *Nature Methods*, *9*(7), 671–675. https://doi.org/10.1038/nmeth.2089

Schwarz, S., Buchhammer, H.-M., Lunkwitz, K., & Jacobasch, H.-J. (1998). Polyelectrolyte adsorption on charged surfaces: study by electrokinetic measurements. *Colloids and Surfaces A: Physicochemical and Engineering Aspects*, *140*(1–3), 377–384. https://doi.org/10.1016/S0927-7757(97)00294-X

Secco, E. A. (1988). Spectroscopic properties of SO4 (and OH) in different molecular and crystalline environments. I. Infrared spectra of Cu4(OH)6SO4, Cu4(OH)4OSO4, and Cu3(OH)4SO4. *Canadian Journal of Chemistry*, *4*.

Seesala, V. S., & Dhara, S. (2021). Nature inspired dough processing of alumina-zirconia composites: Rheology, plasticity and weibull analysis towards net shaping. *Journal of the European Ceramic Society*, *41*(14), 7170–7181. https://doi.org/10.1016/j.jeurceramsoc.2021.07.019

Seesala, V. S., Rajasekaran, R., Dutta, A., Vaidya, P. V., & Dhara, S. (2021). Dense-porous multilayer ceramics by green shaping and salt leaching. *Open Ceramics*, *5*, 100084. https://doi.org/10.1016/j.oceram.2021.100084

Shang, Y., Hasan, M. K., Ahammed, G. J., Li, M., Yin, H., & Zhou, J. (2019). Applications of nanotechnology in plant growth and crop protection: A review. *Molecules*, *24*(14), 2558. https://doi.org/10.3390/molecules24142558

Shaviv, A., & Mikkelsen, R. L. (1993). Controlled-release fertilizers to increase

efficiency of nutrient use and minimize environmental degradation - A review. *Fertilizer Research*, *35*(1–2), 1–12. https://doi.org/10.1007/BF00750215

Sheng, X., Akinc, M., & Kessler, M. R. (2010). Rheology and dynamic mechanical analysis of bisphenol E cyanate ester/alumina nanocomposites. *Polymer Engineering & Science*, *50*(2), 302–311. https://doi.org/10.1002/pen.21543

Sigmund, W. M., Bell, N. S., & Bergström, L. (2000). Novel powder-processing methods for advanced ceramics. *Journal of the American Ceramic Society*, *83*(7), 1557–1574. https://doi.org/10.1111/j.1151-2916.2000.tb01432.x

Soltan, N., Ning, L., Mohabatpour, F., Papagerakis, P., & Chen, X. (2019). Printability and cell viability in bioprinting alginate dialdehyde-gelatin scaffolds. *ACS Biomaterials Science & Engineering*, *5*(6), 2976–2987. https://doi.org/10.1021/acsbiomaterials.9b00167

Su, B., Dhara, S., & Wang, L. (2008). Green ceramic machining: A top-down approach for the rapid fabrication of complex-shaped ceramics. *Journal of the European Ceramic Society*, *28*(11), 2109–2115. https://doi.org/https://doi.org/10.1016/j.jeurceramsoc.2008.02.023

Sudharsan Reddy, K., Prabhakar, M. N., Kumara Babu, P., Venkatesulu, G., Kumarji Rao, U. S., Chowdoji Rao, K., & Subha, M. C. S. (2012). Miscibility studies of hydroxypropyl cellulose/poly(ethylene glycol) in dilute solutions and solid state. *International Journal of Carbohydrate Chemistry*, *2012*, 1–9. https://doi.org/10.1155/2012/906389

Suo, Z., Ma, E. Y., Gleskova, H., & Wagner, S. (1999). Mechanics of rollable and foldable film-on-foil electronics. *Applied Physics Letters*, *74*(8), 1177–1179. https://doi.org/10.1063/1.123478

Supare, K., & Mahanwar, P. A. (2022). Starch-derived superabsorbent polymers in agriculture applications: an overview. *Polymer Bulletin*, *79*(8), 5795–5824. https://doi.org/10.1007/s00289-021-03842-3

Tan, H., Zhang, Y., Sun, L., Sun, Y., Dang, H., Yang, Y., & Jiang, D. (2021). Preparation of nano sustained-release fertilizer using natural degradable polymer polylactic acid by coaxial electrospinning. *International Journal of Biological Macromolecules*, *193*, 903–914. https://doi.org/10.1016/j.ijbiomac.2021.10.181

Tang, M., Zhong, Z., & Ke, C. (2023). Advanced supramolecular design for direct ink writing of soft materials. *Chemical Society Reviews*, *52*(5), 1614–1649.

https://doi.org/10.1039/D2CS01011A

Tiwari, S., Singh, P., Tiwari, R., Meena, K. K., Yandigeri, M., Singh, D. P., & Arora, D. K. (2011). Salt-tolerant rhizobacteria-mediated induced tolerance in wheat (Triticum aestivum) and chemical diversity in rhizosphere enhance plant growth. *Biology and Fertility of Soils*, *47*(8), 907–916. https://doi.org/10.1007/s00374-011-0598-5

Tomadoni, B., Casalongué, C., & Alvarez, V. A. (2019). Biopolymer-based hydrogels for agriculture applications: Swelling behavior and slow release of agrochemicals. In *Polymers for Agri-Food Applications* (pp. 99–125). Springer International Publishing. https://doi.org/10.1007/978-3-030-19416-1_7

Torun, A. A., Gülmezoğlu, N., Tolay, İ., Duymuş, E., Aytaç, Z., Cenkseven, Ş., & Torun, B. (2019). Effects of zinc and NaCl applications on dry matter yield and mineral nutrient concentrations of durum wheat (Triticum durum Desf.). *Journal of Bahri Dagdas Crop Research*, *8*(1), 1–10.

Trenkel, M. E. (1997). *Controlled-release and stabilized fertilizers in agriculture: Improving fertilizer use efficiency*. IFA, International fertilizer industry Association.

Tripathi, A., & Kumar, A. (2011). Multi-featured macroporous agarose-alginate cryogel: Synthesis and characterization for bioengineering applications. *Macromolecular Bioscience*, *11*(1), 22–35. https://doi.org/10.1002/mabi.201000286

Tsai, S. C., & Zammouri, K. (1988). Role of interparticular Van der Waals force in rheology of concentrated suspensions. *Journal of Rheology*, *32*(7), 737–750. https://doi.org/10.1122/1.549988

United States Department of Agriculture. (2001). *Cellulose processing*. https://www.ams.usda.gov/sites/default/files/media/Cellulose TR 2001.pdf

Vaben, R., & Stöver, D. (1997). Properties of silicon-based ceramics produced by hot isostatic pressing ultrafine powders. *Philosophical Magazine B*, *76*(4), 585–591. https://doi.org/10.1080/01418639708241124

Vickers, G. W., & Quan, K. (1989). Ball-mills versus end-mills for curved surface machining. *Journal of Engineering for Industry*, *111*, 22–26. https://api.semanticscholar.org/CorpusID:110084001

Vincent, B., Luckham, P. F., & Waite, F. A. (1980). The effect of free polymer on the stability of sterically stabilized dispersions. *Journal of Colloid and Interface Science*, *73*(2), 508–521. https://doi.org/10.1016/0021-9797(80)90097-1

Wang, C., Wang, J., Li, Q., Xu, S., & Yang, J. (2024). A review on recent development

of foam ceramics prepared by particle-stabilized foaming technique. *Advances in Colloid and Interface Science*, *330*, 103198. https://doi.org/10.1016/j.cis.2024.103198

Wang, J., & Zhuang, S. (2022). Chitosan-based materials: Preparation, modification and application. *Journal of Cleaner Production*, *355*, 131825. https://doi.org/10.1016/j.jclepro.2022.131825

Wang, W., Kweon, S. H., & Yang, S. H. (2005). A study on roughness of the micro-end-milled surface produced by a miniatured machine tool. *Journal of Materials Processing Technology*, *162–163*, 702–708. https://doi.org/10.1016/j.jmatprotec.2005.02.141

Wei, L., Abd Rahim, S., Al Bakri Abdullah, M., Yin, A., Ghazali, M., Omar, M., Nemeș, O., Sandu, A., Vizureanu, P., & Abdellah, A. (2023). Producing Metal Powder from Machining Chips Using Ball Milling Process: A Review. *Materials*, *16*(13), 4635. https://doi.org/10.3390/ma16134635

Wu, Y., Xu, K., Yin, R., Li, J., & Xue, R. (2020). Fabrication of Sialon ceramic via non-aqueous gelcasting based on the HEMA gelling agent. *Ceramics International*, *46*(16), 25236–25241. https://doi.org/10.1016/j.ceramint.2020.06.315

Xu, W., Wang, X., Sandler, N., Willför, S., & Xu, C. (2018). Three-dimensional printing of wood-derived biopolymers: A review focused on biomedical applications. *ACS Sustainable Chemistry & Engineering*, *6*(5), 5663–5680. https://doi.org/10.1021/acssuschemeng.7b03924

Yin, L., Peng, H. X., Dhara, S., Yang, L., & Su, B. (2009). Natural additives in protein coagulation casting process for improved microstructural controllability of cellular ceramics. *Composites Part B: Engineering*, *40*(7), 638–644. https://doi.org/10.1016/j.compositesb.2009.04.016

Yoo, J., & Won, Y.-Y. (2020). Phenomenology of the initial burst release of drugs from PLGA microparticles. *ACS Biomaterials Science & Engineering*, *6*(11), 6053–6062. https://doi.org/10.1021/acsbiomaterials.0c01228

Yoon, J., Yang, H., Lee, B., & Yu, W. (2018). Recent progress in coaxial electrospinning: New parameters, various structures, and wide applications. *Advanced Materials*, *30*(42). https://doi.org/10.1002/adma.201704765

Yu, J., Wang, H., Zeng, H., & Zhang, J. (2009). Effect of monomer content on physical properties of silicon nitride ceramic green body prepared by gelcasting. *Ceramics*

International, *35*(3), 1039–1044. https://doi.org/10.1016/j.ceramint.2008.04.021

Yu, Z. B., & Thompson, D. P. (2006). Sialons. In *Ceramic-Matrix Composites* (pp. 491–513). Elsevier. https://doi.org/10.1533/9781845691066.5.491

Zamboulis, A., Michailidou, G., Koumentakou, I., & Bikiaris, D. N. (2022). Polysaccharide 3D printing for drug delivery applications. *Pharmaceutics*, *14*(1), 145. https://doi.org/10.3390/pharmaceutics14010145

Zemberekci, L., Demir, G., Akaoglu, C., Aldulaimi, W. A., Ozhan, A. B., Gulgun, M. A., Akhlaghi, O., & Akbulut, O. (2021). Polymer bridging induced by a single additive imparts easy-to-implement green machinability to yttria-stabilized zirconia. *ACS Applied Polymer Materials*, *3*(11), 5397–5404. https://doi.org/10.1021/acsapm.1c00605

Zhai, W., Bai, L., Zhou, R., Fan, X., Kang, G., Liu, Y., & Zhou, K. (2021). Recent progress on wear-resistant materials: Designs, properties, and applications. *Advanced Science*, *8*(11). https://doi.org/10.1002/advs.202003739

Zhang, C., Janssen, R., & Claussen, N. (2003). Pressureless sintering of β-sialon with improved green strength by using metallic Al powder. *Materials Letters*, *57*(22–23), 3352–3356. https://doi.org/10.1016/S0167-577X(03)00073-9

Zhong, Y., Cai, J., & Zhang, L.-N. (2020). A review of chitin solvents and their dissolution mechanisms. *Chinese Journal of Polymer Science*, *38*(10), 1047–1060. https://doi.org/10.1007/s10118-020-2459-x

Zhou, Y., Hyuga, H., Kusano, D., Yoshizawa, Y., Ohji, T., & Hirao, K. (2015). Development of high-thermal-conductivity silicon nitride ceramics. *Journal of Asian Ceramic Societies*, *3*(3), 221–229. https://doi.org/10.1016/j.jascer.2015.03.003

Zhu, C., & Smay, J. E. (2011). Thixotropic rheology of concentrated alumina colloidal gels for solid freeform fabrication. *Journal of Rheology*, *55*(3), 655–672. https://doi.org/10.1122/1.3573828